STUDY AND CLASSIFICATION OF LUNAR SURFACE USING MINI-SAR DATA

A DISSERTATION

Submitted in partial fulfillment of the
requirements for the award of the degree
of

INTEGRATED DUAL DEGREE

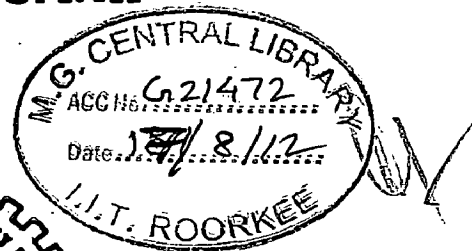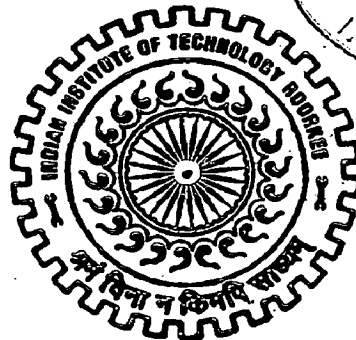(Bachelor of Technology & Master of Technology)

in

ELECTRONICS AND COMMUNICATION ENGINEERING

(With Specialization in Wireless Communication)

By

SHAILESH KUMAR

DEPARTMENT OF ELECTRONICS AND COMPUTER ENGINEERING
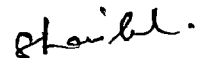INDIAN INSTITUTE OF TECHNOLOGY ROORKEE
ROORKEE - 247 667 (INDIA)
JUNE, 2012

Candidate's Declaration

I hereby declare that the work, which is presented in this dissertation report entitled, "STUDY AND CLASSIFICATION OF LUNAR SURFACE USING MINI-SAR DATA" towards the partial fulfilment of the requirements for the award of the degree of **Integrated Dual Degree (Bachelor of Technology and Master of Technology)** in Electronics and Communication Engineering with Specialization in **Wireless Communication**, submitted in the Department of Electronics and Computer Engineering, Indian Institute of Technology Roorkee, Roorkee (India) is an authentic record of my own work carried out during the period from June 2011 to June 2012, under the guidance of **Dr. Dharmendra Singh, Associate Professor, Department of Electronics and Computer Engineering, Indian Institute of Technology Roorkee.**

I have not submitted the matter embodied in this dissertation for the award of any other Degree or Diploma.

Date: 8|06|2012

Place: Roorkee

SHAILESH KUMAR

CERTIFICATE

This is to certify that the above statement made by the candidate is correct to the best of my knowledge and belief.

Date: 8|06|2012

Place: Roorkee

Dr. Dharmendra Singh

Associate Professor

E&C Department

IIT Roorkee

ACKNOWLEDGEMENT

ABSTRACT

In present study an attempt has been made to classify the craters to check the possibility of finding planetary water-ice deposits For this purpose, three different approaches (i.e., polarimetric, pattern analysis and fractal) have been applied for understanding the scattering behaviour of lunar surface. The polarimetric approach, m-δ decomposition is used to identify craters having high probability of planetary water-ice deposits and then based on pattern analysis of CPR pixels a method is described to classify craters into two categories type-I and type-II. **Type-I craters are those craters which have high probability of having planetary water-ice deposits and type-II craters are those craters which have low probability of having planetary water-ice deposits.** This classification is based on degree of polarization and relative phase between LH-LV receptions. Different polarimetric parameters (child parameters) are calculated and statistics of these parameters are calculated for different craters.

Further in this study unsupervised classification of mini-SAR images based on the surface texture is carried out. Texture parameter is measured with the help of fractal dimension (D), which lies in the range 2.0 and 3.0. Based on fractal values, i.e., 'D', various regions of lunar surface is clustered in different classes. Using moving window approach, the local fractal dimension 'D' is estimated with Triangular Prism Surface Area Method (TPSAM) and Differential Box Counting (DBC) method for different window sizes and corresponding fractal maps from TPSAM method are used for classification purpose. Different window sizes may give different results thus the window size is very important for classification and hence effect of window size on fractal dimension and on Moran'sI is discussed. The K-means classifier has been used for classification which clusters the pixels according to 'D' values. Although fractal dimension is able to provide the texture information very efficiently but it cannot uniquely identify all the classes. In order to remove this discrepancy, analysis based on spatial autocorrelation has been performed. For this purpose local value of Moran's I is calculated by varying window sizes, Moran's I gives spatial autocorrelation of pixels. Spatial autocorrelation measures the correlation of a variable with itself through space. Spatial autocorrelation can be positive or negative. Positive spatial autocorrelation occurs when similar values occur near one another. Negative value of spatial autocorrelation occurs when dissimilar values occur near one another thus classification based on Moran's I and fractal

dimension 'D' can give classification results with enhanced accuracy. Classification results are studied to draw conclusions, further the classification results are compared against images generated by m-δ decomposition of mini-SAR images.

LIST OF FIGURES

TABLE OF CONTENTS

Chapter 1

Introduction

In recent years advancement of rocket science and remote sensing technology has lead humans to explore its near space for the search of life and essential components needed to support life. In space science Moon holds a very important place as it is closest terrestrial object from Earth. Moon can be very good prototype for studying other terrestrial objects. In past there have been many missions to Moon for collecting data of lunar surface to study its properties and to analyze the possibilities of finding planetary water-ice deposits on lunar surface.

Chandrayan-I was one such attempt to study and collect data on lunar surface by Indian Space and Research Organization (ISRO) [1, 2]. Mini-SAR was a microwave imaging sensor onboard Chandrayan-I. A Miniature Synthetic Aperture Radar (mini-SAR) system illuminates a scene with microwaves and records both the amplitude and the phase of the back-scattered radiation, making it a coherent imaging process at centre frequency 2.38 GHZ. Mini-SAR is hybrid polarimetric Radar and it stores data in four channels from which complete scattering matrix can be calculated, Spudis et.al [2, 3, 4]. The received signal is sampled and converted into a digital image and sent to ground stations. This image is further analyzed on ground stations for acquiring different information about lunar surface using combination of image processing techniques, microwave and remote sensing concepts. It was first attempt of microwave imaging of lunar surface all earlier attempts were based on optical imaging technique; data recorded by mini-SAR provides unique opportunity to study the dark areas of the lunar craters on Moon [3, 4]. . Since the temperature on the Moon varies from - 387 Fahrenheit (-233 Celsius), at night, to 253 Fahrenheit (123 Celsius) during the day time [5]. Regions where sunlight reach in day time become very hot thus there is no possibility of finding planetary water-ice in any form i.e. frozen or liquid form, in such regions hence study of permanently shadowed regions is necessary where temperature remains very low. As microwaves can penetrate in the surface and are independent of solar illumination, it would be possible to reach the permanently shadowed regions of the lunar craters especially polar

1

region craters and to arrive at further conclusive evidence on the possibility of planetary water-ice in the permanently shadowed zones of lunar craters.

1.1 Motivation

Among the various studies, it has been shown that polar region of lunar surface may contain planetary water-ice deposits [3, 5-8]. Though, detailed, conclusive and extensive evidences are still needed for the claim. As it is possible to find planetary water-ice in polar region craters, so an extensive and detailed study of polar craters is needed to identify possible regions where possibility of finding planetary water-ice is higher. Further classification is an important step towards the retrieval of geophysical parameters. Classification scheme based on textural and polarimetric property of mini-SAR data can prove useful for understanding the characteristics of the lunar surface and crater regions, particularly for the physical assessment for the type of scatterers and different scattering phenomenon associated with them. Thus classification can be an important step towards understanding the lunar surface characteristics. Previous analysis of mini-SAR images has revealed presence of mixed planetary water-ice on permanently shadowed regions of polar craters based on the assumption that CPR>1 occur for those regions where lunar surface contain planetary water-ice deposits but further studies revealed that CR>1 can also occur due to high roughness of lunar surface[2-4] (Fig.1.1). The two regions where CPR>1 is due to dielectric mixing i.e. due to presence of planetary water-ice or because of surface roughness, can be differentiated by scattering mechanism associated with them. Dominant volume scattering behaviour is expected for dielectric mixing and dihedral or double bounce scattering behaviour is expected for surface roughness.

High CPR caused by surface roughness scattering   High CPR caused by ice/volume scattering
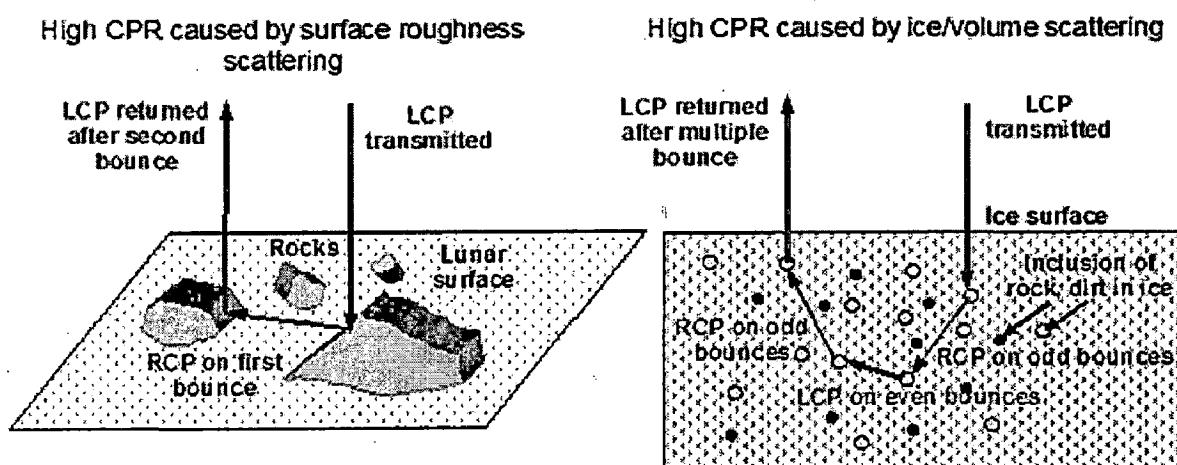
Figure: 1.1 CPR>1 due to double bounce and due to volume scattering from ice [3]

2

Thus the objective of this study is to determine the different scattering mechanism associated with lunar surface. Further a textural analysis on mini-SAR image is performed to classify lunar surface using fractal and spatial correlation coefficients. Polarimetric SAR images are widely used for terrain classification for Earth as they can extract geometrical properties (size, shape, orientation distribution and spatial arrangement of objects) and physical information about the target like symmetry, non symmetry and irregularity of the target [9] but classification of lunar surface based on texture properties of mini-SAR images is not performed so far, so motivation behind taking up the task of terrain classification of Moon surface using mini-SAR data is to explore different terrain types of lunar surface along with learning different approaches to classify satellite images. Before textural analysis, a statistical analysis is performed to identify and develop a method based n pattern analysis to identify craters having higher probability of finding planetary water-ice deposits with the aid of 'm-δ' decomposition technique results.

1.2. Aim and objective of the thesis

Aim of this dissertation work is to generate 'm-δ' maps for studying different scattering mechanism associated with lunar surface. Analyzing different scattering mechanism associated with craters of polar regions to classify them in two categories, one having dominant volume scattering phenomenon and another having dominant double bounce and surface scattering phenomenon, in this thesis these two types of craters are called **type-I** and **type-II** respectively, since type-I craters have dominant volume scatterers so they have higher probability of finding planetary water-ice. To perform a statistical analysis of lunar craters and to develop a method based on pattern analysis to identify type-I and type-II of craters, to generate a land cover classification map of lunar surface using textural properties,

The objectives of this thesis are:

The main objective of thesis is to understand the scattering behaviour of lunar surface with polarimetric as well as other methods to understand the possibility of planetary water-ice deposits on Moon surface. For this purpose, several sub tasks are formulated which are as following

- Calculation stokes matrix from raw mini-SAR data

3

- Calculation and study of various child parameters which describes scattering phenomenon
- Study of 'm-δ' decomposed images to understand scattering phenomenon.
- Study of various statistical models to fit data points to a distribution function for understanding the distribution nature of mini-SAR data.
- Develop a method based on density functions/pattern analysis to differentiate craters
- Study of various methods for extracting textural information for terrain classification.
- Perform unsupervised classification on textured images
- Study the role of window size on classification.

1.3. Organization of the thesis

This thesis consists 5 chapters.

In *chapter 2* brief review is presented, this chapter explains basics of radar polarimetry i.e. wave and scattering concepts. It includes mathematical formulations and theory about different scattering matrices to represent radar scattering, general concepts of fractals and spatial correlation and their previous application, description of different classification strategies. In this chapter different scattering phenomenon is also explained.

In *chapter 3* details about the methodology adopted for this thesis is presented. It presents description of test site, along with the description of used mini-SAR data and software. Data processing techniques which are used for this thesis is described. Methods to determine child parameters are explained in detail. Then steps used for differentiating two crater types based on 'm-δ' value and then RGB decomposition using 'm-δ' is explained. This chapter also includes the methodology used for statistical and texture analysis. Methods to calculate fractal dimension (D) and Moran's I are discussed in detail then methodology to generate fractal map and Moran's I map is discussed. Classification steps adopted using these texture images is presented.

In *chapter 4*, .implementation, results and discussion are presented. Implementation and results of all the methods discussed in methodology (chapter-3) are explained. Child parameters are calculated and their statistics and significance are discussed. Then implementation of 'm-δ' technique is presented along with its results, some of the craters which are identified as type-I and type-II are shown. Results of GoF tests are shown and best fit distribution function to represent CPR data is determined. Then range of position and shape parameters of density functions representing type-I and type-II craters are determined.

Implementation of textural analysis is presented; Fractal and spatial auto correlation maps are shown, classified images for a specific region is shown. Effect of window size on texture property is discussed.

Finally concluding remarks are presented in chapter 5

Chapter 2

Brief Review

2.1. Basics of Radar Polarimetry

In these sections basics of radar polarimetry concepts, hybrid architecture of radar is discussed along with classification techniques. There are two main conceptual formalisms in polarimetry. The first one is a real space formalisms based on the Stokes Vector for the description of the polarimetric properties of waves for the polarimetric description of the scatterers. The second one is a complex space formalism based on the Jones vector for the analysis of wave polarization for the description of the scattering phenomenon. Both formalisms are equivalent and can be changed unambiguously into one another. Since most of the child parameters derived are real in nature and don't have any phase associated with them, so in this study real domain formalism is chosen. In following sections Stokes vector and Jones vector are discussed along with polarization concept, which is the basis of radar polarimetry.

2.1.1 Polarization

For an EM monochromatic plane wave, the polarization can be described in terms of the orientation of the electric field vector w.r.t. the plane perpendicular to the direction of propagation, as a function of time. The electric field component can be resolved into two orthogonal sinusoidal waves namely 'x' and 'y' component having different amplitudes as given in Eq. (2.1) A plane electromagnetic wave is fully characterized by the parameters (magnitude, phase, and direction) of its electric vector $E(r, t)$ given by

$$E(r,t) = E_x \hat{x} + E_y \hat{y} = (a_x . \exp(j\delta_x)\hat{x} + a_y . \exp(j\delta_y)\hat{y}) . \exp(j(\omega t - kz)) \qquad (2.1)$$

Polarization of microwaves can be explained easily with the help of polarization ellipse. Polarization ellipse is defined as locus of the tip of electric field vector as shown in Fig.2.1 The shape and orientation of the ellipse together with the rotation sense of the field vector,
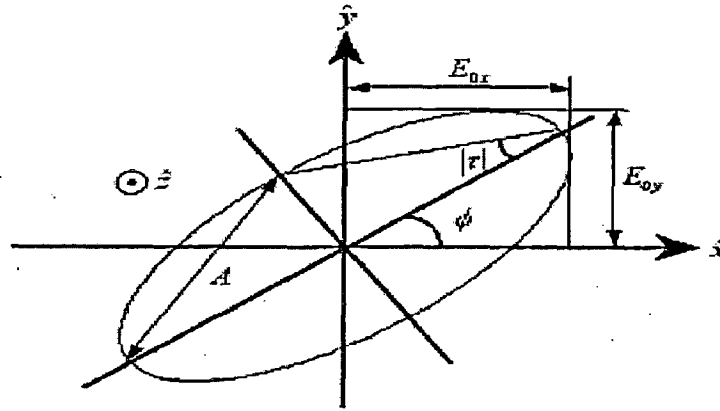
Figure: 2.1 Polarization Ellipse [10]

When looked along the direction of propagation can describe the polarization state [10]. To completely able to describe the polarization state we need orientation angle Φ and tilt angle τ.

They are described as follows:

- The orientation angle Φ is defined as the angle between the major axis of the ellipse and the x- axis, expresses the inclination of the ellipse and is limited between $0°$ and $180°$.

- The tilt angle τ, defined as the ratio between two minor semi-axes of the ellipse (a, b) describes the shape of the ellipse.

$$\tan\tau = \pm\frac{b}{a}$$

(2.2)

The polarisation sense; given by the sign of τ (the positive value applies for right-handed polarizations)

There are three types of polarizations : linear , circular and elliptical depending on the values of above parameters. They are summerized in table-2.1:

Table-2.1

Polarization descriptors for characteristic polarization states [10]

	Horizontal	Vertical	Linear 45°	Linear 135°	Left circular	Right circular
Orientation Φ	90	0	45	135	0 to 180	0 to 180
Tilt angle τ	0	0	0	0	45	-45
Complex ratio ρ	0	∞	1	-1	i	-i

8

2.1.2 Jones vector

Jones vector E_{xy} may be defined as [11]

$$E_{xy} = \begin{bmatrix} E_x \\ E_y \end{bmatrix} = \begin{bmatrix} |E_x| \exp(j\delta_x) \\ |E_y| \exp(j\delta_y) \end{bmatrix} = E_x \begin{bmatrix} 1 \\ \rho \end{bmatrix} \tag{2.3}$$

Where ρ is called polarization ratio, defined by [11]

$$\rho = \frac{E_y}{E_x} = \frac{|E_y|}{|E_x|} \exp(j\{\delta_n - \delta_m\}) \tag{2.4}$$

2.1.3 Stokes vector

For a quasi monochromatic wave the Stokes vector formulation is used, which is defined by

$$g = \begin{bmatrix} g_0 \\ g_1 \\ g_2 \\ g_3 \end{bmatrix} = \begin{bmatrix} e^2 \\ e^2 \sin 2\phi \cos 2\tau \\ e^2 \cos 2\phi \sin 2\tau \\ e^2 \sin 2\tau \end{bmatrix} \tag{2.5}$$

g_0 is the total intensity, g_1 is the difference of the intensities in both polarizations, while g_2 and g_3 contain the phase information [12]. These four parameters are not independent for a fully polarized wave, since in that case the following identity holds:

$$g_0^2 = g_1^2 + g_2^2 + g_3^2 \tag{2.6}$$

2.2. Hybrid Polarimetry and mini-SAR

To date all conventional dual-polarized radars (and also all quad pol radars for that matter) are designed such that the polarization of receiver antenna agrees with the transmitted signal. It follows that there always must be a "like-polarized" and a "cross-polarized" channel in the receiver, i.e. for transmitted H-polarized wave receiver antenna should be H-polarized for "like-polarized" reception and V-polarized for "cross-polarized reception". A hybrid-polarity

synthetic aperture radar (SAR) is a dual polarized system that transmits circular polarization, either left (LC) or right (RC) and receives coherently in orthogonal linear polarizations, horizontal (H) and vertical (V).

·A generic diagram of the hybrid polarity architecture is shown in Fig.2.2. One simple approach to this type of mixed mode radar is based on a dual-linearly-polarized antenna, which will radiate circular polarization, if the H and V feeds are driven simultaneously at 90° out of phase [4]. Mini-SAR a microwave imaging sensor on-board **Chandrayan-I** mission of ISRO was designed to gather data on the scattering properties of polar region of the Moon and it had this hybrid polarimetry architecture [2, 4].

Mini-SAR was a single frequency (2.38 GHz), hybrid polarimetry imaging radar designed to collect information about the scattering properties of the permanently dark areas near the lunar poles at optimum viewing geometry[1, 2, 4]. Additionally, mini-SAR was designed to map the terrain of these areas, invisible to optical imaging sensors through a side looking SAR mode and nadir looking scatterometer mode. The specific instrument parameters and data collection modes are shown in Appendix-I [2]. Mini-SAR mapped both Polar Regions systematically with a resolution of 75 m/pixel which is of sufficient quality to identify areas of unusual scattering properties. Thus, mini-SAR measurements are expected to provide RF data of better resolution to classify lunar surface and more conclusive evidence of presence of deposits of planetary water-ice deposits in permanently shadowed regions.
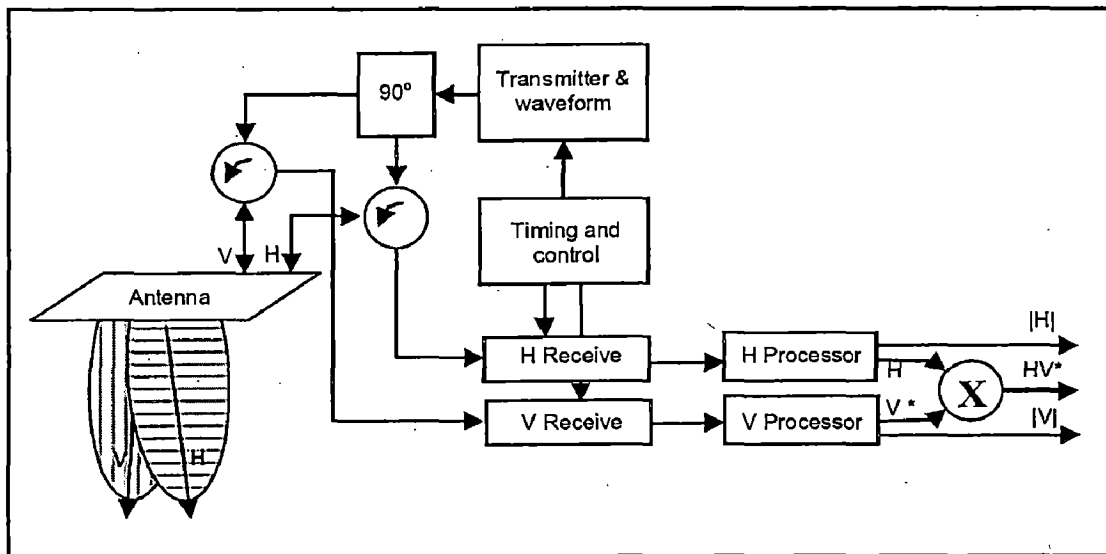
Figure: 2.2 Generic hybrid polarimetry architecture [4]

2.3 Different scattering mechanism

Canopy layer   Double bounce   Rough surface
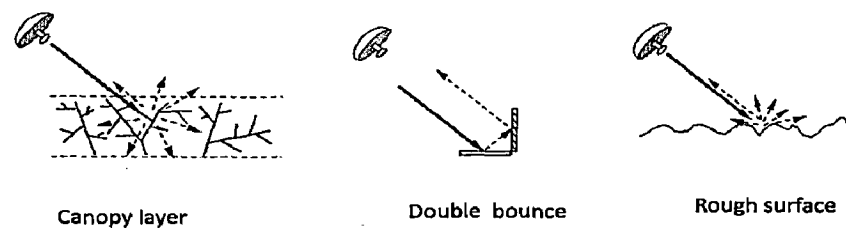
Figure: 2.3 Model of different scattering mechanism

Different scattering phenomenon can be described by a three-component scattering model suited for classification and inversion of air-borne and space-borne polarimetric SAR image data this model can be also applied too mini-SAR data. This scattering model presents the scattering phenomenon as the contribution of three scattering mechanisms (Fig.2.3) [13]

- **Volume scattering:** Modelled by a set of randomly oriented dipoles.
- **Double-bounce scattering:** Modelled by scattering from a dihedral corner reflector.
- **Single-bounce scattering:** Modelled by a first-order Bragg surface scatterers.

For the case of Earth volume scattering occurs for diffused targets such as trees, forests, double bounce also known as dihedral scattering takes place where two walls are inclined to each other e.g. building walls. Surface scattering takes place at large plane fields, roads etc. These scattering mechanisms can be resolved using 'm-δ' decomposition technique for mini-SAR images; it is discussed in section-3.4.

2.4 Statistical modelling of satellite data

Pixel values of any satellite image can be assumed of an outcome of a random process [14, 15]. When the resolution of images are fairly low (i.e. larger area/pixel) and surface contains variety of terrains and objects then from central limit theorem this random process can be assumed Gaussian without any harm but when resolution increases (i.e. lower area/pixel) and surface doesn't show much variety then Gaussian assumption is most likely to fail as in the case of mini-SAR images. Thus the need of modelling the distribution behaviour of data is an important step for analysis purpose. Since, lunar surface doesn't vary much compared to mini-SAR image resolution, 75mx75m/per pixel [2].

Statistical modelling of radar data in terms of probability density functions (PDFs) is an important exercise which forms the basis of many radar image analysis techniques. Experience with single-polarization radar data has shown that they are well suited for parametric modelling, and a number of distribution families have been proposed for the purpose. Some models are based on the simplistic complex Gaussian assumption of the scattering coefficient distribution, such as the Rayleigh distribution for single-look amplitude data, the exponential distribution for single-look intensity data, and the gamma distribution for multilook intensity data [14]. Other distribution models, such as the Weibull and the log-normal, Beta etc. provide added flexibility and the ability to model data with non-Gaussian characteristics [15, 16]. The goodness of fit of a statistical model describes how well a statistical model fits to a set of observations. Measures of goodness of fit typically summarize the discrepancy between observed values and the values expected under the model in question [17, 18]. Such measures can be used in statistical hypothesis testing. In this dissertation goodness of fit test is used to determine nature of distribution of pixels in an image or in a local region of interest.

Goodness of Fit (GoF) test

There exist a number of GoF tests but the following three tests were studied for the purpose:

       i) Kolmogorov–Smirnov test [19, 20]
       ii) Anderson–Darling test [20, 21]
       iii) Chi Square test [20, 22]

Among these Chi-square test is most popular and efficient test for unbinned data. Performance of GoF test for small data size reduces significantly because for small data samples, asymptotic approximations do not hold [17, 18]. Thus care must be taken to ensure there are sufficient data points are in sample. Detailed description of these tests are given in section-3.5

2.5 Classification schemes

Classification of satellite images mean clustering of like pixels based on their SAR, textural or any other property. There are two types of classification techniques: **supervised** and **unsupervised**. Supervised methods require the user to collect samples to "train" or teach the classifier to determine the decision boundaries in feature space, and such decision boundaries are significantly affected by the properties and the size of the samples used to train the

12

classifier. On the other hand, unsupervised classifiers "learn" the characteristics of each class directly from the input data. Since for lunar surface we don't have any training data so for the classification purpose of lunar surface unsupervised classification technique is used. So in following section supervised classification technique is discussed in brief.

2.5.1. Supervised classification

Supervised classification involves using a priori knowledge of data to "train" computer software to identify classes in an image [23]. The supervised approach to pixel labelling requires the user to select representative training data for each of a predefined number of classes [24]. It is assumed that the classification (the definition of the groups and their characteristics) has been defined before any previously unknown objects were identified.

Steps for supervised classification:

i. Decide the set of ground cover types into which image is to be segmented. These are called information class. The information classes are determined by ground truth survey, maps or personal experience,

ii. Chose representative pixels on image from each of the desired set of classes. These pixels are called training samples.

iii. Estimate the statistical parameters for each required class using training samples.

iv. Select proper decision rule for classification.

v. Select the classifier, which classify every pixel in the image into one of the desired ground cover types (information class).

2.5.2 Unsupervised classification

Unsupervised classification is the process in which clusters are generated automatically based on natural grouping found in data. Due to this nature the technique is commonly referred to as clustering. Unlike supervised classifier, it does not require the selection of training data in order to train the classifier. This classifier operates independently and does not require intervention of user. Therefore sometimes it may happen that results are unaccepted on the basis of failure of user's expectations.

Steps for unsupervised classification are [25]:

i. Classify image into number of clusters or group.

ii. Indentify clusters and assign name to each group.

13

iii.   Merge classes (if required).

iv.   Post classification and accuracy assessment.

Unsupervised classification is of two types: *i) K-mean* and *ii) ISO-data.*

i. K-mean

K-means unsupervised classification algorithm (Fig.2.4) first assigns arbitrarily initial K-cluster vectors. The input cluster vectors are then iteratively assigned to closest cluster according to the square of the Euclidean distance from the clusters. This is illustrated in (Fig-2.5), where data pixel 'a' is closest to class 3, hence is put in class 3. Each iteration recalculates mean (centroid) of each cluster and reclassifies pixels with respect to the new means. All pixels are classified to the nearest class unless a standard deviation or distance threshold is specified, in which case some pixels may be unclassified if they do not meet the selected criteria. This process is repeated until no more "change" in the value of the means or the maximum number of iterations is reached. The "change" can be defined either by measuring the distances the mean cluster vector have changed from one iteration to another or by the percentage of pixels that have changed between iterations [26].
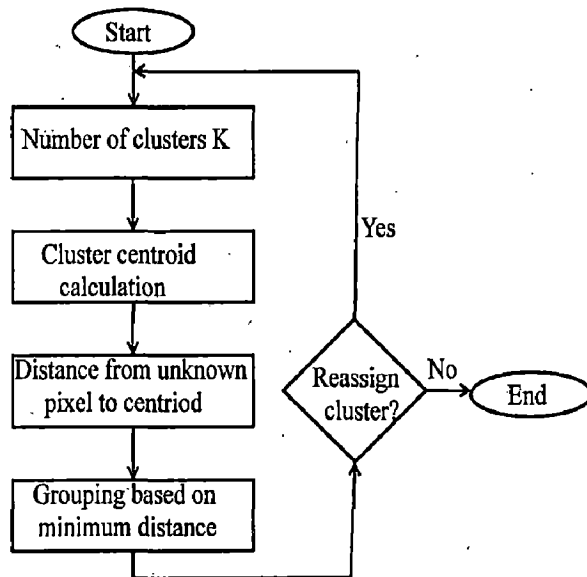
Figure: 2.4 K-means algorithm [26]   Figure: 2.5 Minimum distance classification example [24]
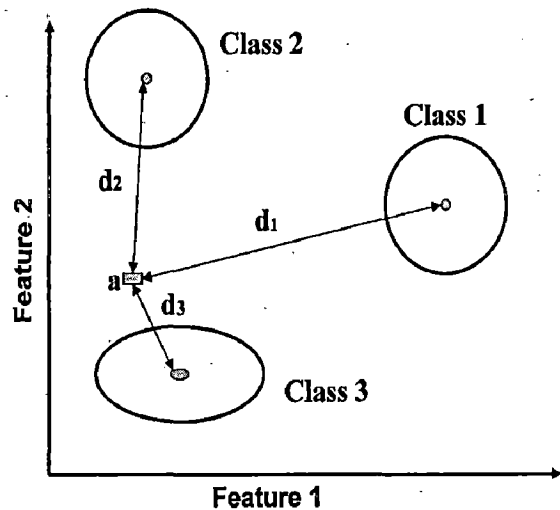
Merits:

a.   With a large number of variables, K-Means may be computationally faster than hierarchical clustering (if K is small).

b.   K-Means may produce tighter clusters than hierarchical clustering, especially if the clusters are globular.

14

Demerits [27]:

a. K-means is very sensitive to initial starting value of cluster centre.

b. K-means assumes that the number of clusters is known a priori, which is not true for real world situation.

c. Does not work well with non-globular clusters.

ii. ISO-data

The iterative self organizing data (ISO-data) algorithm represents a comprehensive set of heuristic (rule of thumb) procedures that have been incorporated into an iterative classification algorithm. ISO-data is a nearest-centroid, non-hierarchical, clustering algorithm. It performs in the same manner as K-mean but with further refinements by splitting and merging of clusters [28]. Iterative class splitting, merging, and deleting are done based on input threshold parameters. Clusters are merged if either the number of members (pixel) in a cluster is less than a certain threshold or if the centres of two clusters are closer than a certain threshold. Clusters are split into two different clusters if the cluster standard deviation exceeds a predefined value and the number of members (pixels) is twice the threshold for the minimum number of members. Using accuracy of classification result some parameters need to be optimized but ground truth data for lunar surface is not available to estimate accuracy of classification and its very time consuming when compared to K-means algorithm, so K-means classifier is preferred over iso-data classifier.

Merits:

a. More robust.

b. User specific.

c. ISODATA is self-organizing because it requires relatively little human input.

d. Clustering is not geographically biased to the top or bottom pixels, since it is iterative.

Demerits:

a. The clustering process is time-consuming, because it can repeat many times.

2.6 Fractals

2.6.1 Definition and its application'

The term fractal, given by Mandelbrot[29]. Self-similarity and fractal dimensions are two basic characteristics which define fractal. Fractals are widely being used for natural surface modelling and analysis purpose [29-35]. Due to complex nature of natural objects and

surfaces traditional geometrical objects, viz., lines, circles, cones etc. can not represent them [29, 36, 37]. With the introduction of fractal geometry, more flexibility got introduced in modelling of natural surfaces with fractal approach. In analysis of satellite images, fractal approach is getting more and more attention and it is helpful in various applications [33, 34, 37]. In order to apply fractal geometry to natural image analysis, Pentland [37] had proposed that natural surfaces can be modelled with fractional Brownian motion (fBm) function [35, 38]. The image intensity $I(x, y)$ follows the fBm process, given by (2.7)

$$\Pr\left[\frac{I(x+\Delta x, y) - I(x, y)}{\|\Delta x\|^H} < z\right] = F(z) \qquad (2.7)$$

Where, $F(z)$ is the c.d.f and $0 < H < 1, H \in R$ is the Hurst parameter. In fact the height difference, i.e., $I(x+h, y+k)-I(x, y)$ follows the normal distribution with zero mean and variance $(h^2+k^2)^H$ and hence the fractional Brownian surfaces are defined as [39]

$$P(I(x+h, y+k) - I(x, y) \le z) = \frac{1}{\sqrt{2\pi}\sqrt{(h^2 + k^2)^H}} \int_{-\infty}^{z} \exp\left(\frac{-r^2}{2(h^2 + k^2)^H}\right) dr \qquad (2.8)$$

The most important property of fractals, i.e., self-similarity, also called scale independence means by magnification or reduction any part of the image can be formed from any part of that image [29, 35, 39]. An example of self similarity is shown in Fig.2.6. Though, natural scenes are similar to another at some extent but they are not exactly same. So self-similarity of natural scenes is limited i.e. they are not truly self-similar rather they are statistically self-similar. The second property of fractals, i.e., fractal dimension (D) is the measure of complexity of the fractals [35, 39, 40]. Though there exists multiple definition of fractal dimension but most versatile definition is self-similarity dimension is considered as the fractal dimension [29], which is defined as

$$D = \frac{\log(N_r)}{\log\left(\frac{1}{r}\right)} \qquad (2.9)$$

Where,

N_r represents the number of similar parts of an object scaled down by the ratio r.
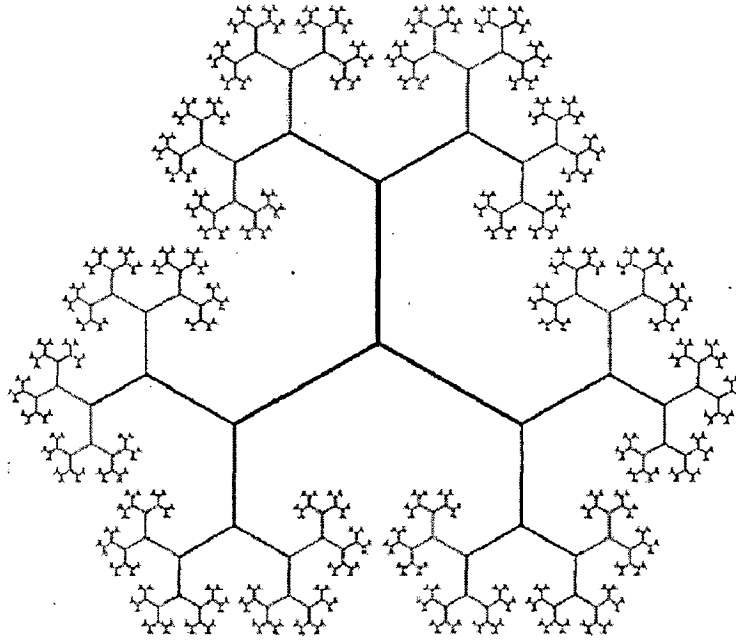
Figure: 2.6 Illustration of self similarity [41]

2.6.2. Significance of Fractals

Fractal dimension is more important for image analysis in terms of estimating irregularities or roughness. The basic thing is that fractal dimension 'D' gives an idea of irregularity or roughness and using local fractal dimension, we can get an index ('D') value of roughness at local level. As it is very common to say rough, very rough, highly rough and so on for various land classes; this terminology ends with 'D' values which map these terms into a range between 2.0 and 3.0 depending on terrain properties [35, 37, 40]. Local variations computed in 'D' values can be used as texture measure for clustering of images. The basic idea is that various land cover types may have their characteristic texture and their roughness could be described by 'D' values. 'D' could be considered as the fractal signature of the land cover types if there were a one to one relation between the land cover texture and a unique 'D' value [34, 35]. However, this assumption is only hypothetical because fractal dimension is not a unique feature, i.e. it cannot identify all the different textures uniquely [30, 40, 42].

Methods to calculate Fractal Dimension

In order to estimate the fractal dimension of surfaces a number of methods exist and are listed below:

- Differential Box counting (DBC) method [42, 43]

- Triangular Prism Surface Area Method (TPSAM)[44-46]

17

- Isarithm method [35]
- Fourier spectrum method [35],
- Two Dimensional variation method (2DVM) [47].

Among these methods, the most famous and widely used method is TPSAM besides this DBC method is also studied for analysis in present thesis. The advantages of the chosen methods for present study over other methods are their feasibility and simplicity to implement. Since, these methods are easy to implement hence they are preferred over other methods both of these methods are discussed in section-3.4.1.

2.7. Spatial autocorrelation (Moran's *I*)

However fractal dimension provides a good tool for classification of surface but using fractal dimension alone for clustering of land cover classes, it is very difficult to identify different classes uniquely i.e., it cannot identify all the different textures uniquely [30, 42,40]. Therefore spatial autocorrelation or Moran's*I* is introduced to aid fractal dimension to classify mini-SAR images. Spatial autocorrelation index maps the pixel clustering properties in a fixed range and based on that range, the association can be explained. Moran's*I* provides an index for determining association of a data point with its neighbourhood. Spatial autocorrelation measures the correlation of a variable with itself through space. Moran's*I* can be estimated either globally or locally according to the application requirement [48]. The global value of '*I*' represents mutual association of all the pixels in image, which is not of much interest for classification purposes. As the image size grows, global '*I*' become less important. On the other hand, local '*I*' gives the information about the association of pixels in smaller neighbourhood which is important for image classification. Again, local '*I*' depends on the size of neighbourhood as well as on the selection of neighbouring pixels, e.g., *m*-neighbourhood. In order to decide the neighbourhood type different cases are to be considered, e.g., Rook's case, Bishop's case and Queen's case which implement 4-neighborhood, diagonal neighbourhood (*d*-neighbourhood) and 8-neighborhood respectively. It is obvious that selection of neighbourhood and hence the connectivity case is important and affects the value of '*I*'. The value of '*I*' lies between −1 and +1 such that the positive value shows higher association of neighbouring pixels and negative value shows opposite association of the pixels. The value 0 indicates no association, i.e., a random sequence of pixels [36, 48, 49]. Method for calculating Moran'sI is described in section-3.4.1.

Chapter 3

Methodology

In this chapter methodology adopted for data processing and to calculate child parameters are presented. Methodology for determining type of craters is presented then a statistical method is developed for identification of two craters types. Goodness of fit (GoF) tests are described then steps to determine best fit distribution function for CPR pixels are explained. Finally methodology for classification of lunar surface using texture properties of mini-SAR image is discussed. In this dissertation following software were used:

ENVI 4.3- Environment for Visualizing Images (ENVI) was for processing mini-SAR images. **MATLAB 2010b-** It is used to write algorithms to calculate fractal images and Moran'sI map from mini-SAR images.

3.1. Material used and study area

In this dissertation four channel mini-SAR images of Polar Regions (North Pole) is taken. For current study four scenes are selected as identified by strip no. FSR_CDR_LV2_01625_0R, FSR_CDR_LV2_01628_0R, FSR_CDR_LV2_01631_0R, FSR_CDR_LV2_01633_0R, taken on 22/03/2009, 22/03/2009, 23/03/2009, 23/03/2009 respectively. Fig.3.1 is a Google Earth image of North Pole of Moon, in Moon explorer view of Google earth to view location of these four scenes on Moon.
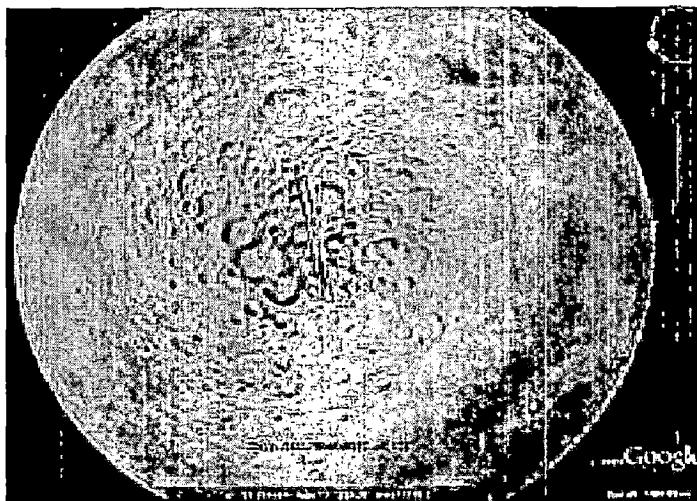
Figure: 3.1 North Pole image of Moon (Google Earth in Moon explorer)

19

3.2. Data Processing

Mini-SAR data was formatted and stored in a Planetary Data System (PDS) compliant standard where each pixel in an image strip consisted of 16 bytes data in four channels of 4 bytes each as $|LH|^2$, $|LV|^2$, Real (LH LV*) and Imaginary (LH LV*)[2-4]. Meaning of the notation LH means left handed transmission (L) and horizontal reception (H). The first two channels represent the intensity images for 'horizontal' and 'vertical' receive, respectively. The last two channels represent the real and imaginary components, respectively of the complex value for the cross power intensity image between the 'horizontal' and 'vertical' receive. These four channel raw data is used in this dissertation to analyze and classify lunar surface.

3.2.1. Stokes Vector

Four channel raw data $|LH|^2$, $|LV|^2$, Real (LH LV*) and Imaginary (LH LV*) are directly received data by mini-SAR sensor data without any processing. These data were used for deriving stokes vector for each pixel [2-4]. Stokes vector contains four parameters. These parameters can be described as:

- First parameter (S0): Total received power i.e. Sum of total power in inphase channel and in quadrature phase channel

- Second parameter(S1): Difference of power in inphase channel and in quadrature phase channel

- Third parameter (S2): Real part of cross channel received signal. It is important for retrieval of contained phase information.

- Fourth parameter (S3): Imaginary part of cross channel received signal. It is also important for retrieval of contained phase information.

Several useful parameters follows from stokes vector. Some of the important parameters are: degree of polarization (DoP or m), circular polarization ratio (CPR), LH-LV relative phase (δ) etc. Where, DoP gives information associated with polarized and diffuse scattering phenomenon, CPR represents scattering associated with volume scattering phenomenon and dihedral reflection (volume scattering is largely due to planetary ice and multiple reflection). Stokes vector can be derived using Eq. (3.1) for each pixel [2-4]

$$S_0 = \left\langle |E_{LH}|^2 + |E_{LV}|^2 \right\rangle$$

$$S_1 = \left\langle |E_{LH}|^2 - |E_{LV}|^2 \right\rangle$$

$$S_2 = 2\Re\left\langle E_{LH} E_{LV}^* \right\rangle$$

$$S_3 = -2\Im\left\langle E_{LH} E_{LV}^* \right\rangle$$

(3.1)

Where the 'E_{LH}' represents complex voltage received by the channel with left-circular transmit and horizontal polarization receive, 'E_{LV}' represents complex voltage received by the channel with left-circular transmit and vertical polarization receive, * indicates complex conjugate, < > represents the ensemble average.

3.2.2 Phase Calibration

Mini-SAR data was found to have a phase shift of 45° in the anti-clock-wise direction that resulted most of the lunar surface showing volume scattering characteristics which is not true. A phase correction for generating stokes vector's 3rd and 4th parameter is need to be done on Mini-SAR data to compensate for this phase shift before the data is processed for calculating any child parameters. Equations (3.2) and (3.3) show method for phase calibration for third and fourth Stokes' vectors. In Fig. 3.2(a and b), histogram for uncalibrated and calibrated δ is plotted, we can see that histogram shifts by 45° in calibrated graph of δ.

Re (LH LV*)$_{calib}$ = Re (LH LV*)$_{un}$ cos 45° - Im (LH LV*)$_{un}$ sin 45°   (3.2)

Im (LH LV*)$_{calib}$ = Re (LH LV*)$_{un}$ sin 45° + Im (LH LV*)$_{un}$ cos 45°   (3.3)

Where subscript, *un* stand for uncalibrated data.
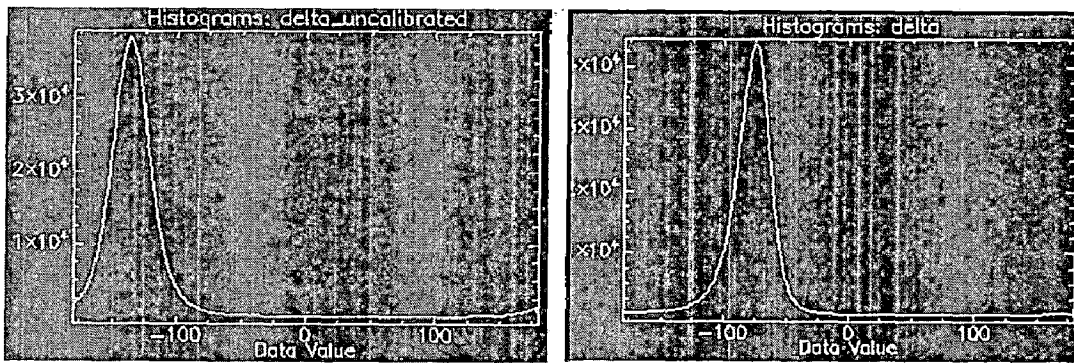
a) Uncalibrated LH-LV relative phase   b) Calibrated LH-LV relative phase

Figure: 3.2 Histogram of LH-LV relative phase (δ)

21

3.3 Generation of child parameters

After the phase calibration stokes vector can be used to determine various parameters as discussed in previous section. Which give different polarimetric information regarding scattering nature of surface, these parameters are called child parameters. Following equations explain how child parameters can be calculated from stokes vector [2, 3, 4]

- **Degree of Polarization** *(m)*: It is fundamentally related to entropy (E). **Degree of polarization** (DoP) is a quantity used to describe the portion of an electromagnetic wave which is polarized. A perfectly polarized wave has a DoP of 1, whereas an unpolarized wave has a DoP of 0. A wave which is partially polarized, and therefore can be represented by a superposition of a polarized and unpolarized component, will have a DoP somewhere in between 0 and 100%. DoP is calculated as the fraction of the total power that is carried by the polarized component of the wave Eq. (3.4).

$$m_L = \left(S_1^2 + S_2^2 + S_3^2\right)^{1/2} / S_0 \qquad (3.4)$$

- **Degree of Linear Polarization** *(m_L)*: This is indicator of volume vs subsurface/surface scattering. It gives a measure of power in linearly polarized component of electromagnetic wave.

$$m_L = \left(S_1^2 + S_2^2\right)^{1/2} / S_0 \qquad (3.5)$$

- **Relative Phase:** This is a sensitive indicator of scattering mechanism associated with surface. A distributed δ occurs for dominant volume scatterers, clustered around +90° and around -90° reflects double bounce and surface scattering mechanism respectively.

$$\delta = tan^{-1} \ S_3 / S_2 \qquad (3.6)$$

- **Degree of circular polarization** *(m_c)*: m_C is positive for right-handed circular polarization and negative for left-handed circular polarization. Together with linear polarization ratio it gives nature of polarization in a completely polarized r partially polarized wave. It gives a measure of power in circularly polarized component of electromagnetic wave.

$$m_C = S_3 / S_0 \qquad (3.7)$$

- **Circular Polarization Ratio (μ_c):** This is indicator of scattering associated volume scattering phenomenon along with dihedral scattering for $\mu_c > 1$

$$\mu_C = (S_0 - S_3)/(S_0 + S_3) \qquad (3.8)$$

- **Linear Polarization ratio:** It gives ratio of polarized power contained in horizontal component and in vertical component.

$$\mu_L = (S_0 - S_1)/(S_0 + S_1) \qquad (3.9)$$

3.4 Methodology for 'm-δ' decomposition

'm-δ' decomposition presents a method to determine type of scattering phenomenon associated with a region. Models of different scattering mechanism are discussed in section-2.3, Fig.2.3.

- **Volume scattering:** Modelled by a set of randomly oriented dipoles.

- **Double-bounce scattering:** Modelled by scattering from a dihedral corner reflector.

- **Single-bounce scattering:** Modelled by a first-order Bragg surface scatterer.

Degree of polarization (m) can be calculated using Stokes parameters using Eq. (3.4). Degree of polarization of a scattered wave provides information on the randomness of the scattering phenomenon from natural targets [50, 51], because value of 'm' depends on the effect of multiple reflections. Hence, degree of polarization value could be used as an important factor for classifying images. For example, the bare surface or buildings have high degree of polarization values because there are only simple reflections, while the forest or pastures have low values because it contains various multiple reflections. Scattering decomposition of polarimetric mini-SAR data is done to understand the predominant scattering type from a single or averaged resolution cell. It is known that buried water ice on lunar surface exhibits volume scattering phenomenon and only due to this reason they also have CPR>1. Apart from CPR and degree of polarization relative LH-LV phase (δ) are also important parameters to study the scattering mechanisms associated with lunar surface. The 'm-δ' together indicates the type of scattering mechanism associated with the target. For higher m value along with 'δ' values close to -90° and +90° indicates 'surface' and 'double-bounce' scatterings respectively, where a distributed values of δ in a region indicate 'diffused' scattering mechanism.

If, we intersect the regions having CPR>1 with regions having volume scattering phenomenon we get regions having high probability of planetary water-ice particles. Because it is explained by Spudis et.al [2-4] that regions having possibility of planetary water-ice particles have CPR>1 and such regions exhibits volume scattering phenomenon. Thus we can also say those regions which do not exhibit dominant volume scattering phenomenon cannot contain planetary water-ice particles.

'm-δ' decomposition gives fractions of power contained in different scattering phenomenon. Using Eq. 3.10-3.12 fraction of power in surface, double bounce and in volume scattering mechanism can be calculated. Further using these three values as source for three primary colours (RGB) we get a coloured image.

$$f_{surface}(R) = \sqrt{\frac{S0 \times m \times (1 - \sin(\delta))}{2}} \tag{3.10}$$

$$f_{double-bounce}(B) = \sqrt{\frac{S0 \times m \times (1 + \sin(\delta))}{2}} \tag{3.11}$$

$$f_{volume}(G) = \sqrt{S0 \times (1 - m)} \tag{3.12}$$

Where, S_0 is the first element of Stokes vector and 'm' and 'δ' are child parameters derived from stokes vector and have their usual meanings. For possibilities of planetary water-ice particles i.e. dominant volume scattering

$$f_{volume} > f_{double-bunce} + f_{surface} \tag{3.13}$$

Eq. (3.13) can be solved to get Eq. (3.14)

$$\sqrt{\frac{(1 - \sin(\delta))}{2}} + \sqrt{\frac{(1 + \sin(\delta))}{2}} < \sqrt{\frac{(1 - m)}{m}} \tag{3.14}$$

Eq. (3.14) satisfies for the value of m<0.33, however there isn't any damage done if m=0.35 is taken as threshold value to determine dominant scattering mechanism. For diffused scattering phenomenon DoP should have value lesser then 0.35 and 'δ' should have distributed histogram for that region. So, if a pixel belongs to a ROIs which has distributed δ and satisfies the conditions CPR>1 and m<0.35 has higher possibility of having planetary water-ice particles. Thus applying the conditions stated above, a flow chart is developed for

identifying type of scattering behaviour of crater and thus to differentiate type-I craters and type-II craters.

```
┌──────────────────────────────┐
│   Determine Stokes Vector    │
└──────────────────────────────┘
              ⇩
┌──────────────────────────────┐
│   Generate DoP (m) and Delta │
│            maps              │
└──────────────────────────────┘
              ⇩
┌──────────────────────────────┐
│ Select ROIs from crater regions │
└──────────────────────────────┘
              ⇩
      ◇ If for large no of pixels
        in a ROI m<0.35 &        ──No──▶  ┌──────────────────────┐
        CPR>1                              │  It's a Type-II Crater │
                                           └──────────────────────┘
              ⇩ Yes

      ◇ If histogram of delta for
        that ROI is distributed   ──No──▶  ┌──────────────────────┐
                                           │  It's a Type-II Crater │
                                           └──────────────────────┘
              ⇩ Yes

┌──────────────────────────────┐
│     It's a Type-I Crater     │
└──────────────────────────────┘
```
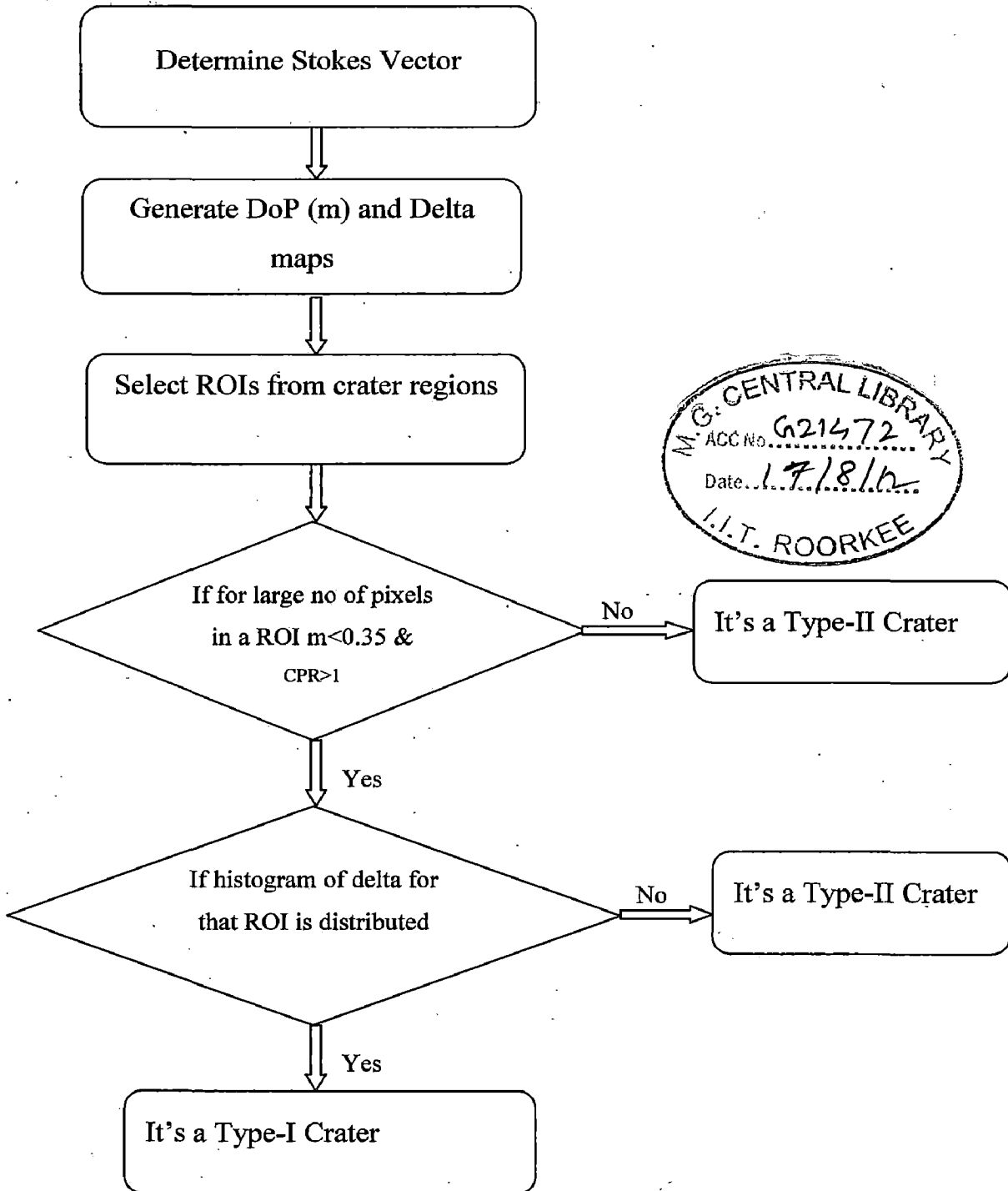
Figure: 3.3 Flow chart for differentiating type-I and type-II craters

25

3.5. Statistical analysis of mini-SAR data

This section first explains methodology adopted for determining best fit density function and the steps followed for the pattern analysis techniques to differentiate two crater types based on distribution behaviour of CPR. Circular polarization ratio (CPR) is an important parameter in study of lunar surface. As introduced earlier in section-1.1 that initial conclusion of **Chandrayan-I** mission was that regions having CPR>1 will be regions having planetary water-ice particles mixed in lunar surface but further investigation and results proved that CPR>1 can arises also in regions which are highly rough in nature and exhibits double bounce scattering phenomenon [2-4] So, it's not possible to say with conclusively that a region has CPR>1 is due to frozen ice or due to rough nature of surface, pixels having CPR>1 value are found primarily in craters regions, (Fig.3.4 is a cropped image for CPR of scene "FSR_CDR_LV2_01633_0R" showing abnormal behaviour of CPR pixels in crater regions, red pixels are masked for CPR>1), so first step for developing the pattern analysis technique to identify different crater types is determination of best fitted distribution function for CPR pixels in crater regions. Also, CPR is a very important parameter in study of lunar surface. So, it's important to study distribution behaviour of CPR pixels and to determine best fitted distribution function to represent it. Best fit density function can be determined using goodness of fit tests as discussed in section-2.4. In this section methodology to perform goodness of fit test is presented.

Description of GoF tests

The three GoF test studied for determining the fitness of a distribution are:

        i) Kolmogorov–Smirnov test [19, 20]
        ii) Anderson–Darling test [20, 21]
        iii) Chi Square test [20, 22]
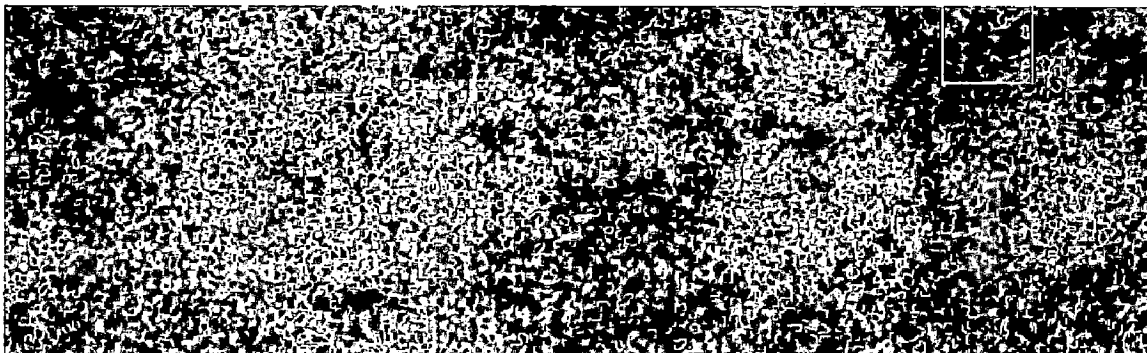
Figure: 3.4 CPR image of a small region from scene "FSR_CDR_LV2_01633_0R", red colour pixels shows pixels having CPR>1

26

i) Kolmogorov-Smirnov test

Kolmogorov-Smirnov (K-S) test can be described as it's based on the empirical cumulative distribution function (ECDF). Given N ordered data points Y_1, Y_2, ..., Y_N, The ECDF is defined as (3.15)

$$E_N = n(i)/N$$

(3.15)

Where, $n(i)$ is the number of points less than Y_i and the Y_i are ordered from smallest to largest value. This is a step function that increases by $1/N$ at the value of each ordered data point. Once an empirical density function is chosen for test, the K-S test calculates the maximum distance 'D' between these two curves E_N and empirical function, lesser the value of 'D' better the distribution is represented by the statistical model in test. 'D' for this test can be calculated using (3.16).

$$D = \max_{1 \le i \le N}\left(F(Y_i) - \frac{i-1}{N}, \frac{i}{N} - F(Y_i) \right)$$

(3.16)

Where, 'F' is the theoretical cumulative distribution function of the distribution being tested. Which must be a continuous distribution (i.e., no discrete distributions such as the binomial or Poisson), and it must be fully specified (i.e., the location, scale, and shape parameters cannot be estimated from the data) [19, 20].

ii) Anderson-Darling test

The Anderson-Darling test is used to test if a sample of data came from a population with a specific distribution. It is a modification of the Kolmogorov-Smirnov (K-S) test and gives more weight to the tails than does the K-S test. The K-S test is distribution free in the sense that the critical values do not depend on the specific distribution being tested. The Anderson-Darling test statistic is defined as

$$A^2 = -N - S$$

(3.17)

Where,

$$S = \sum_{i=1}^{N} \frac{(2i-1)}{N}[\ln F(Y_i) + \ln(1 - F(Y_{N+1-i}))]$$

(3.18)

F is the cumulative distribution function of the specified distribution. Y_i are the ordered data [20, 21].

iii) Chi-Squared test

The chi-squared test is also known as Pearson's chi-square test. The chi-square goodness-of-fit test is applied to binned data (i.e., data put into classes). However for non-binned data we can calculate a histogram or frequency table before applying the chi-square test. However, the values of the chi-square test are dependent on how the data is binned this dependency of binning has lesser effect if we have large number of data points. Another disadvantage of the chi-square test is that it requires a sufficient sample size in order for the chi-square approximation to be valid. The chi-square goodness-of-fit test can be applied to continuous as well as discrete distributions, such as the binomial and the Poisson. For the chi-square goodness-of-fit computations, the data are divided into k bins and the test statistic value (χ^2) is defined in equation (3.19):

$$\chi^2 = \sum_{i=1}^{k} (O_i - E_i)^2 / E_i$$

(3.19)

Where, O_i is the observed frequency for bin i and E_i is the expected frequency for bin i. The expectation is calculated by equation (3.20).

$$E_i = N(F(Y_u) - F(Y_l))$$

(3.20)

Where, F is the cumulative distribution function for the statistical model being tested, Y_u is the upper limit for class i, Y_l is the lower limit for class i, and N is the sample size. Critical values of χ2 for accepting or rejecting a hypothesis can be found in Appendix-II for different confirmation values [20, 22].

3.5.1. Steps to determine best fit density function

Fig.3.5 is flow chart for the method followed to determine best density function which can be used to represent distribution of circular polarization ratio (CPR) effectively. For the determination of best fitted distribution function a large number of homogeneous regions of interest (ROIs) are selected for different regions of craters.

28
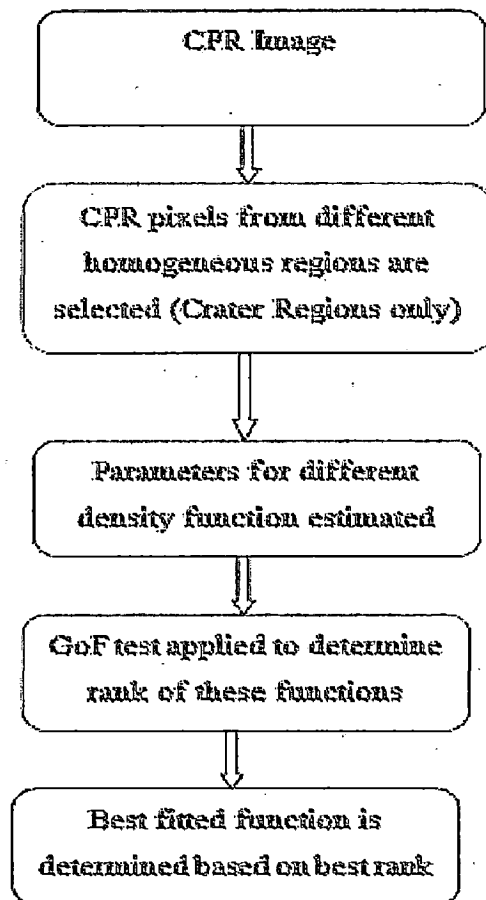
Figure: 3.5 Steps to determine best fit distribution function

Selection of homogeneous ROIs

Crater regions can be divided into three regions as shown in Fig.3.6

- **Base of craters**
- **Rim of craters**
- **Outer rim (edge) of crater**
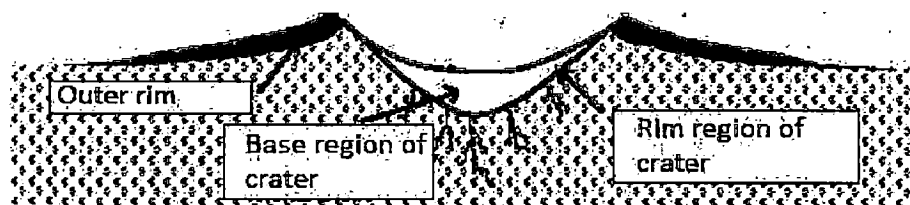
Figure: 3.6 Different regions of a crater [3]

29
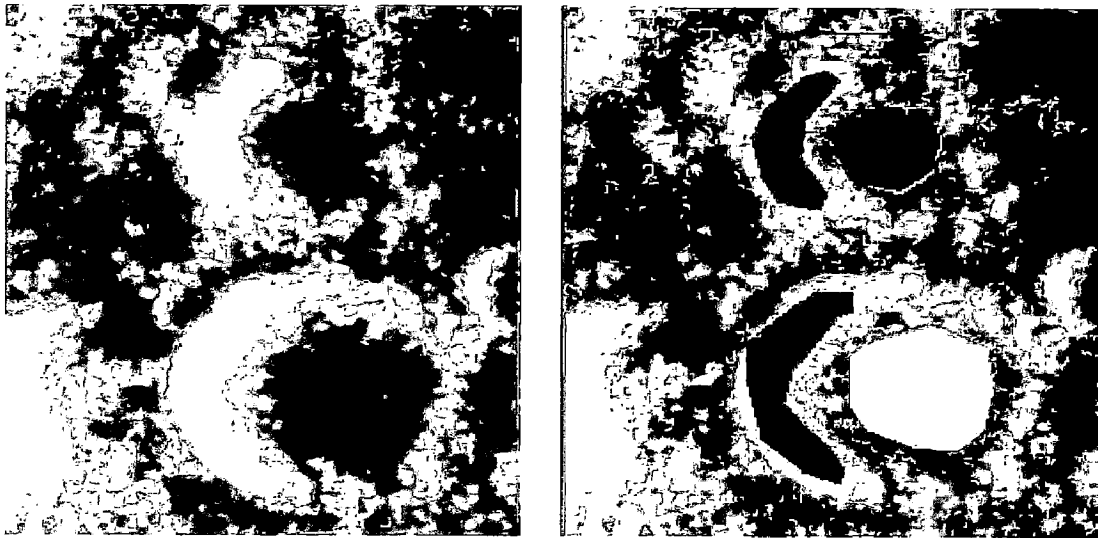
a) Total intensity image   b) Selected homogeneous ROIs

Figure: 3.7 Depicting the procedure of homogeneous ROI selection

Homogeneous ROIs for rim and base regions are selected using total intensity image which is S0 of stokes vector, homogeneous region of interest means regions where pixel value does not vary too much. Outer rim (edge) is not considered in this analysis because it is not possible to identify homogeneous region of interest for the outer edge and as its size is too small when compared to inner rim or base regions so this region is excluded. Fig.3.7 (a, b) shows how homogeneous ROIs are selected. ROIs shown in yellow and green colour are a base region and in blue and red are inner rim regions. Then GoF tests are applied on CPR data for each and every ROI to test the fitness of different well known probability distribution functions (Beta, Kumarswamy, Johnson, Generalized Extreme Value, Log-Pearson, Weibull etc.) on these ROIs. Since, it is found that 99.95% CPR pixels are in the range of 0 to 2 so GoF tests are applied for bounded distributions. For every ROI five best fitted distribution functions are selected according to Chi-square test. Number of occurrence of each density function is calculated and a table is formed. From the table best fitted density function can be determined.

3.5.2. Methodology for pattern analysis

Probability density based classification technique also known as pattern analysis is primarily used for differentiating two targets; It has been used for target classification in through wall imaging [52]. It is based on the property that best fit probability density functions for similar type of targets have high correlation between them thus there shape and location parameters are closely related with each other. To be able to apply pattern analysis technique to identify

30

two different structures, it is important to determine best fitted distribution function and then to estimate parameters of best fitted density function for a large number of observations for known structure types. Then the range of shape and location parameter for the best fit density function is determined. In current study this technique is applied to CPR image of crater regions to identify two types of craters. As given in [2-4] that CPR>1 is necessary condition to have any probability of finding planetary water-ice particles apart from this condition, it is also necessary that such regions exhibit volume scattering behaviour and not double bounce. It is therefore informative to investigate the distribution of CPR value for both types of crater regions and to develop a method to differentiate two craters which satisfy the 'm-δ' decomposition criterion and which does not satisfy the 'm-δ' decomposition criterion based on distribution of CPR pixels. For this purpose sufficiently large number of craters is selected in order to detect and differentiate them more accurately. These craters were divided in two groups one which satisfies the 'm-δ' criterion and one which doesn't satisfy 'm-δ' criterion using 'm-δ' technique.Then the result is used as training data for pattern analysis. Once the best fit density function to represent distribution of CPR pixels is known this technique can be applied to identify crater types. In section-4.1.1 it will be shown that CPR is best represented by Generalized Extreme Value distribution function.
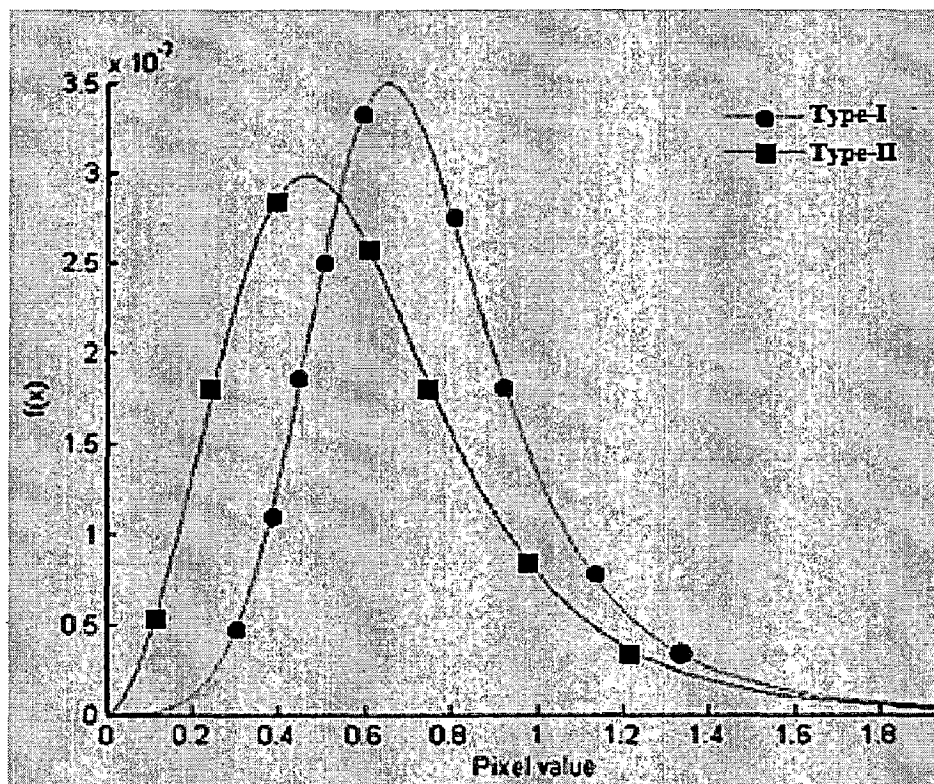
Figure: 3.8 Graph of best fitted distribution for CPR for two types of crater

The parameters of Gen. Extreme Value functions i.e. shape, scale and position parameters (k, μ, and σ) for different crater regions are estimated using maximum likelihood estimator. It is observed that distribution graphs (an example is shown in Fig.3.8) of CPR pixels for type-I craters are shifted towards higher value compared to graphs for type-II craters. This shift in CPR distribution can be used to differentiate these curves and hence the craters can be labelled as type-I and type-II. [52].

Determination of range of parameters

For determining range of position and scale parameter for different types of crater, position and scale parameter of those craters estimated whose type is already known are identified. Then mean and standard deviation of 'μ' is calculated for all the craters. Then upper and lower boundaries of both the parameters ('μ' and 'σ') for each type of craters are calculated using Eq. (3.21)

$$LowerBoundary = mean - std.dev.$$
$$UpperBoundary = mean + std.dev.$$

(3.21)

For the calculation of range for type-I crater mean and std. dev. of type-I craters and for the calculation for range of type-II craters mean and std. dev. of type-II craters will be used.

3.6. Classification of mini-SAR Images using Fractals and Moran's *I*

The classification of mini-SAR images has been done by using fractal images of mini-SAR data and analysis based on spatial correlation of images using Moran's *I* values for different local windows sizes.

3.6.1 Methods to calculate fractal dimension and Moran's *I*

Triangular Prism Surface Area Method (TPSAM)

It is the most widely known method for estimating fractal dimension which was proposed by Clarke [44-46]. The image pixels are considered as columns having heights equal to their digital number value. The pixel columns are considered for generating the prism in 3D space with four pixels at four corners and their average as the central pixel. These five points generate four triangular prisms in 3D space, whose upper surface areas are estimated and added to obtain the whole surface area. The triangular prism generated from image pixels is
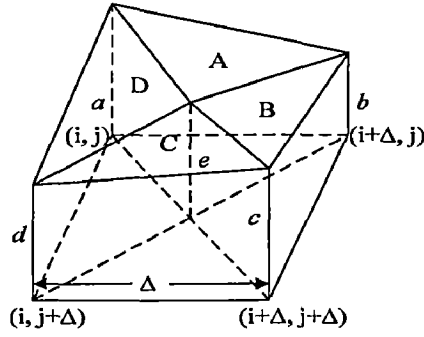
Figure: 3.9 Triangular prism generation from image pixels [44]

shown in Fig.3.9, four pixels are considered which are separated by a distance Δ which are at locations (i, j), (i+Δ, j), (i+Δ, j+Δ) and (i, j+Δ). The pixel values are assumed to make the height columns named as a, b, c and d respectively at these four pixels. The average of these four corner pixel values is e which also generates the middle height column. By joining the top points of these five height columns and assuming thus obtained triangles four triangular prisms are generated whose top triangular areas are represented by A, B, C and D respectively.

Thereafter, the surface area is estimated for different bases generated by corner pixels values, which keeps track with the resolution of base of triangular prism area. For different values of base resolution, total surface area is estimated and plotted against the base area in a log-log scale. The slope of the least square fit line is subtracted from two to calculate the fractal dimension, i.e.

$$D = 2.0 - \text{Slope}. \tag{3.22}$$

The total surface area decreases as the base resolution increases [35, 44], the slope comes to be negative in general and hence the value of 'D' becomes greater than 2.0. The base resolution is increased in power of 2 in original method, i.e. 2, 4, 8, 16, and so on. The method is based on the variation of pixel values in 3D space in terms of the surface area showing the distribution of image points. The pixel values showing low variation correspond to smooth surface and thus give high value of slope and consequently low fractal dimension.

Differential box counting method (DBC)

The method, called differential box counting (DBC) method [35, 43] is described below. As fractal dimension 'D' is given by Eq. (2.9). It is rewritten here for convenience

$$D = \frac{\log(N_r)}{\log\left(\dfrac{1}{r}\right)}$$

33
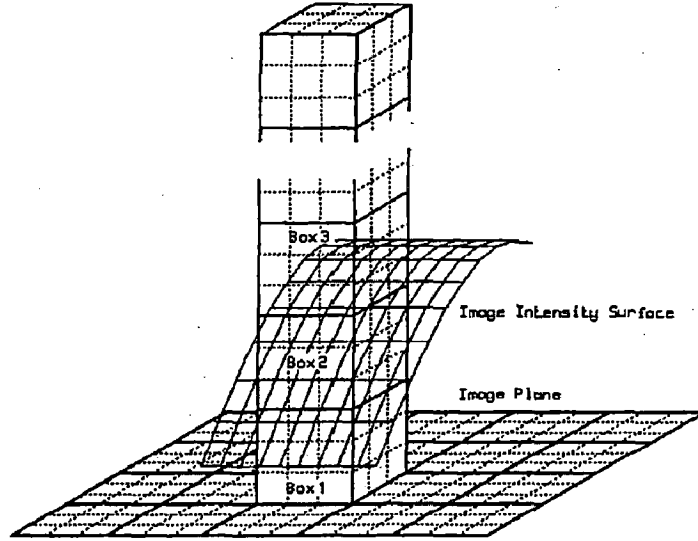
Figure: 3.10 Determination of Nr by DBC method [43]

In the DBC method, N_r, is counted in the following manner. Consider that the image of size M x M pixels has been broken down to a grids of size s x s, where $M/2 \geq s > 1$ and s is an integer. Then we have an estimate of $r = s/M$. Consider the image as a 3-D space with (x, y) denoting 2-D position and the third coordinate (z) denoting the gray level i.e. image intensity. The (x, y) space is partitioned into grids of size s x s. Each grid is further partitioned into a column of s' boxes. So, entire image is partitioned into boxes of size s x s x s'. If number of gray level is G then $\lfloor G/s' \rfloor = \lfloor M/s \rfloor$.

In figure Fig.3.10 where, s=s'=3 assumed. Boxes are numbered 1, 2, 3..... If the minimum and maximum gray level of the image in the (i, j)th grid fall in the box numbered k and l, respectively. Eq. (3.23) gives the contribution of N_r, for the (i, j)th grid.

$$n(i,j) = l - k + 1 \tag{3.23}$$

For the example given in Fig.3.10, n(i, j)=3-1+1. Taking contributions from all grids, we have

$$N_r = \sum_{i,j} n(i,j) \tag{3.24}$$

N_r, is counted for different values of r (i.e. different values of s). Then using Eq. (2.9) the fractal dimension 'D' can be estimated from the least-squares linear fit of $\log(N_r)$ against $\log(1/r)$ [43-45].

Method for the determination of Moran'sI

·Moran'sI (Moran 1950) tests for global spatial autocorrelation for continuous data [53]. It is based on cross-products of the deviations from the mean and is calculated for n observations on a variable x at locations (i, j) by Eq. (3.25):

$$I = \frac{n}{S_0} \frac{\sum_i \sum_j w_{ij}(x_i - \bar{x})(x_j - \bar{x})}{\sum_i (x_i - \bar{x})^2}$$

(3.25),

Where, $\bar{x}$ is the mean of the x variable, w_{ij} are the elements of the weight matrix, and S_0 is the sum of the elements of the weight matrix:

$$S_0 = \sum_i \sum_j w_{ij}.$$

(3.26)

Moran'sI is similar but not equivalent to a correlation coefficient. It varies from -1 to +1. In the absence of autocorrelation and regardless of the specified weight matrix, the expectation of Moran'sI statistic is $-1/(n-1)$, which tends to zero as the sample size increases.

Weight Matrix

To assess spatial autocorrelation, one first needs to define what is meant by two observations being close together, i.e., a distance measure must be determined. These distances are presented in weight matrix, which defines the relationships between locations where measurements were made. If data are collected at n locations, then the weight matrix will be $n \times n$ with zeroes on the diagonal [53].

- The weight matrix can be specified in many ways:
- The weight for any two different locations is a constant.
- All observations within a specified distance have a fixed weight.
- K nearest neighbours have a fixed weight, and all others are zero.
- Weight is proportional to inverse distance, inverse distance squared, or inverse distance up to a specified distance.

Other weight matrices are possible. The weight matrix is often row-standardized, i.e., all the weights in a row sum to one but not necessarily.

35

Local fractal dimension can be defined as the fractal dimension of a predefined pixel neighbourhood known as local window. In general, the window is odd sized square mask of pixels where a fixed central pixel exists and works as the representative of window. The role of such a window is obvious because the textural features of the window get changed as the size of window changes. Since the local windows are given sizes as 5x5, 7x7 and so on, the fractal dimension of the window changes with its size. Thus, it is important to highlight the role of window size in such studies because it affects the final results. The local fractal dimension provides a fractal map when the local window is moved over the image sequentially. As the fractal map represents the values of fractal dimension only, it maps the actual image into a fractal domain. Thus, local fractal map provides a textured image of the original image which is dependent on the size of local window. Using various window sizes, different texture images are obtained. It is useful for our study in comparing different textures based on local window size. Some of the features are highlighted for a particular window size. It is interesting to find out such features and hence the appropriate window size. It is important to note that this event is not useful for overall classification but used for identification of some particular area or point in the image based on its neighbouring pixel arrangements.

3.6.2. Methodology for classification

In this section 'D', 'I' and 'S' notations are used for fractal map, Moran's I map and for original power intensity map respectively.

The fractal based approach deals with the textural ('D' for fractal & 'I' for Moran's I) maps generated by applying a moving window approach for different window sizes within which local fractal dimension and Moran's I is estimated for whole image. The flowchart of the methodology adopted for classification purpose is shown in Fig.3.11 first step requires selection of local window size. We have chosen the local window to be of odd size, i.e., 5×5, 7×7, and so on till 15×15. In second step local fractal dimension and local Moran's I are estimated for these window sizes and corresponding D-maps and I-maps are generated. For each D-map, clustering is performed for five different classes using 'D' values. The next step used as the sub step of previous one considers the I-map for clustering.

```
                    ┌─────────────────────┐
                    │     SAR Image       │
                    └─────────────────────┘
                               │
                               ▼
          ┌──────────────────────────────────────────┐
          │  Selection of Local Window Size 5,7,...,15 │
          └──────────────────────────────────────────┘
                               │
                               ▼
          ┌──────────────────────────────────────────┐
          │   Estimation of Local D and Local I       │
          │                   &                       │
          │   Generation of D-Map and I-Map           │
          └──────────────────────────────────────────┘
```
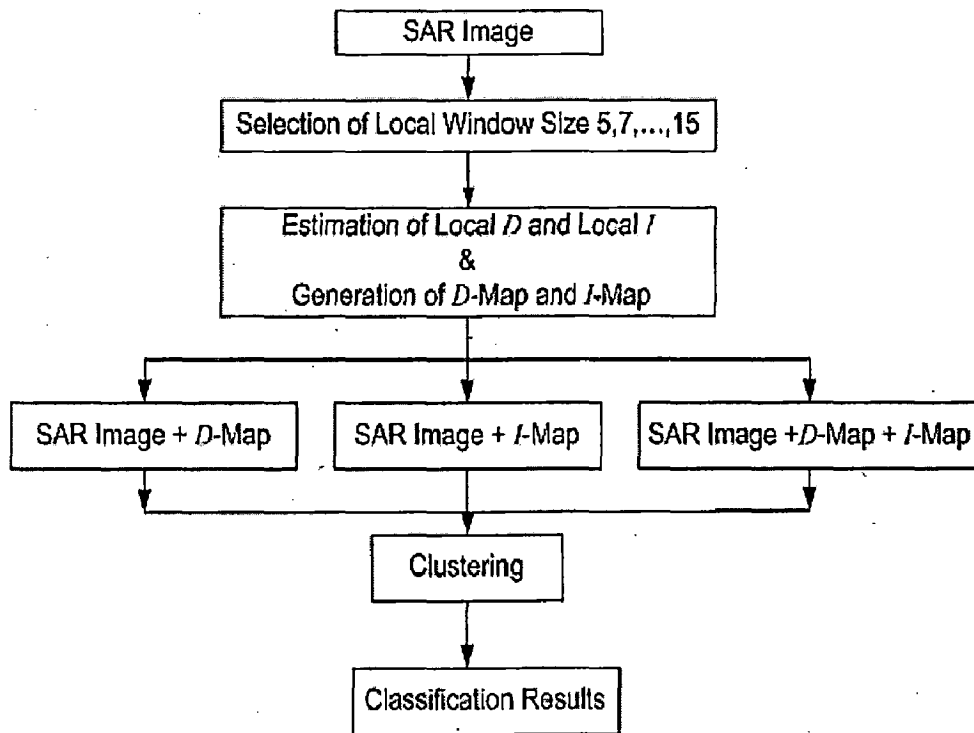
Figure: 3.11 The Flowchart of the methodology used [35]

Based on 'I' values, the clusters are generated using K-means algorithm. In third step, the 'D' values are added with the image pixel values and the combination of these two features, i.e., pixel values and 'D' values are used for clustering before addition normalization of 'D', 'I' and image pixels(S) are done. For the compatibility of sizes, the original image is resized to be equal to that of fractal and Moran'sI map. The image comprising the pixel values and fractal dimension values highlight some features clearly. By addition of fractal dimension to the pixel values, both the original information and the textural information are available for land feature identification. Thus, the clustering based on pixel values combined with 'D' values is better than that of individual 'D' values. The next sub-step includes the combination of pixel values with 'I' values. In this step the addition of pixel values with 'I' values is considered and the combined image thus obtained again highlights some of the surface features more clearly. The land features, which are agglomerated, like crater region area, are easily identified in the combined images. Since Moran's 'I' is sensitive for heaped structures (e.g. crater edges), the combination of pixel values with 'I' values is able to identify such land features better than the pixel values or 'I' values considered individually. The clustering is now performed on the combined image and the process is repeated for different selected windows.

Fourth step combines all the texture images, i.e., it includes the original image, fractal map and the I-map. As expected, this image is able to identify the features more clearly. Finally, the combined image is classified for five classes using the K-means algorithm. For different selected window sizes, the combined images are generated and the clustering is performed. For the compatibility of size, the image resizing is performed for each selected window as previously done. Using moving window approach, the local fractal dimension is estimated with TPSAM and DBC method and corresponding fractal maps are used for classification purpose. One imperative issue in estimation of local fractal dimension is selection of local window. Generally, the local window is considered to be of odd size square window which gets the benefit of having a unique centre pixel. Though, accuracy of this classification cannot be calculated due to unavailability of ground reference points on Moon but a comparison is done for different classes and whatever available terrain map. The importance of window size lies in the fact that once the window size is changed, textural information of the image gets changed which may change the class of a pixel. Since, accuracy of classification depends on size of local window size but accuracy of classification cannot be determined due to unavailability of ground truth points. So, optimization of window size cannot be performed so results for different window sizes are presented here therefore in this chapter a thorough systematic analysis of classified maps has been carried out for varying window size.

Chapter 4

Implementation, Results and Discussion

4.1 Generation of stokes vectors

After the pre-processing of mini-SAR data, parameters of stokes vector are generated according to the formulae given in section-3.2.1. Images of generated stokes vector for a part of region from scene "FSR_CDR_LV2_01633_0R" are shown in Fig.4.1. One side of crater walls are highly illuminated compared to other half, it's because one side of the wall was facing directly towards the mini-SAR sensor while other war hidden due to its slope.

a) S0   b) S1   c) S2   d) S3
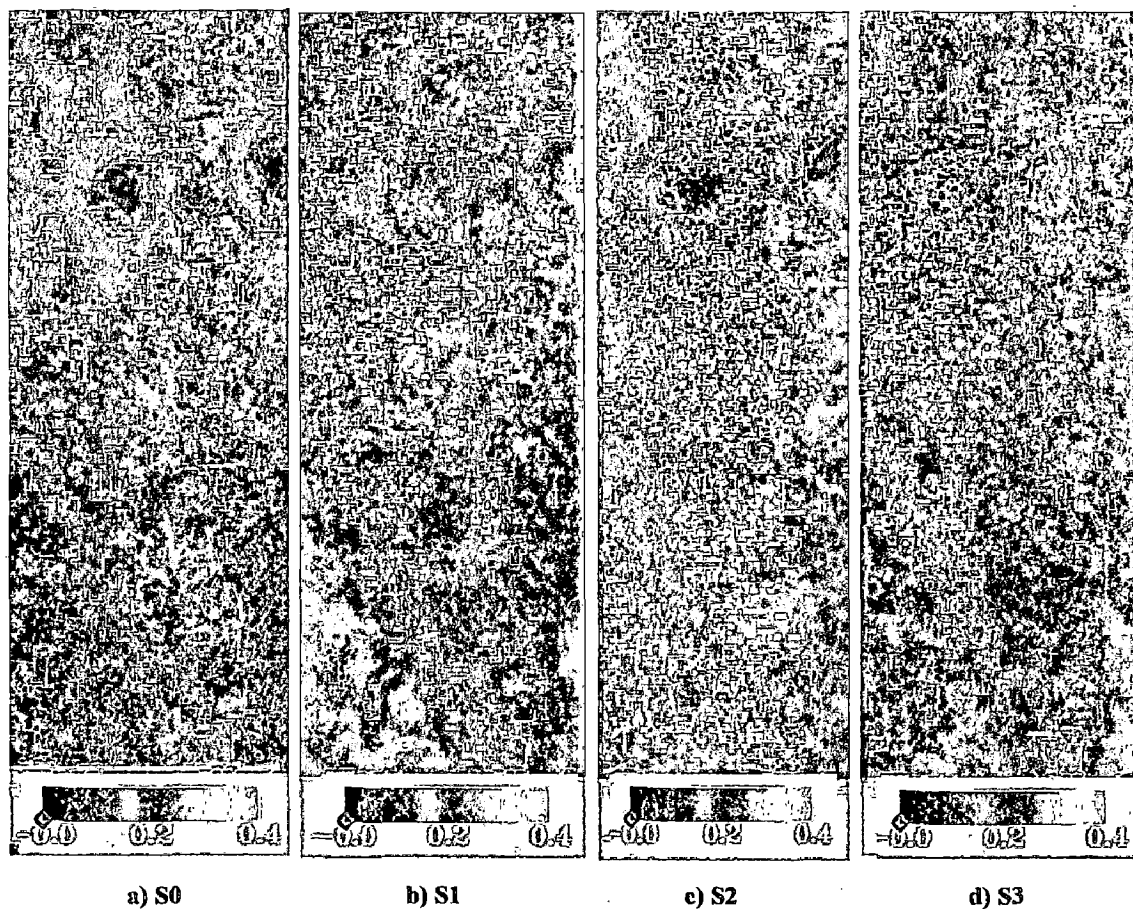
Figure: 4.1 Elements of stokes vector

(a) Histogram of S0

(b) Histogram of S1

(c) Histogram of S2
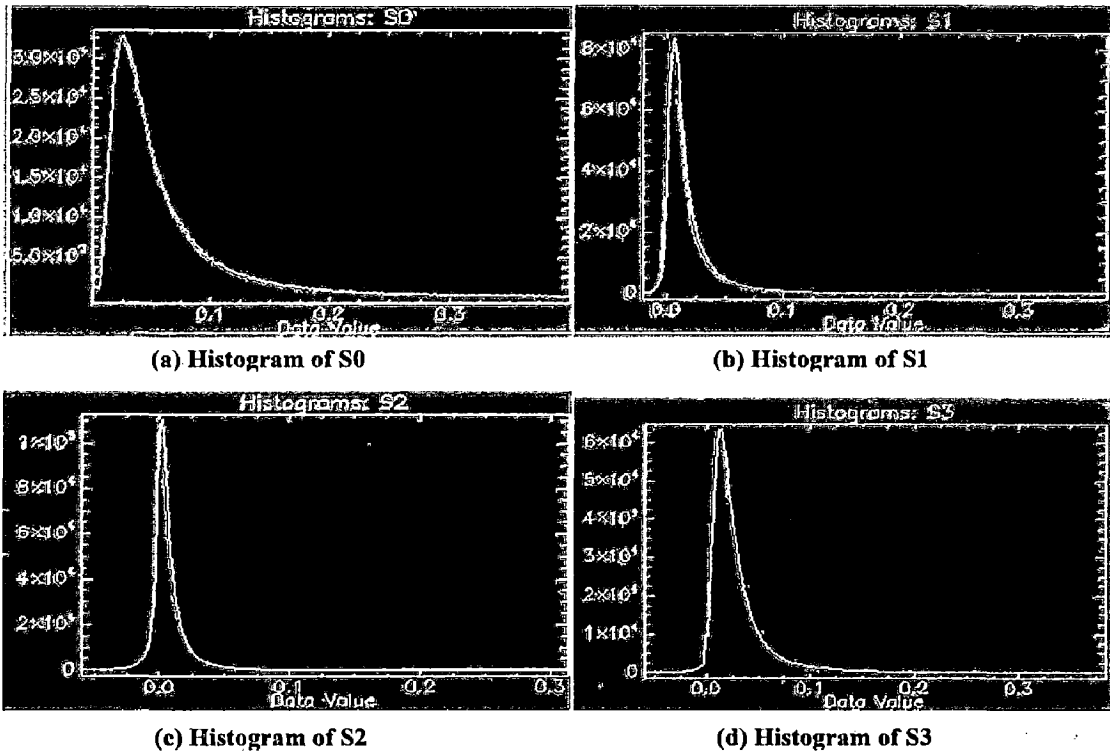
(d) Histogram of S3

Figure: 4.2 Histogram of elements of stokes vector

Pixel values for S0, S1, S2 and S3 are limited in the range of 0-0.4. However there are few pixels which have abnormally higher value and thus the histogram of these data have a long tail, shown in Fig.4.2 (a-d). 'S0' do not contain negative value but 'S1', 'S2', 'S3' contain few pixels which have negative value and it can be confirmed from histograms of these data value that negative pixels are indeed very less in number. The reason for such discrepancy could be random instrumentation errors. Table-4.1 summarizes the statistics of stokes vector elements.

Table-4.1

Statistics of stoke vector

Parameter	Minimum	Maximum	Mean	Std.Deviation	% of Pixel (x<0.4)
S0	0.000000	25.917572	0.079271	0.241871	98.8433
S1	-0.283528	13.310391	0.025636	0.107413	99.6398
S2	-0.889359	5.438548	0.009656	0.044372	99.8877
S3	-0.363855	20.891930	0.038152	0.163703	99.6034

4.2. Implementation for polarimetric parameters

(a) CPR   (b) Degree of polarization   (c) Degree of linear polarization (d) Delta

Figure: 4.3 Child parameters

(a) CPR   (b) Degree of Polarization

(c) Degree of linear polarization   (d) Delta

Figure: 4.4 Histogram of child parameters

41

Polarimetric parameters or child parameters from stokes vector are calculated using the procedure explained in section-3.3. Snapshot of child parameters for a part of mini-SAR image from scene "FSR_CDR_LV2_01633_0R" are shown in Fig.4.3. In Fig.4.4 histograms of various child parameters are plotted.
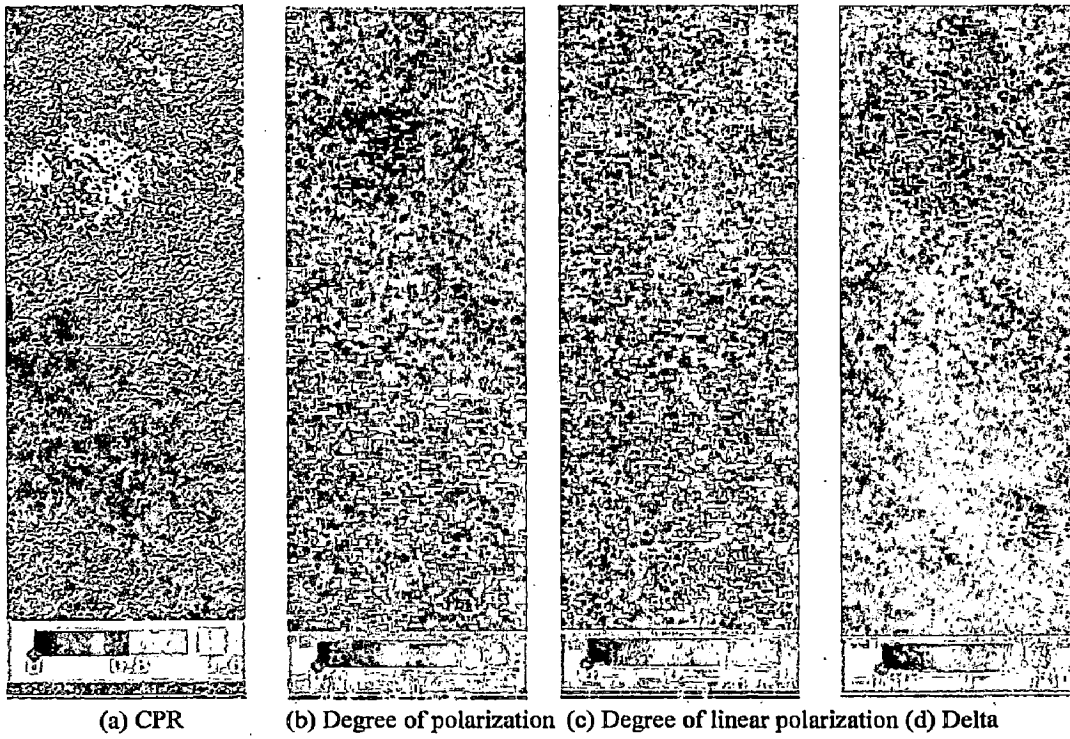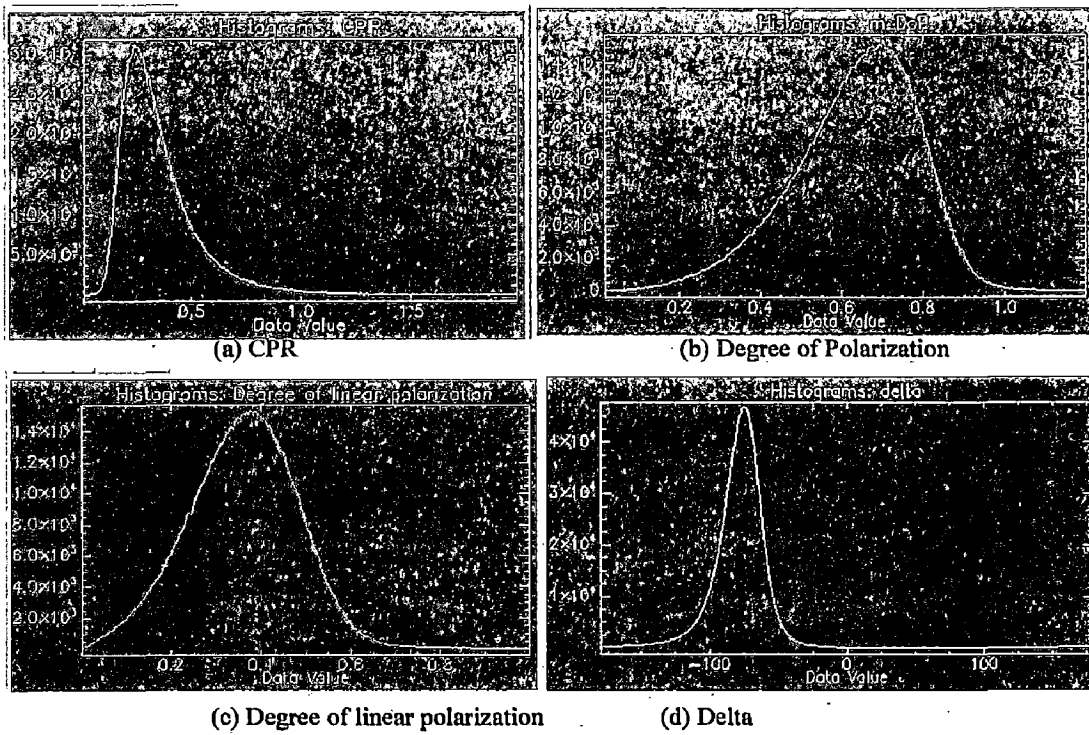
From these images some general conclusions are drawn as listed below.

- No. of pixels having CPR>1 is very high in crater regions compared to non-crater regions. Non-crater regions have much lesser no. of pixels having CPR>1.

- Regions having low CPR have higher degree of polarization (m) and vice-versa. These two images are approximately complementary of each other.

- CPR ranges between 0-1.6, though a small tail lasts up to CPR<2.

- Degree of linear polarization follows the trend of DoP but with less clustering.

- Crater regions have δ value clustered around 180°.

- Non-crater regions have very lesser no. of pixels around 180°

- δ value is clustered around -90° when entire image is considered.

4.2.1 Statistics of child parameters in craters

In this section statistics of child parameters for sixteen craters are shown. These craters were selected from scene "FSR_CDR_LV2_01628_0R" and "FSR_CDR_LV2_01633_0R In Fig. 4.6 statistics for CPR, in Fig.4.7 statistic for DoP, in Fig. 4.8 statistics for δ and in Fig. 4.9 statistics for linear polarization ratio is shown for these sixteen craters. In these graphs on X-axis crater number (crater identification number) and on Y-axis value of minimum, maximum, mean and standard deviation for each parameter is plotted. The location of these craters are shown in Fig.4.5

a) "FSR_CDR_LV2_01633_0R"   b) "FSR_CDR_LV2_01633_0R"
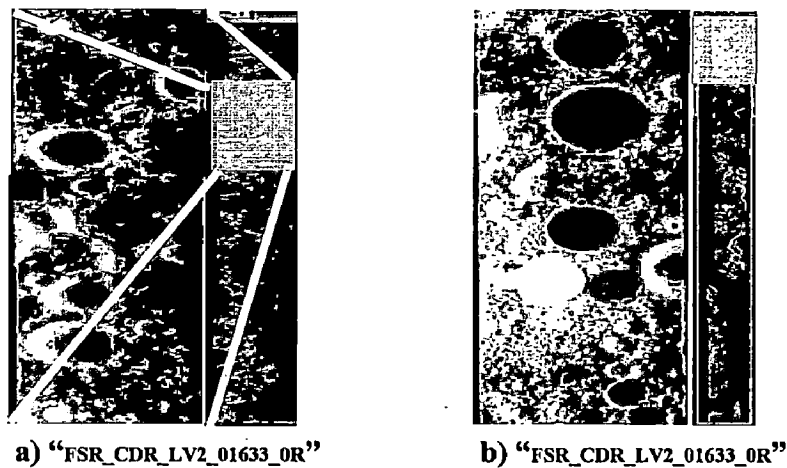
Figure: 4.5 Location of craters
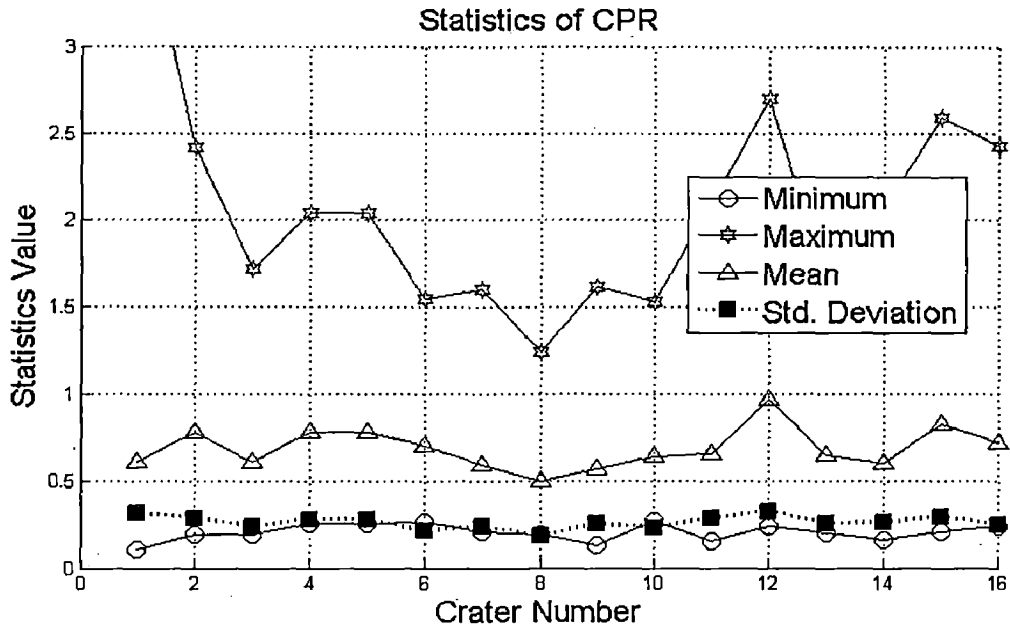
Statistics of CPR

Figure 4.6 Statistical graph of CPR data for 16 craters

Statistics of DoP(m)
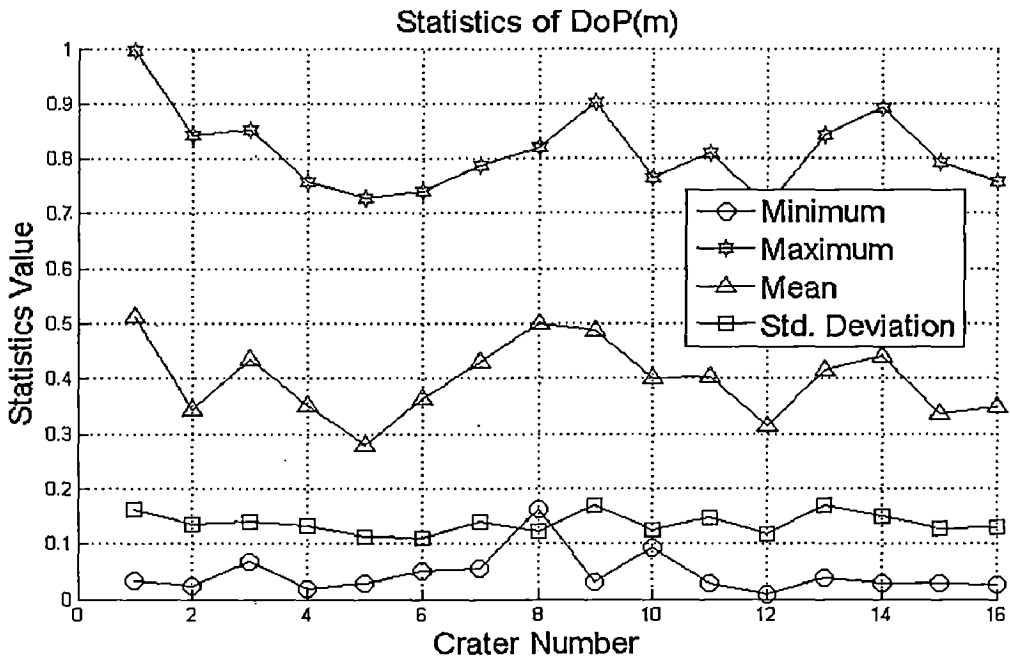
Figure 4.7 Statistical graph of degree of polarization (m) data for 16 craters
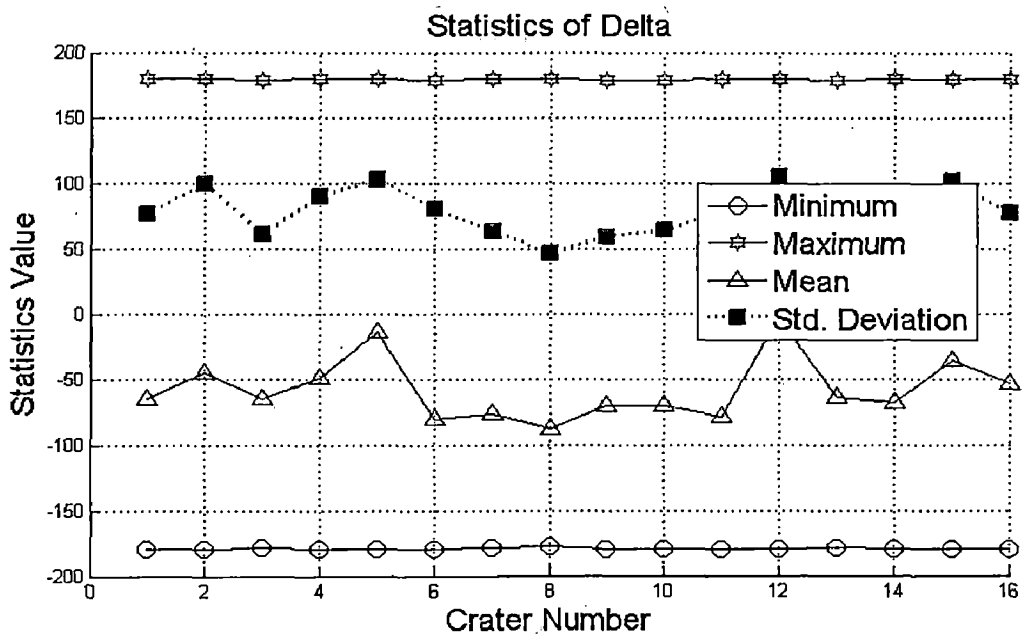
Figure: 4.8 Statistical graph of relative phase(δ) for 16 craters
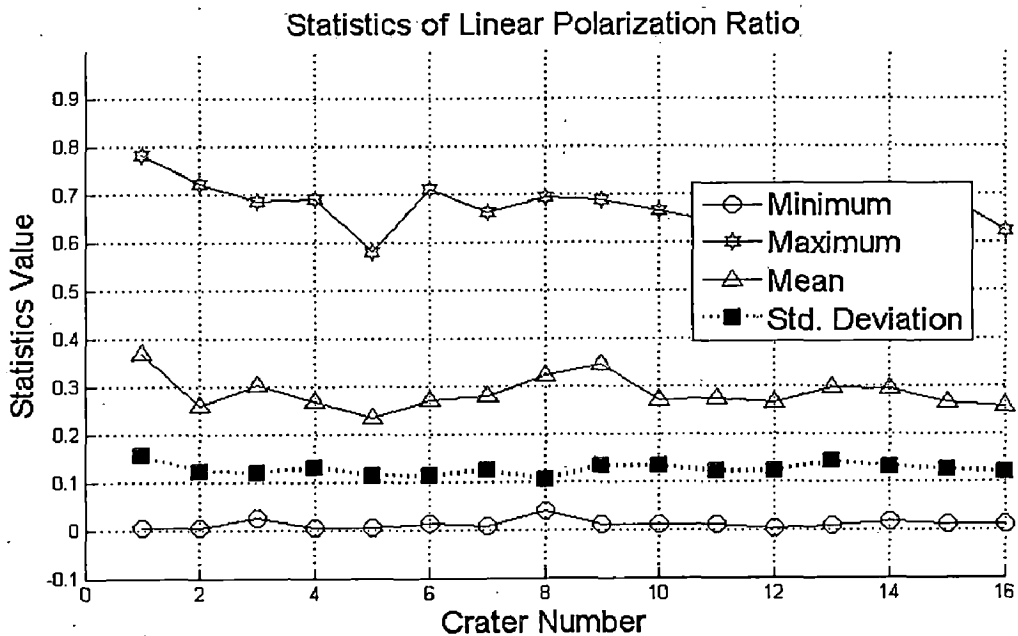
Figure: 4.9 Statistics graph of linear polarization ratio for 16 craters

44

Comparision of CPR & DoP(m)
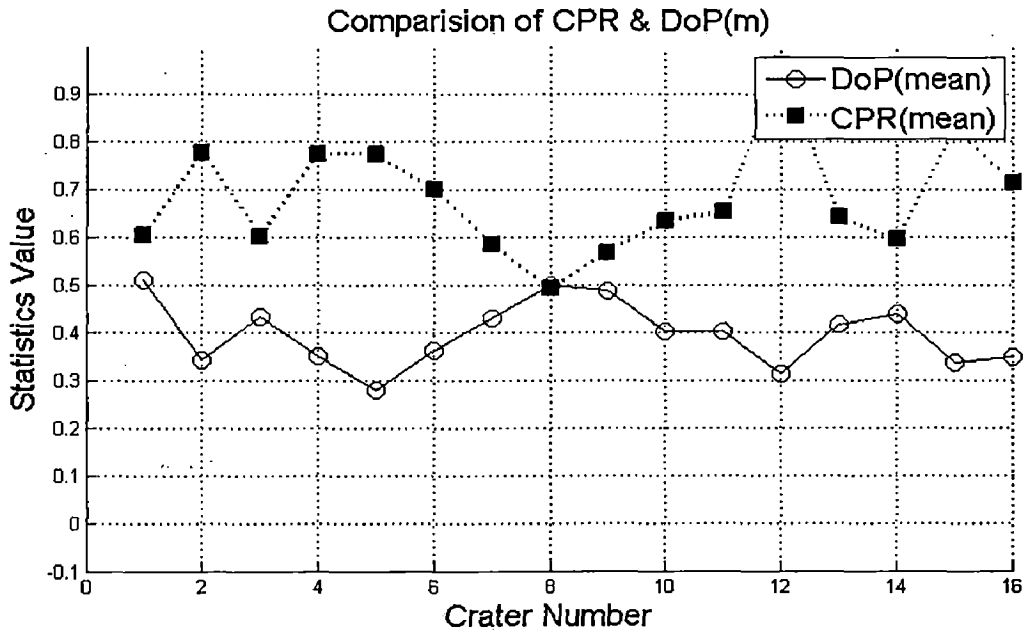
Figure: 4.10 Comparison graph for CPR and DoP inside each crater

From Fig. 4.10, we can conclude that in all cases higher value of CPR, DoP value decreases and vice-versa. CPR and DoP are closely related to surface property. For smooth surface low CPR and high DoP and vice-versa.

4.3 Implementation of 'm-δ' decomposition

4.3.1 Identification of type-I and type-II of craters

As discussed in section-3.4 in 'm-δ' decomposition, for a crater to satisfy 'm-δ' condition, it must have a distributed histogram for δ. In Fig.4.11 histogram of 'δ' for two ROIs are shown one for non-distributed and one for distributed 'δ'. By inspection of the bins of histogram it is determined whether the histogram is of distributed or non-distributed nature.
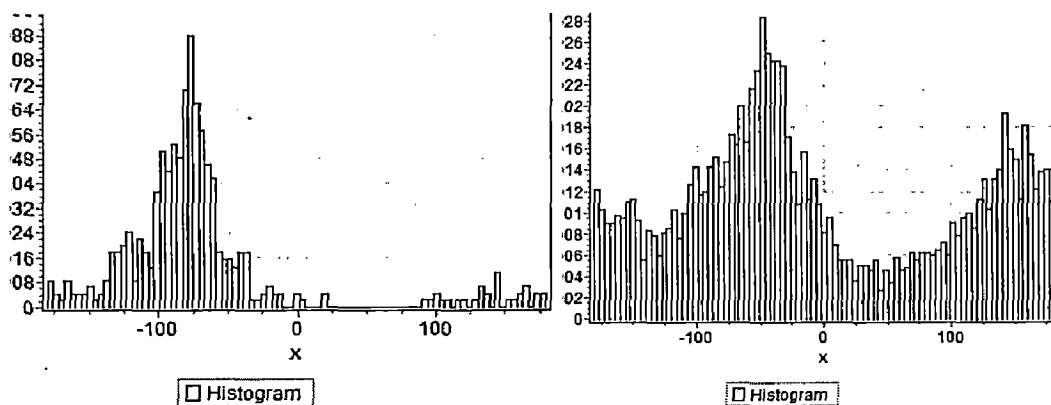
Figure: 4.11 Example of non-distributed and distributed ROIs for δ

45

Craters of scenes "FSR_CDR_LV2_01628_0R, FSR_CDR_LV2_01631_0R and FSR_CDR_LV2_01633_0R" are divided in two groups based on their CPR, degree of polarizations and δ value, the procedure is described in section-3.4. Here, implementation of the procedure is described for craters shown in Fig.4.5(a,b). Fig.4.12a shows pixels masked with CPR>1 and Fig.4.12b shows pixels masked with m<0.35 and in Fig.4.12c intersection of these masked pixels are shown. In Fig.4.12d some of the ROIs selected from different craters are shown. These ROIs have large number of pixels satisfying first two conditions simultaneously. Now histograms of δ are plotted for each of these ROIs (Fig.4.13, 1 to 16) and nature of distribution of δ is determined in each case by method of inspection. Based on these results each ROIs and hence crater to which those ROIs belong are differentiated and the result is presented in table-4.2.

Table-4.2

Result of 'm-δ' analysis for considered ROIs.

| ##ROI No.	% pixels m<0.35	Behaviour of 'δ'	'm-δ' condition satisfies	Type, probability of having planetary water-ice deposits
1.	24.98	Non Distributed	No	Type-II, Low ice probability
2.	56.30	Distributed	Yes	Type-I, High ice probability
3.	33.16	Non Distributed	No	Type-II, Low ice probability
4.	59.87	Distributed	Yes	Type-I, High ice probability
5.	69.26	Distributed	Yes	Type-I, High ice probability
6.	49.84	Non Distributed	No	Type-II, Low ice probability
7.	42.30	Non Distributed	No	Type-II, Low ice probability
8.	17.01	Non Distributed	No	Type-II, Low ice probability
9.	03.48	Non Distributed	No	Type-II, Low ice probability
10	36.24	Non Distributed	No	Type-II, Low ice probability
11	37.98	Non Distributed	No	Type-II, Low ice probability
12	63.17	Distributed	Yes	Type-I, High ice probability
13	37.80	Non Distributed	No	Type-II, Low ice probability
14	30.03	Non Distributed	No	Type-II, Low ice probability
15	57.28	Distributed	Yes	Type-I, High ice probability
16	53.72	Non Distributed	No	Type-II, Low ice probability
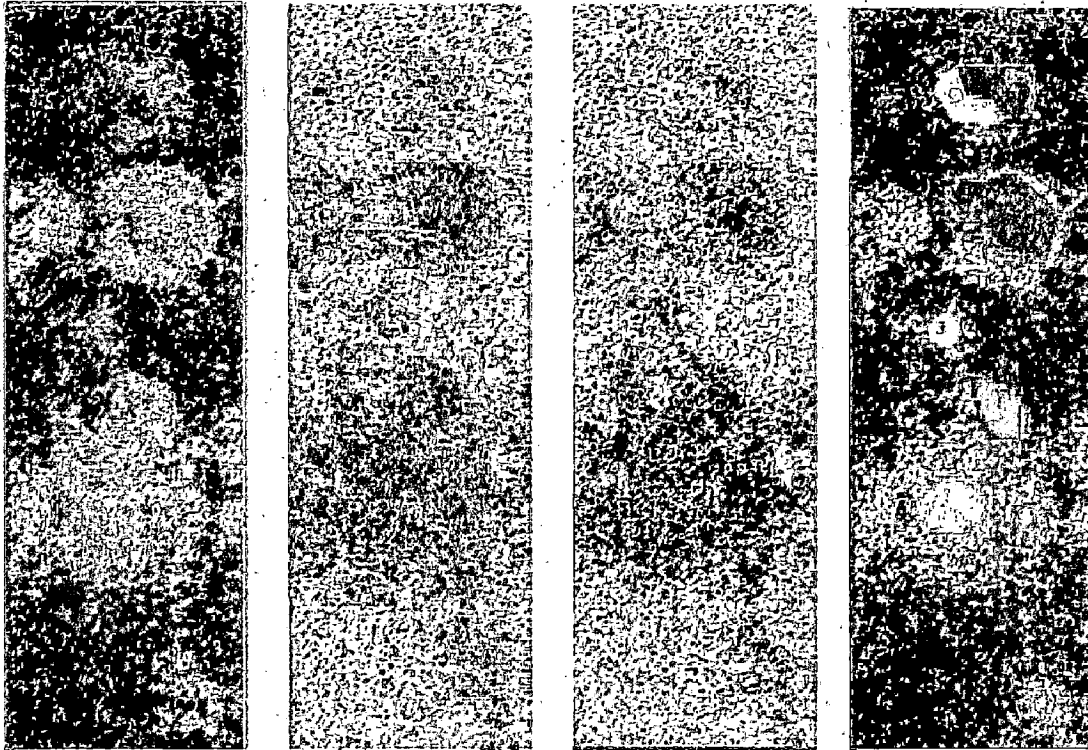
Figure: 4.12 Pixels having a) CPR>1 are masked by red colour, b) m<0.35 pixels are blue colour, c)CPR>1 & m<0.35 are masked by green colour. d) ROIs from different crater regions are shown.

Once we decide ROIs satisfying CPR>1 and m<0.35 condition we need to examine the distribution of δ for distributed or non-distributed property. Only nine craters from scene "FSR_CDR_LV2_01633_0R" are shown here rest of the craters are shown in Appendix-III

Histograms of all ROIs(1-16)

1. ROI#1, Non-distributed delta

2. ROI#2, Distributed delta

3. ROI#3, Non-distributed delta

4. ROI#4, Distributed delta
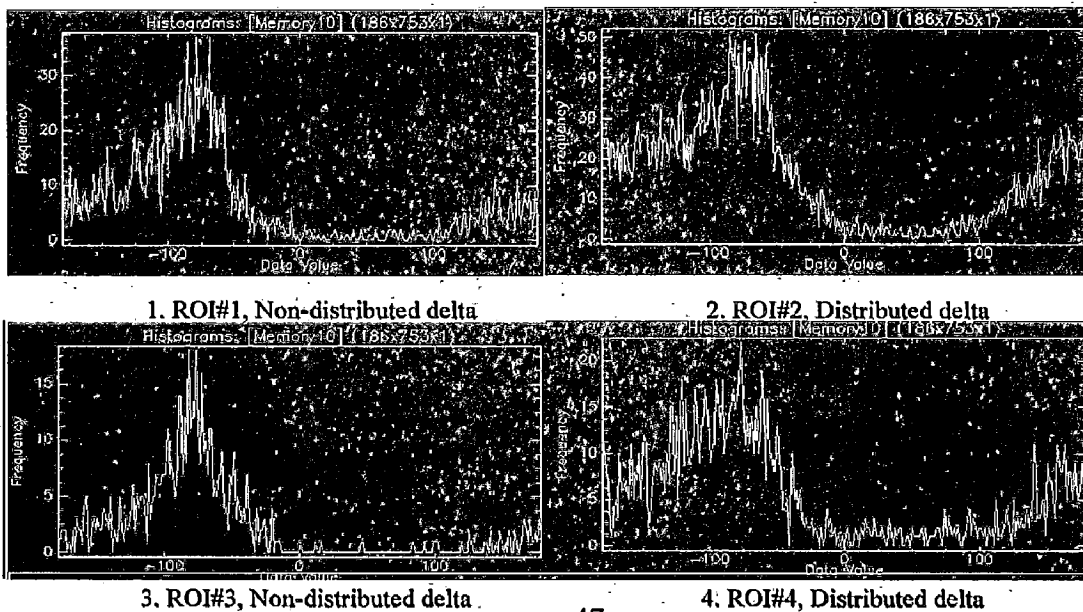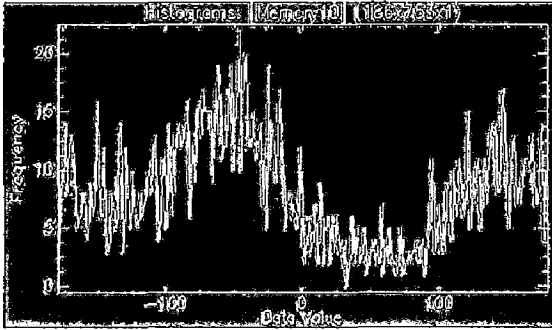
5. ROI#5, Distributed delta
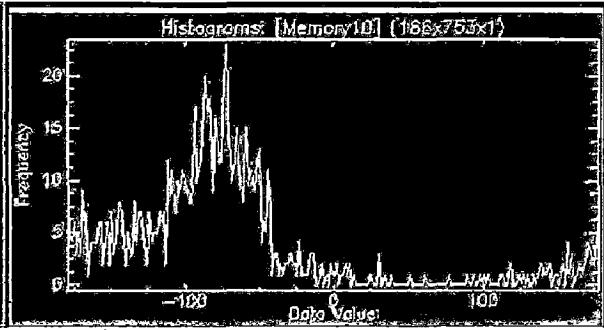
6. ROI#6, Non-distributed delta
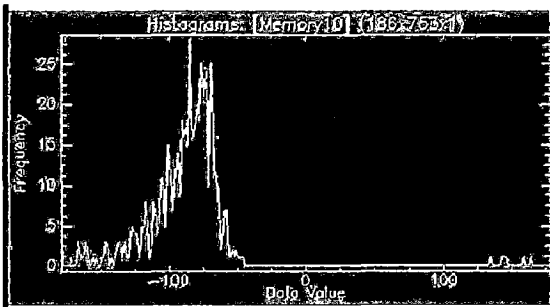
7. ROI#7, Non-distributed delta
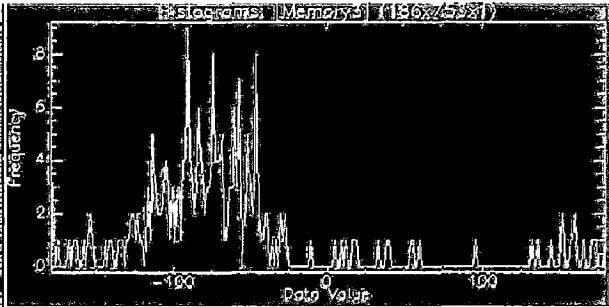
8. ROI#8, Non-distributed delta
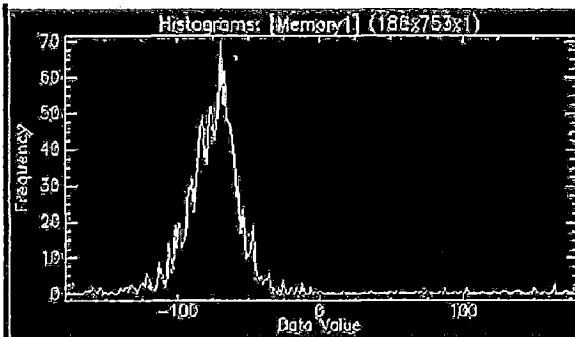
9.ROI#9, Non-distributed delta
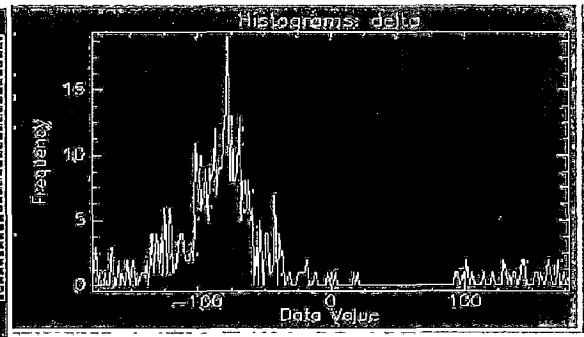
10.ROI#10, Non-distributed delta
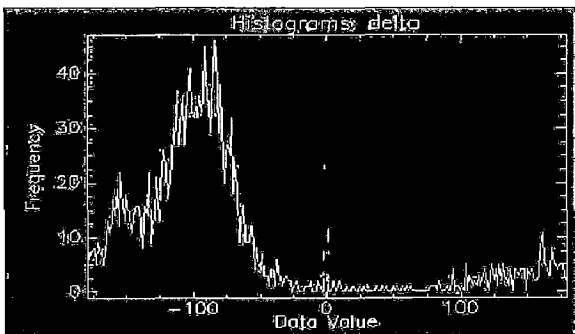
11.ROI#11, Non-distributed delta
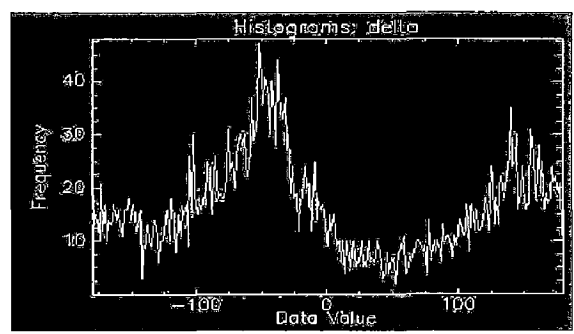
12.ROI#12, Distributed delta

48
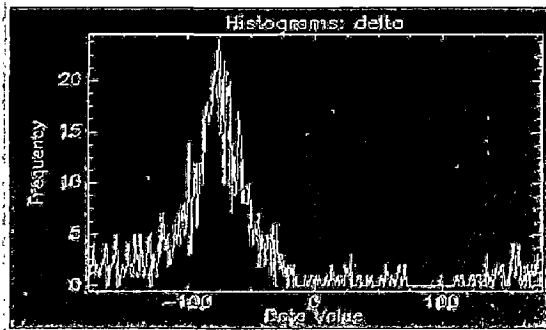
13.ROI#13, Non-distributed delta
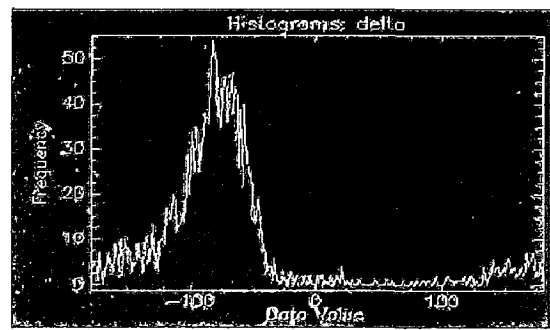
14.ROI#14, Distributed delta
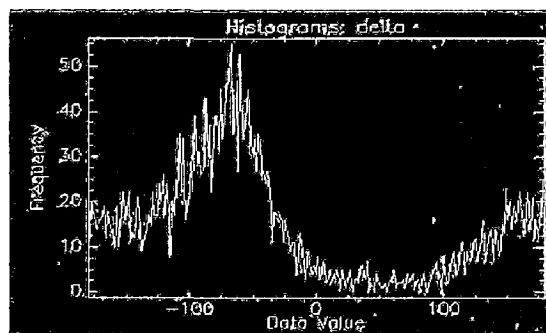
15.ROI#15, Distributed delta
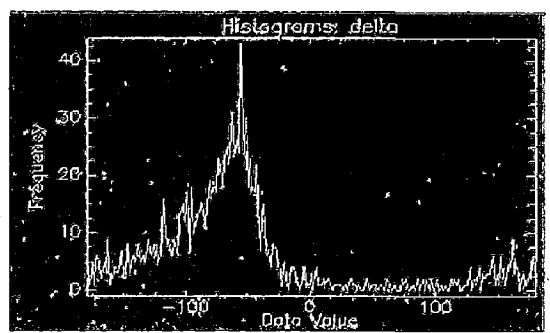
16.ROI#16, Distributed delta

Figure: 4.13, Histograms of δ for 16 ROIs (1-16)

In Fig. 4.13 histogram for relative phase (δ) is plotted to find out distribution nature of δ in each ROI. If an expanded histogram is observed we conclude that δ in this region is of distributed nature. If it is found that histogram is clustered around some particular value then distribution is of non-distributed nature. In above figure (Fig.4.13) histograms having serial number (1-9) are from scene "FSR_CDR_LV2_01628_0R, shown in Fig. 4.5(a) and serial number (10-16) are from scene FSR_CDR_ LV2_01633_0R"shown in Fig. 4.5(b).

4.3.2 RGB representation of scattering mechanism

In section-3.4 methodology to resolve three scattering mechanisms (Fig.2.3) is discussed. It calculates the fraction of power associated in three scattering mechanisms and each value is used as input for the primary colours to generate an RGB image of the area under investigation. Fig.4.14 shows an RGB image for the region shown in Fig.4.5(b).
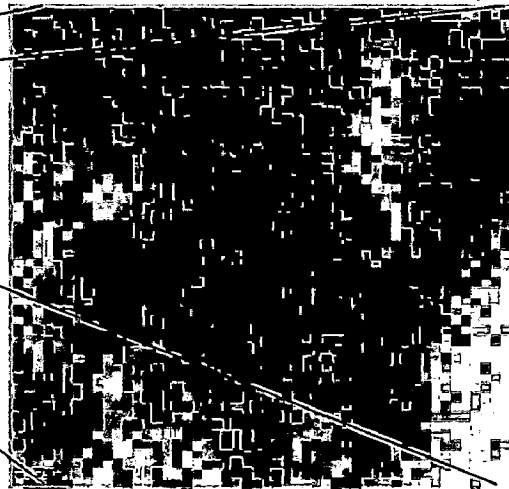
- Seeing the RGB image of m-δ decomposition it is clear that rim of craters has all types of scatterers but volume scatterers are dominant.
- Base of crater contains surface and volume scatterers.
- Other regions (magenta in colour) contain surface and double bounce scatterers.
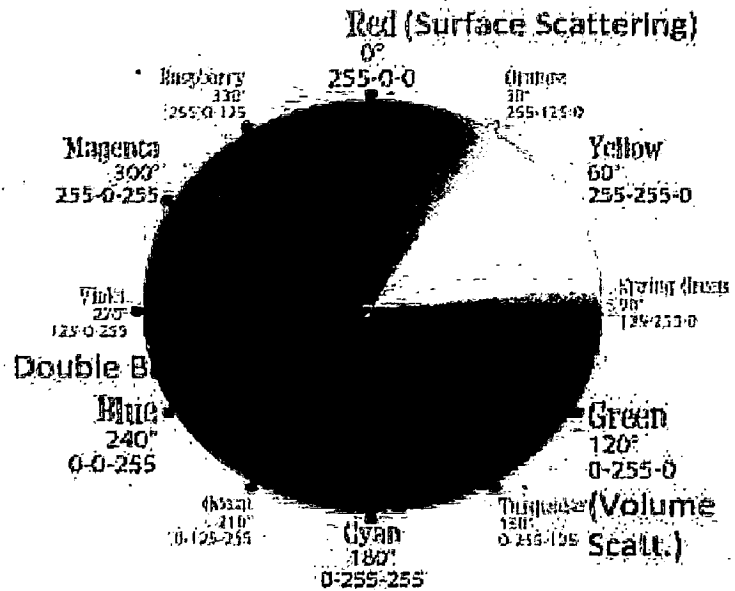
(a)   (b)

Figure: 4.14 a) RGB image of m-δ decomposition b) Colour composition of primary colours [54]

50

4.4. Implementation of statistical analysis

4.4.1 Implementation of GoF test to determine best fit PDF

Then GoF tests are applied on CPR value for different well known probability distribution functions (Beta, Kumarswamy, Johnson, Gen. Extreme Value, Log-Pearson, Weibull) on these ROIs. Since, 99.95% CPR pixels are in the range of 0-2 so GoF tests are applied only for bounded distribution. For every ROI Chi-square test parameter is calculated for each density function under test and based on the value of χ^2 these functions are ranked as shown in Fig.4.15 for simplicity only three functions are shown here. For each of the ROIs five best fitted distribution functions are selected according to Chi-square test parameter and number of occurrence of each density function is noted for each place as given in table-4.3. From this table it is concluded that distribution of CPR pixels is best represented by Generalized. Extreme Value distribution function [55]. Probability density function for Gen. Extreme Value is given in Eq. (4.1) and cumulative density function is given in Eq. (4.2).
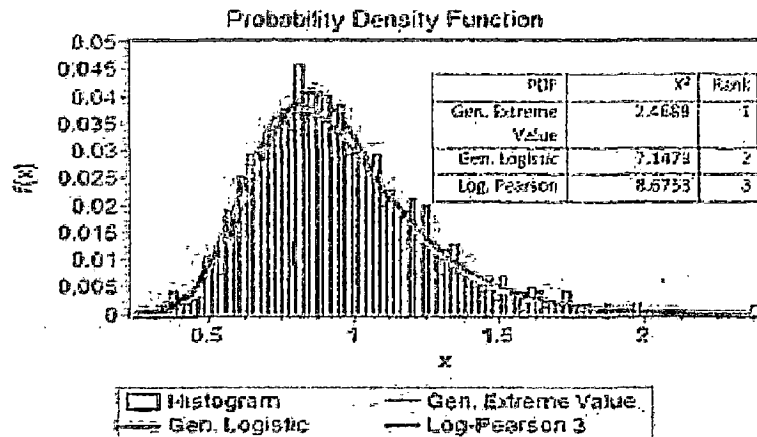
Figure: 4.15 Graph of different tested curves for a ROI

Table-4.3

Frequency of best fit density function

##	Base of crater					Rim of crater					Total				
Position	1st	2nd	3rd	4th	5th	1st	2nd	3rd	4th	5th	1st	2nd	3rd	4th	5th
Gen. Extreme Value	15	14	4	1	1	12	16	4	2	3	27	30	8	3	3
Beta	7	10	6	6	8	9	11	6	6	3	16	21	12	12	17
Kumaraswamy	8	6	4	10	4	9	6	4	11	2	17	12	8	21	8
Johnson	4	4	7	6	10	2	4	11	9	5	6	8	18	15	21
Log-Pearson	3	4	6	8	10	2	4	6	7	2	5	8	12	15	21
Gen. Logistic	4	1	8	6	8	4	2	9	6	3	8	3	17	12	17

4.4.2 Implementation of Pattern analysis

GoF tests are done on different homogeneous regions to determine the distribution function which can represent CPR pixels for crater regions effectively; it is found that Gen. Extreme value distribution function can effectively represent it. After that CPR data are modelled for ROIs of the crater regions which were identified as type-I and type-II craters in previous section now parameters for Gen. Extreme Value density function are estimated as described in section-3.3.2. Estimated value of these parameters are shown in table-4.4

Gen. Extreme Value probability density function is given below, x being the pixel value [55]:

$$f(x) = \frac{1}{\sigma} \exp\left(-(1+kz)^{-\frac{1}{k}}\right)(1+kz)^{-1-1/k} \qquad (4.1)$$

Cumulative density function for Gen. Extreme Value PDF

$$F(x) = \exp\left(-(1+kz)^{-\frac{1}{k}}\right) \qquad (4.2)$$

Where,

k =continuous shape parameter

σ=continuous scale parameter ($\sigma > 0$)

μ- continuous location parameter

$$z \equiv \frac{x-\mu}{\sigma}$$

For $k \neq 0$, its domain is given by (4.3)

$$1 + k\frac{(x-\mu)}{\sigma} > 0 \qquad (4.3)$$

Once we have estimated value of 'k, σ and μ' for both types of craters, range of these parameters can be calculated by method described in section-3.3.2 for each type of craters.

Graph of best fitted Gen. Extrem Value function for Type-II
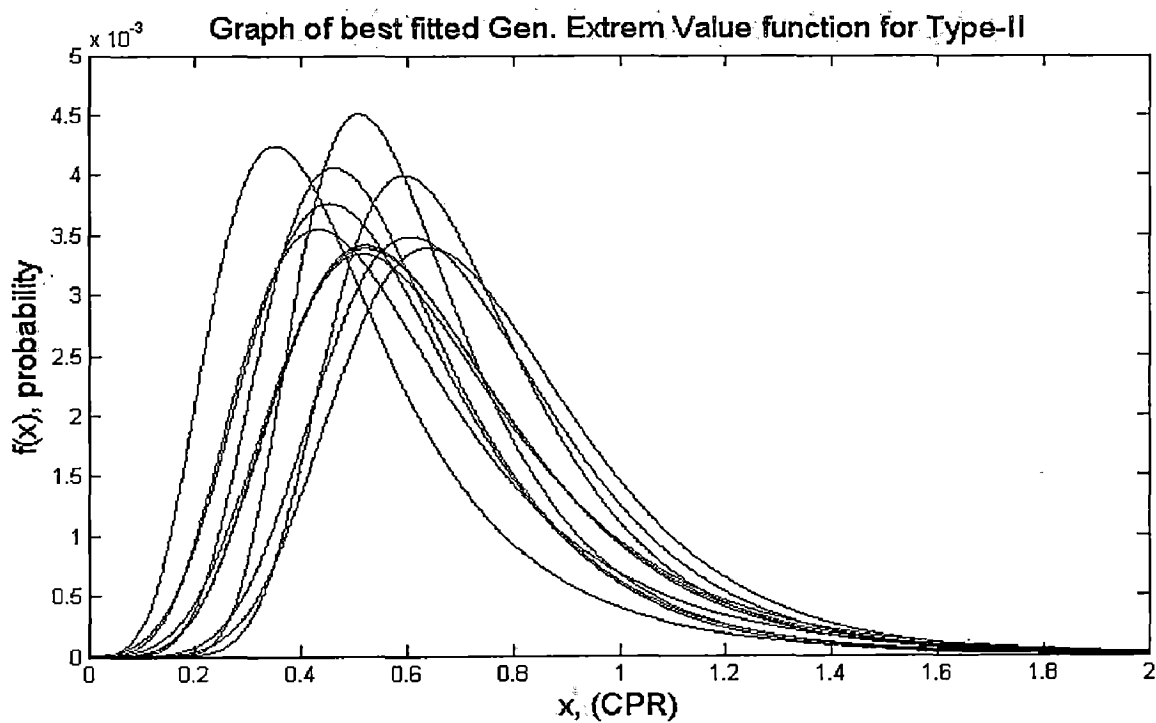
Figure: 4.16 Graphs of best fitted density function for type-II craters

Graph of best fitted Gen. Extrem Value function for Type-I
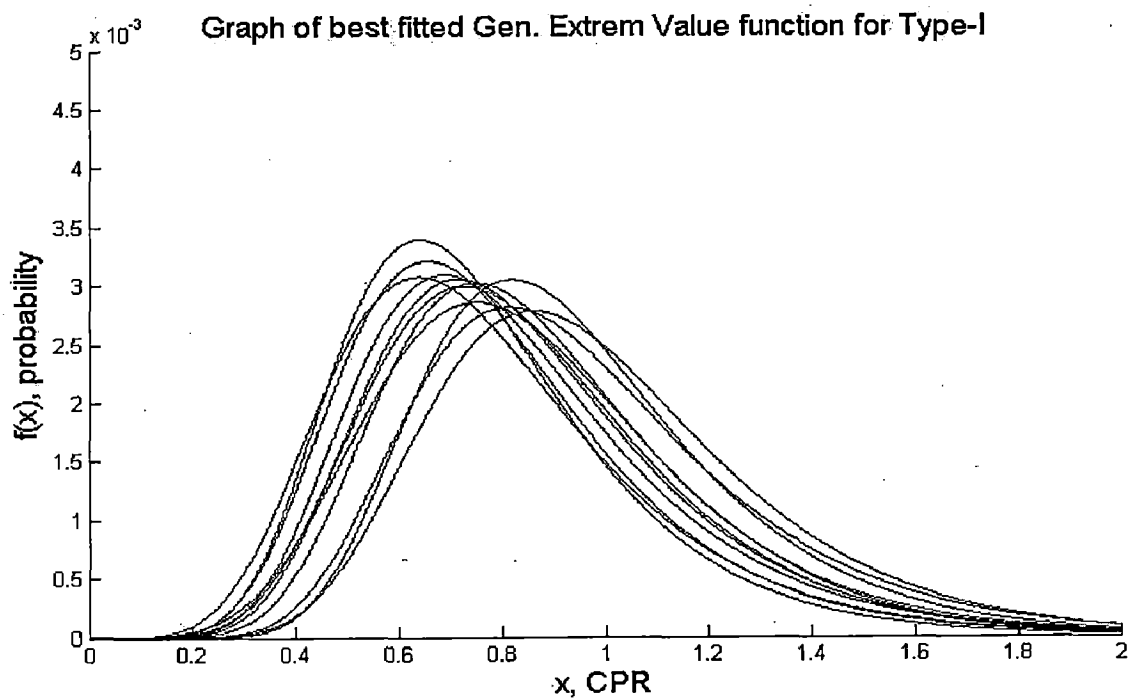
Figure: 4.17 Graphs of best fitted density function for type-I craters

Table-4.4

Estimated parameters for Gen. Extreme value density function

Type-1Craters. Higher probability of Planetary Ice			Type-2 Craters. Lower probability of Planetary Ice		
K	σ	μ	K	σ	μ
0.01343	0.26144	0.8166	0.09155	0.16387	0.52326
0.02048	0.23797	0.69271	0.01373	0.21721	0.52523
.00013238	0.22931	0.6559	0.08249	0.22096	0.53308
0.00193	0.23938	0.63902	0.07983	0.1817	0.47591
0.00417	0.24073	0.71551	0.04114	0.18426	0.6019
-.005794	0.2414	0.81681	0.12559	0.20893	0.45652
-0.03223	0.24582	0.7181	0.14201	0.17503	0.37379
-0.02218	0.26475	0.85286	0.05104	0.21583	0.53171
-0.07034	0.25819	0.73115	0.00984	0.19553	0.45527
-0.00452	0.217	0.63984	-0.0074	0.21091	0.60555
-0.00321	0.24357	0.74718	-0.0045	0.217	0.63984
			0.03648	0.21341	0.62826
			0.02291	0.14809	0.44907

Table-4.5

Obtained boundaries for range of position and scale parameter

##	σ				μ			
	Mean(m)	Std. Dev (SD)	m-SD	m+SD	Mean(m)	Std. Dev (SD)	m-SD	m+SD
Type-I	0.2436	0.0140	0.2296	0.2576	0.7296	0.0735	0.6561	0.8031
Type-II	0.1964	0.0236	0.1728	0.2200	0.523	0.0801	0.4429	0.6031

So, if the estimated value of 'σ' remains in the range of (0.2296 to 0.2576) and that of 'μ' remains in the range of (0.6561 to 0.8031) for CPR data in any ROI or crater then that ROI or crater can be labelled as type-I and if the estimated value of 'σ' remains in the range of

(0.1728 to 0.2200) and that of 'μ' remains in the range of (0.4429 to 0.6031) for CPR data in any ROI or crater then that ROI or crater can be labelled as type-II. If 'μ' and 'σ' does not lie
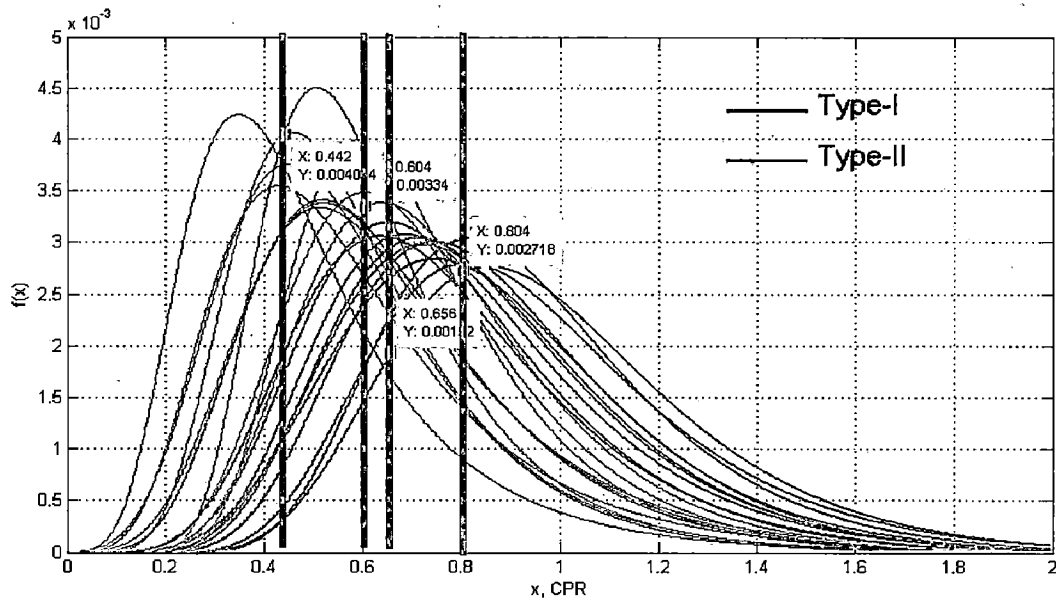
Figure: 4.18 Graph of best fitted density function for craters. Red bars are range of position parameter of type-II craters and blue bars are for type-I craters

in any range then we cannot label the ROI as type-I or type-II conclusively. Significance of the range of position parameter 'μ' for two crater types is explained in Fig.4.18. Position parameters gives the location of the peak of the curve, hence blue bars are boundaries for peak of type-I craters and red bars are boundaries for type-II craters. It is observed that with the pattern analysis, it is possible to segregate the two types of craters, which represents that both type of craters have different pattern and it may be due to many reasons

4.5. Implementation of textural analysis

Classification of lunar surface into five different unknown categories using textural approach has been carried out as explained by the flow chart in Fig.4.19. The fractal map and Moran's*I* map of the image are generated by estimating the local fractal dimension inside a chosen moving window. Fractal dimension and Moran's*I* values are plotted as image pixels according to the methods discussed in section-3.6. These textured images are generated applying moving window approach for different window sizes. Fractal map and Moran'sI map for different windows for part of a scene as identified by 'FSR_CDR_LV2_01633_0R' are shown in Fig.4.19 and in Fig.4.20. Fig.4.19a is total intensity map whose fractal and Moran'sI map are shown in these images. In fractal map as well in Moran's*I* map (Fig 4.19

and 4.20) we can clearly see the wall rings of craters though these rings are clearer in Moran'sI map. As Moran'sI gives spatial autocorrelation so seeing these maps only we can conclude that craters rings at different heights have different textural properties.

Fractal maps for local window sizes 5×5 and 9×9
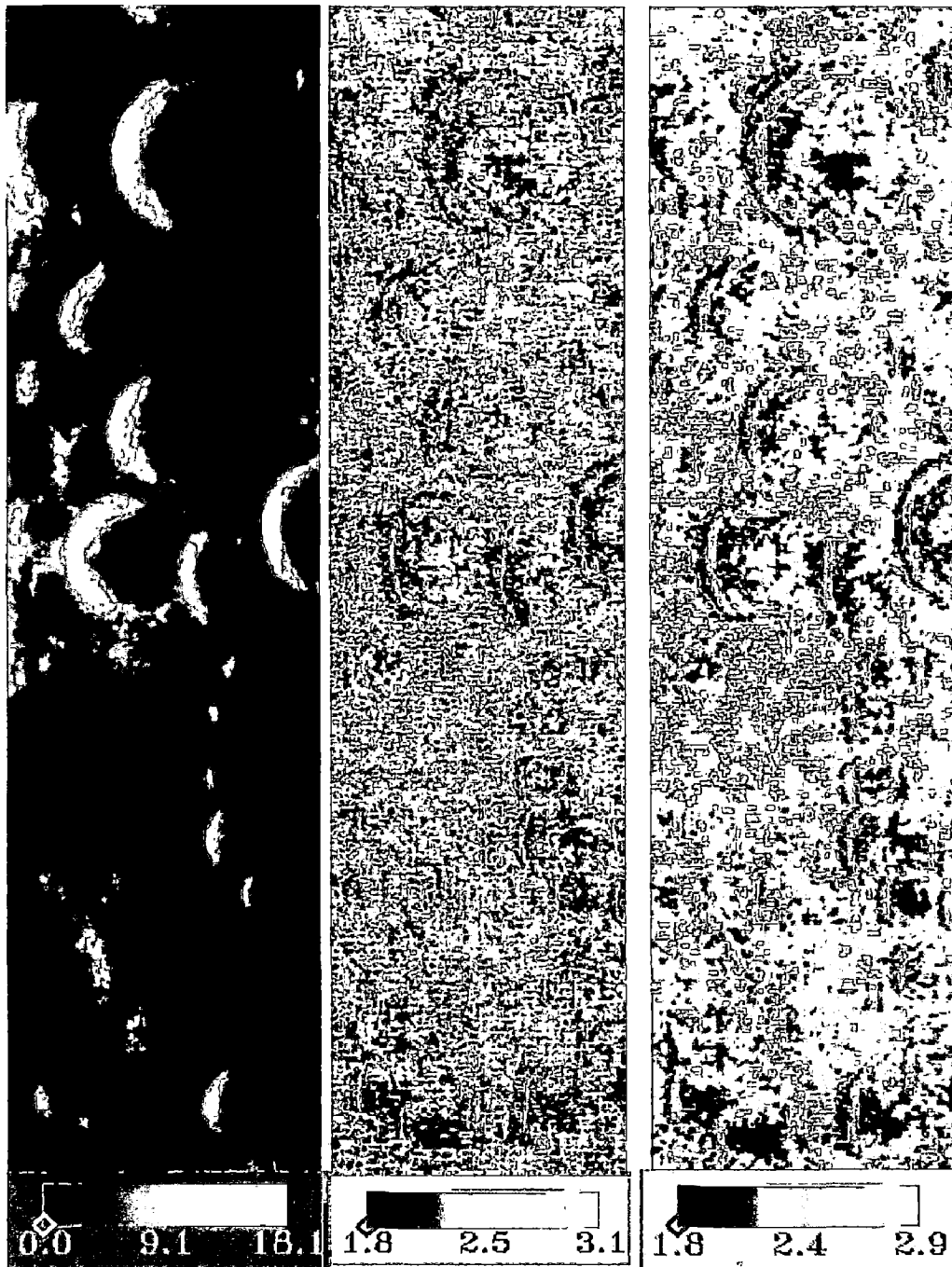
Figure: 4.19 a) Total power image b) Fractal image for window size 5x5 c) Fractal image for window size 9x9
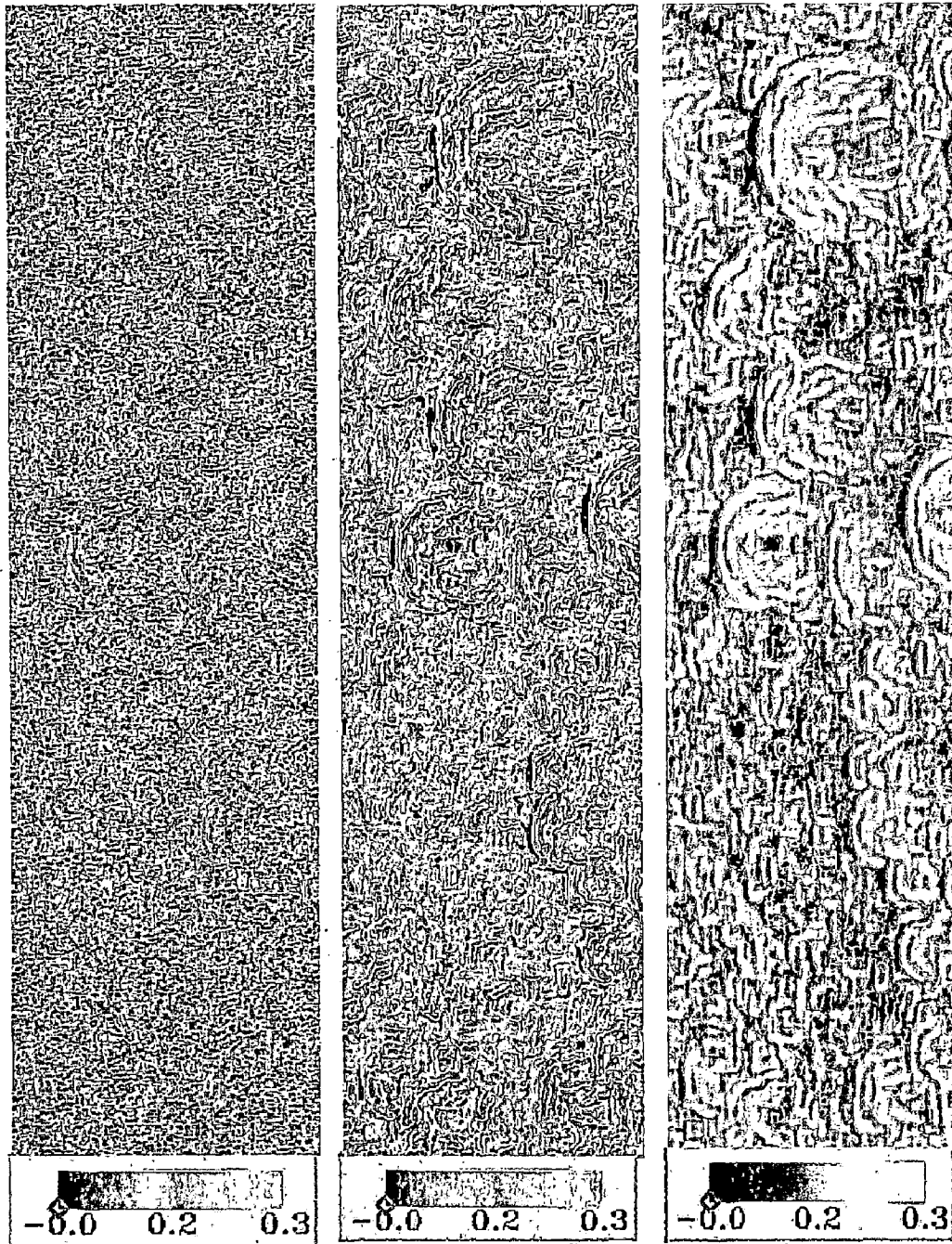
Figure: 4.20 a) Moran'sI map(5x5)   b) 'I' map image for window size 7x7 c) 'I' map for window size 9x9 (B/W)

4.5.1 Implementation of classification algorithm

K-means unsupervised classification technique is used for classification of texture images. After classification image pixels are clustered in five different classes based on their D, I and SAR properties. Classified images of same scene are shown in below for different window sizes. Fractal and Moran's I images are added accordingly to generate D+S, D+I+S, I+S maps. For compatibility all images were resized to same dimension. These images are then classified using K-mean classifier according to the algorithm as discussed in section-3.6.2.

D+S Classified images

Fig.4.21 (a, b) are classified images of D+S map for window sizes 5x5 and 9x9 the same part which is shown in Fig.4.19a from scene "FSR_CDR_LV2_01633_0R" Classification of D+S image does the clustering of the pixels of base regions and of external rim regions of craters very effectively as well as it performs clustering of highly illuminated rim regions. In Fig.4.21c classified image based on only D value is shown, this image is very different when compared to classified image of D+S and original intensity image. It identifies start boundary of craters very effectively which is obvious as large discontinuities at the edges exist, though back edge is not identified clearly but for back edge still an unclear boundary between base region and outside of crater exist, this unclear boundary is better visible in D+S classified images. Table-4.6 shows pixel statistics of different classes for D+S images. In class five maximum, mean and standard deviation value of D+S have abnormally higher value this anomaly is because 'S' image has few pixels which has abnormally higher values, this is true for every classification result. Classification results for local window size 9x9 have larger clusters compared to window size 5x5

Table-4.6
Pixel statistics of different classes for D+S classification

Class#	Range		Mean	Std Deviation
	Max	Min		
1.	2.0581	1.8144	2.018468	0.038883
2.	2.2588	2.0582	2.189802	0.047846
3.	2.4595	2.2589	2.343017	0.054656
4.	2.6601	2.4596	2.533057	0.053723
5.	20.565	2.6602	3.368587	1.445817

Classified maps of D+S maps for local windows 5×5, 9×9, Fig.4.21c is for only D map

(a)	(b)	(c)

Figure: 4.21 Classified Image for D+S map for local window sizes (a) for window size 5x5, (b) for window size 9x9 and (c) for only D map 9x9 window size

Fig.4.22 (a, b) gives the classified images of same scene which is used earlier based on I+S values. Fig.4.22c is classified image of the same region based on only 'I' value. Classification of I+S images gives bigger cluster sizes when compared to cluster size of D+S classified images. 'I' value doesn't vary much if terrain properties changes gradually but sharp discontinuities are detected readily if its size is comparable to window size. In regions having high discontinuity 'I' value remains very less, so K-mean classifier may classify these pixels together in same class, so classification based on only 'I' values is not much reliable [36]. Seeing Fig.4.22c it can be concluded that regions just outside of crater has very less spatial correlation so we can say these regions are very rough in nature. Rims of craters have high spatial correlation so it can be decided that rims either do not change properties or change in gradually and sharp changes are not observed. However in some craters base region contains high discontinuities. Overall accuracy beside few specific terrain properties classification based on 'I' value is not of much information. The classification results based on combination of 'I' values with image pixels, however, is better than 'I' alone.

Table-4.7

Pixel statistics of different classes for I+S classification

Class#	Range		Mean	Std Deviation
	Max	Min		
1.	0.0382	0.0283	0.033925	0.004594
2.	2.2588	2.0582	2.189802	0.047846
3.	0.427	0.2332	0.305022	0.049363
4.	0.6209	0.4271	0.497166	0.052935
5.	18.301	0.6209	1.395977	1.470826

Classified maps of I+S maps for window sizes 5×5, 9×9, Fig.4.22c is classified map
for only Moran'sI value and fr window size 9×9

Class 1
Class 2
Class 3
Class 4
Class 5

Unclass
Class 1
Class 2
Class 3
Class 4
Class 5

Figure: 4.22 Classified Image for I+S map for local window sizes (a) for window size 5x5, (b) for window size 9x9 and (c) for only I map, 9x9 window size

D+I+S Classified maps

Fig.4.23 gives the classified images of the same scene which is used earlier for D+I+S map. Classification of D+I+S images gives smaller cluster sizes compared to cluster sizes in D+S as well as in I+S classified images. This classification is based on all three properties which are discussed here fractal, spatial autocorrelation and image pixel value. Classified D+I+S image identify the outer border, rim and rough regions inside the crater bases too. Due to unavailability of terrain type of lunar surface analysis of classified images is very limited. Fig. 4.23c is classified image based on only 'I' value.

Table-4.8

Pixel statistics of different classes for D+I+S classification

Class#	Range		Mean	Std Deviation
	Max	Min		
1.	2.2125	1.8704	2.153412	0.057551
2.	2.4166	2.2126	2.342707	0.05109
3.	2.6206	2.4167	2.503575	0.055739
4.	2.8246	2.6207	2.696398	0.055186
5.	20.725	2.8247	3.516717	1.415746

Classified maps of D+I+S maps for window sizes 5×5, 9×9, Fig.4.23c is classified map for only Moran'sI value and for window size 9×9
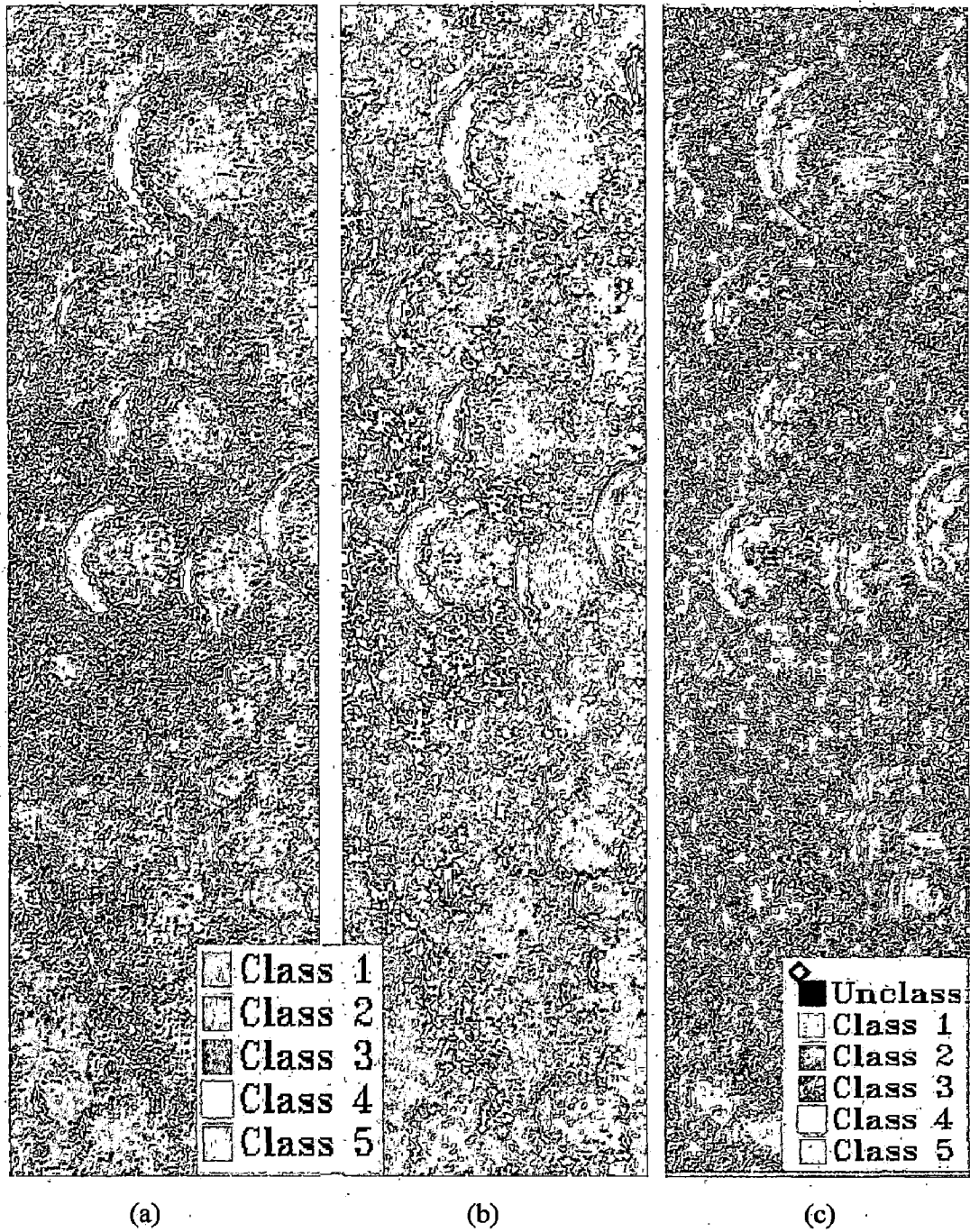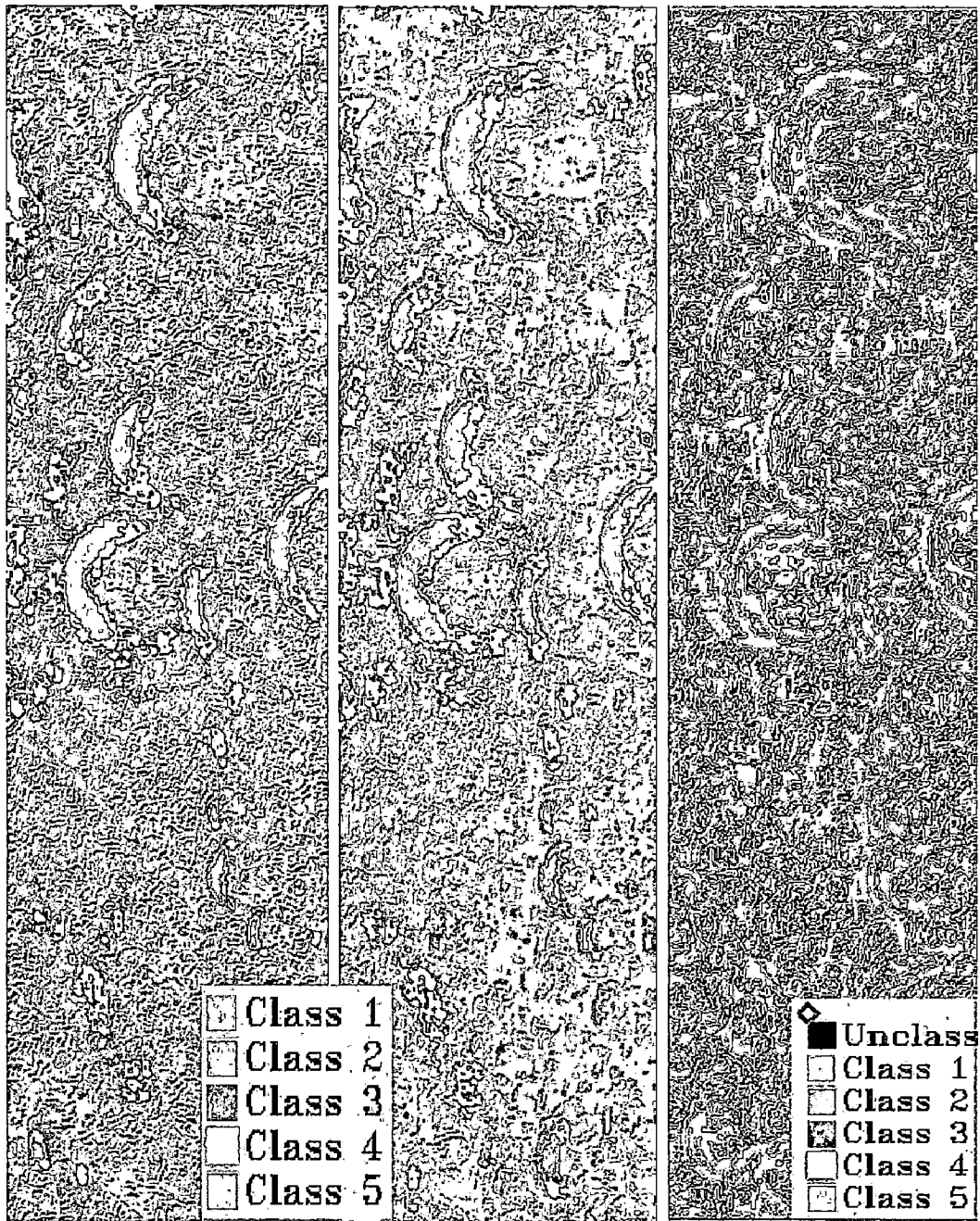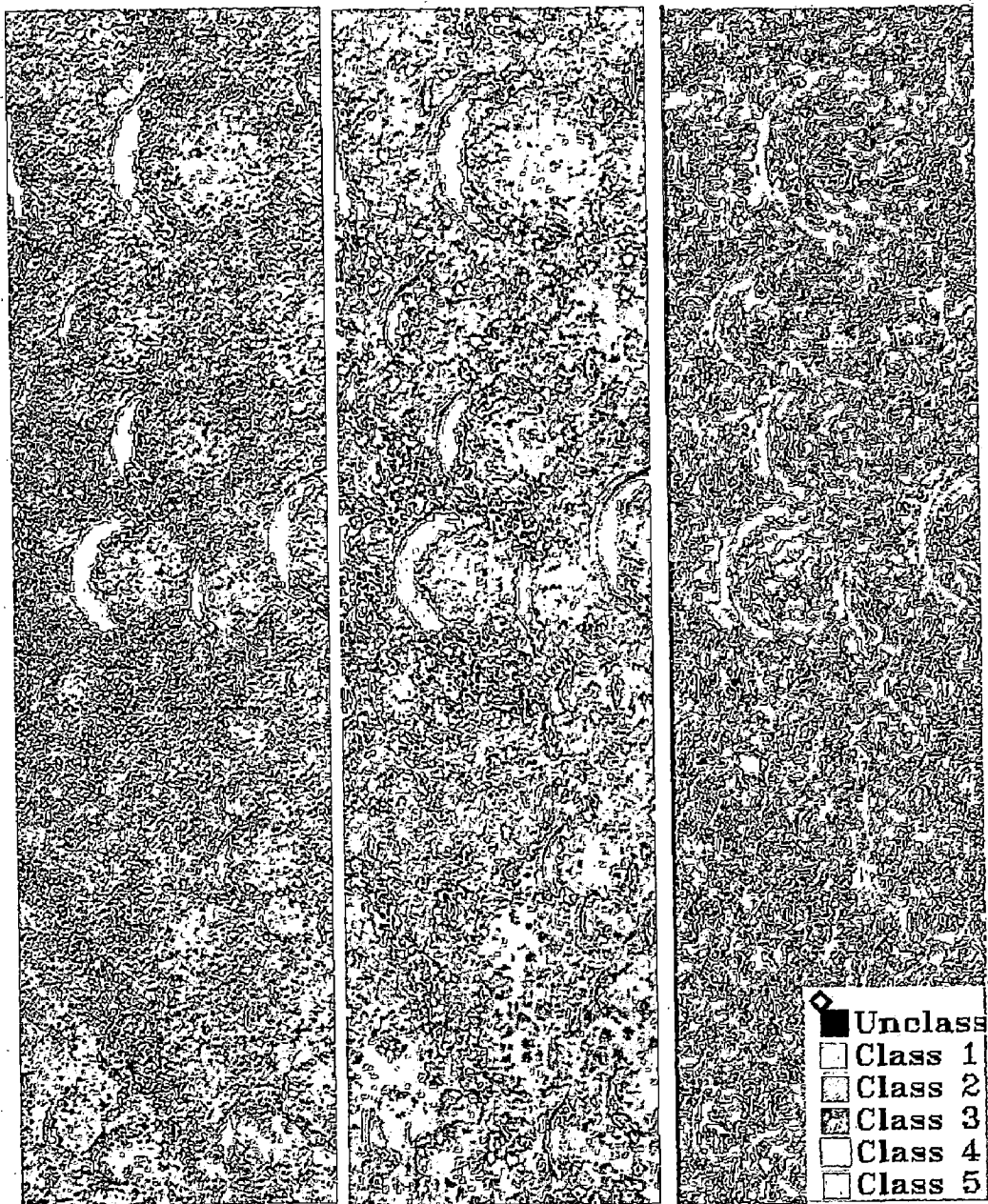

Figure: 4.23 Classified Image of D+I+S map for local window sizes (a) for window size 5x5, (b) for window size 9x9 and (c) for only I map, 9x9 window size

Justification for 5 classes

The prime reason behind selecting only five classes for the classification of textural images is three scattering phenomenon. One class for each regions having dominant volume scatterers, dominant double bounce and dominant surface scatterers. Beside this one class is reserved for rim of the craters as rims have very high illumination from mini-SAR sensor and one class I for error pixels which have abnormally high intensity in the range of (1 to 25) as discussed in section-4.1. Since ground truth data is not available so it is very tough to judge the accuracy and also labelling of classes cannot be done intuitively, location of crater boundaries and rims are known approximately from total intensity image it was observed that some classes overlapped to these regions hence the type of these regions concluded.

4.5.2 Effect of Window Size on Classification

Since window size is one of the major factors explaining various kinds of textures, it is important to critically analyze the windowing effect for textural analysis of mini-SAR data. For window selection various sizes are considered starting from 5×5 and increasing it by steps of 2 to obtain the odd size window. For getting different type of texture information, we have varied the window size up to 15×15. The size of local window is considered to be odd because it contains a centre pixel, which acts as the representative of the whole local neighbourhood. The smallest size selected is to be 5×5 because it provides minimum 4 points for least square slope estimation in 'D' calculation, which would be only 2 points if 3×3 window were used, while the maximum size of local window is chosen to be 15×15 because beyond this size the blurring effect in the processed texture image highly increases and hence do not provide much information. The process is done for both methods, i.e., TPSAM and DBC. For getting the variation of 'D' values in local neighbourhood, the maximum and minimum values of 'D' for both methods are compared. In parallel, for each local window, the value of Moran'sI is computed and finally the I-map is generated. This was the second texture map for the study. The maximum and minimum values of 'I' along with mean and standard deviation for each local window size are estimated as shown in table-4.9. The minimum values of 'D' are less than 2.0 in both the methods, i.e., TPSAM and DBC, which are due to the fact that natural scenes are not exact fractals nevertheless they are modelled with fractals and they are statistically self-similar rather than exactly self-similar. The maximum value of D for both methods shows a variation such that in DBC with increase in local window size maximum value of D decreases, while in TPSAM maximum value of D increases first and then decreases as far as the local window size is increased, which is

64

obvious, since for increasing size of images smaller irregularities get hidden. Another important notable point in DBC is that the difference between maximum and minimum values becomes lesser as the window size increases while the minimum value of D for TPSAM is almost same. The standard deviation (SD) gives the deflection from the mean and the values of SD show that the data is compact about the mean D.

Table-4.9

The Values of 'D' and 'I' for different window size

W		5	7	9	11	13	15
D (TPSAM)	Max	3.1288	2.9107	2.9543	2.8471	2.7830	2.7384
	Min	1.7468	1.7803	1.8145	1.8031	1.8343	1.8104
	Mean	2.1639	2.1888	2.2294	2.2530	2.2293	2.1935
	SD	0.1283	0.1265	0.0994	0.0859	0.0797	0.0787
D (DBC)	Max	2.9802	2.883	2.8626	2.8247	2.7953	2.7595
	Min	0.5742	1.2369	1.5429	1.6143	1.7046	1.7464
	Mean	2.3334	2.3427	2.3618	2.2845	2.3283	2.3278
	SD	0.2831	0.1893	0.1675	0.1385	0.1582	0.1382
Moran'sI	Max	0.2395	0.2950	0.3207	0.3295	0.3350	0.3373
	Min	−0.0577	−0.0165	−0.0118	-0.0141	-0.0061	0.0042
	Mean	0.1363	0.1484	0.1593	0.1688	0.1760	0.1812
	SD	0.052	0.0552	0.0550	0.0544	0.0545	0.0547

Concluding from the table-4.9, The TPSAM values of 'D' are suitable to be used for the classification study. Further, the values of 'I' represented in table-4.9 show that as the window size increases, the minimum values go into positive range which are negative for

lower window sizes. It shows that with increase in local window, the association of neighbouring pixels increases. So, for identifying irregularities or similarity in a region ·Moran'sI map alone is much suited. It is also observed from the results that the values of 'D' increase with random variation in pixel values, which is opposite to that of 'I' as it decreases with randomness in pixel values. This shows an inverse relation in 'D' and 'I' [56]. This inverse relation is also clear from table-4.9, where the mean values of 'D' and 'I' show an opposite behaviour, i.e., with increase in local window size the mean value of D (both TPSAM and DBC) increases while the mean value of 'I' decreases. Finally, it infers that ·TPSAM performance better than DBC because the variation in the values of DBC is more than that of TPSAM. It is again clear from the values of SD for both methods that the SD for TPSAM is more stable than that of DBC.

Fig.4.19 shows the D-map for window size 5x5 and 9x9. As emphasized, the 'D' values are susceptible to sharp changes; the D-maps can identify the linear features as well as the lumped portions in images. The front side of rim got identified as these pixels had very high value in original power image too though base regions didn't had such advantage. For increasing local window size, the texture image (D-map) goes to be blurred and the size of the D-map decreases due to border effect. For various window sizes, the texture and hence the identified land features get changed. It is observed in D-maps that for lower window size, e.g., 5, 9, the linear features (e.g. rim of craters) are sharply identifiable whereas for increased local window size, these features get blurred. For lower window size these features are clearly visible, while for higher window size the blurring effect again takes place making the features mixed with other features. The D-map is combined with the image for testing the combined effect of 'D' and pixel values. For this purpose, the D-map and image sizes are made same and the 'D' values are scaled in the range of image pixel values. For various local window sizes and hence 'D' maps the original image is resized. The effect of Moran'sI is ·studied in a similar way to that of 'D'. At first the I-map alone is tested for feature identification and then the combination of 'I' with pixel values is tested. I-map is sensitive to smooth areas, which is opposite to that of 'D' values and provides very fine textured images as shown in Fig.4.20. With the I-map the sharp changes in image pixel intensities are not easy to identify, however if the sharp change is extended up to window size then these can be identified.

4.5.3. Comparison of texture parameters for different craters

In Fig.4.24 comparison graph for fractal dimension is shown. Standard deviation of the fractal dimension is very low which indicates that fractal dimension is not varying much with the movement of local window over intensity map. Further mean of fractal dimension has lower value indication the radar backscatter intensity is not varying much in a local window but it may have large deviation when compared pixel by pixel basis but it has random distribution in a local window as indicated by statistics of Moran'sI.

In Fig.4.25 comparison graph for Moran'sI is shown. Minimum value of the Moran'sI ranges in (0 to 0.05) indicating a random behaviour of pixels i.e. high irregularities in those local windows. Maximum value of Moran'sI is limited around 0.32 which shows that on lunar surface large smooth regions do not exist where pixels are closely related. Thus we conclude that on average lunar surface is highly irregular in nature.

In Fig.4.26 statistics of total intensity is shown. The graph for maximum value of intensity is not shown because it has abnormally large value due to occasional occurrence of error pixels in intensity image. These error pixels can be assume as a result of random errors present in mini-SAR sensors. As we can see standard deviation value is comparable to mean and maximum pixel intensity value, thus we can say that radar backscatter is very sensitive and it changes rapidly also indicating rough behaviour of surface.
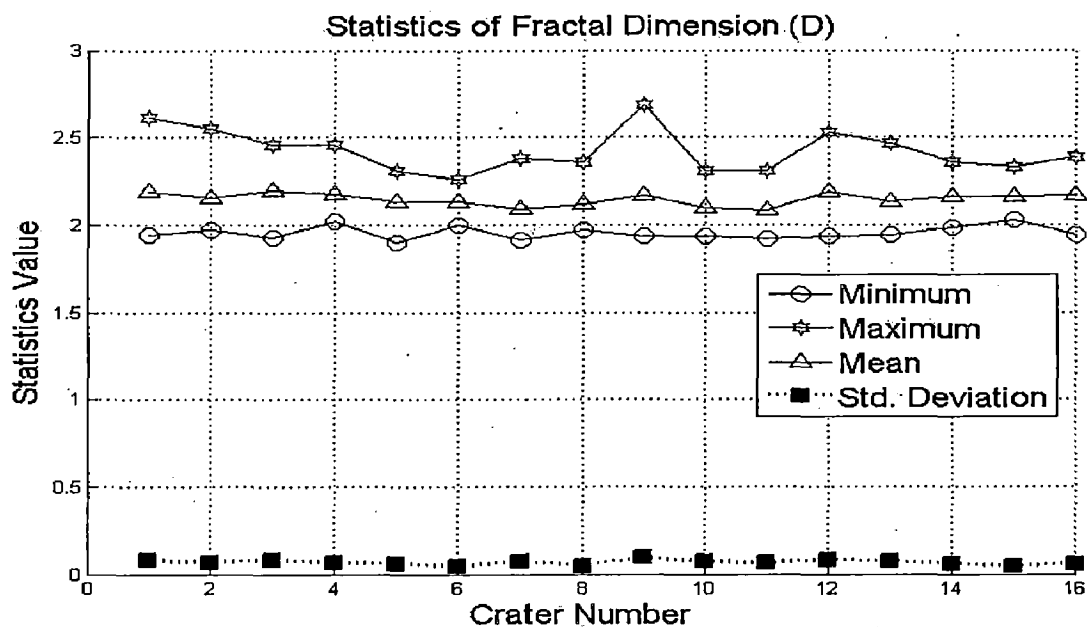
Figure: 4.24 Statistics graph of fractal dimension for 16 craters

67
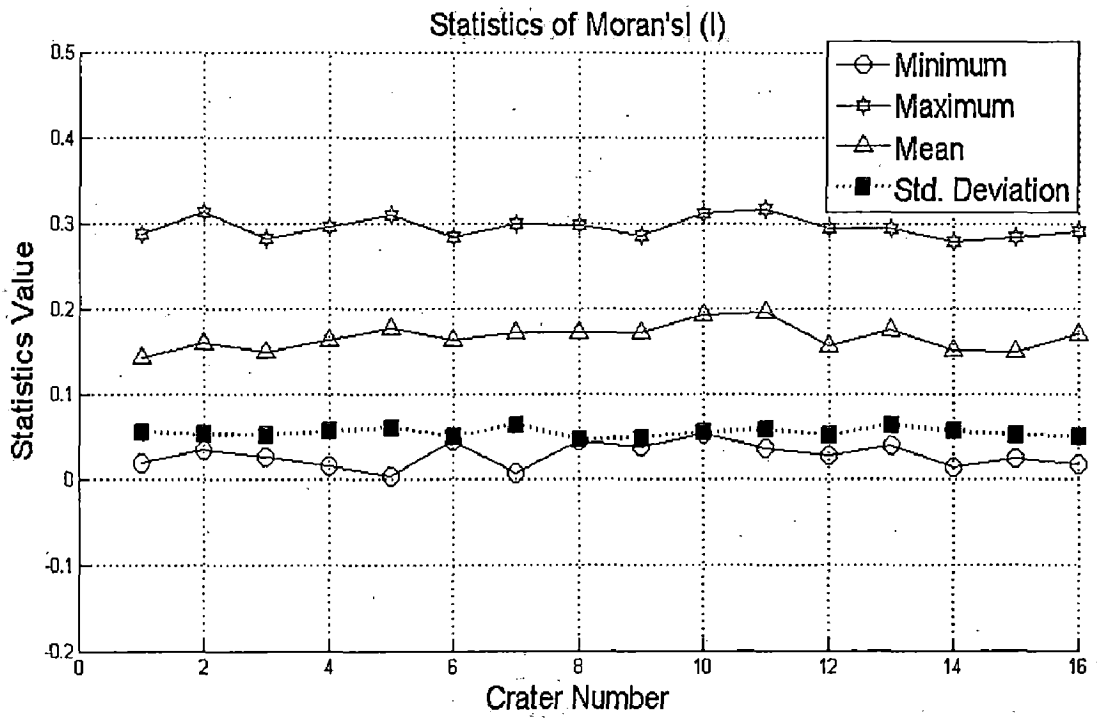
Figure 4.25 Statistics graph of Moran's _I_ for 16 craters
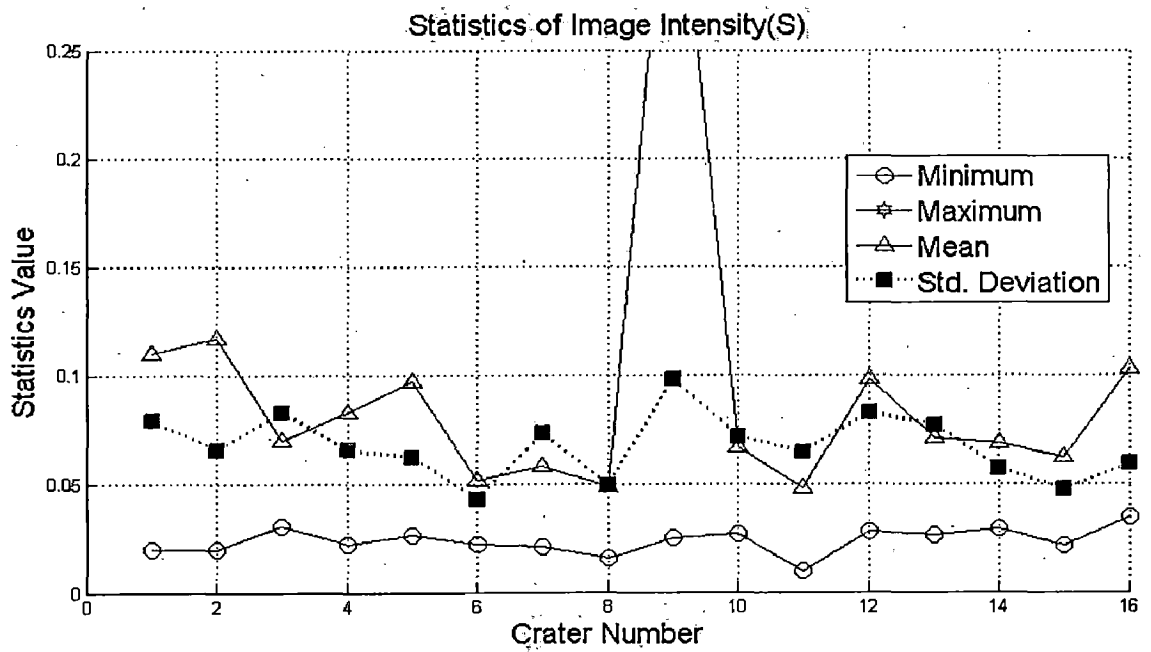
Figure 4.26 Statistics graph of total intensity 'S' for 16 craters

4.6 Comparison of two different images for some craters.

4.6.1. Comparison of RGB image and classified D+I+S for a random crater:

In Fig.4.27 comparison between RGB image of 'm-δ' decomposed image and classified image of D+I+S map is done for a crater region. In Fig.4.27a RGB image of m-δ decomposition and in Fig.4.27b classified image is shown. From RGB image of m-δ decomposition it is clear that base of rim has surface and volume scatterers and outside where the pixels are shown in magenta are regions having double bounce and surface scatterers. So comparing these two images we can estimate that in classified image green pixels contain primarily volume and surface scatterers, blue pixels contain double bounce and surface scattering properties these conclusions are not very conclusive, it's only a rough idea of scattering behaviour or these two classes. For good results classification of smaller region should be done.
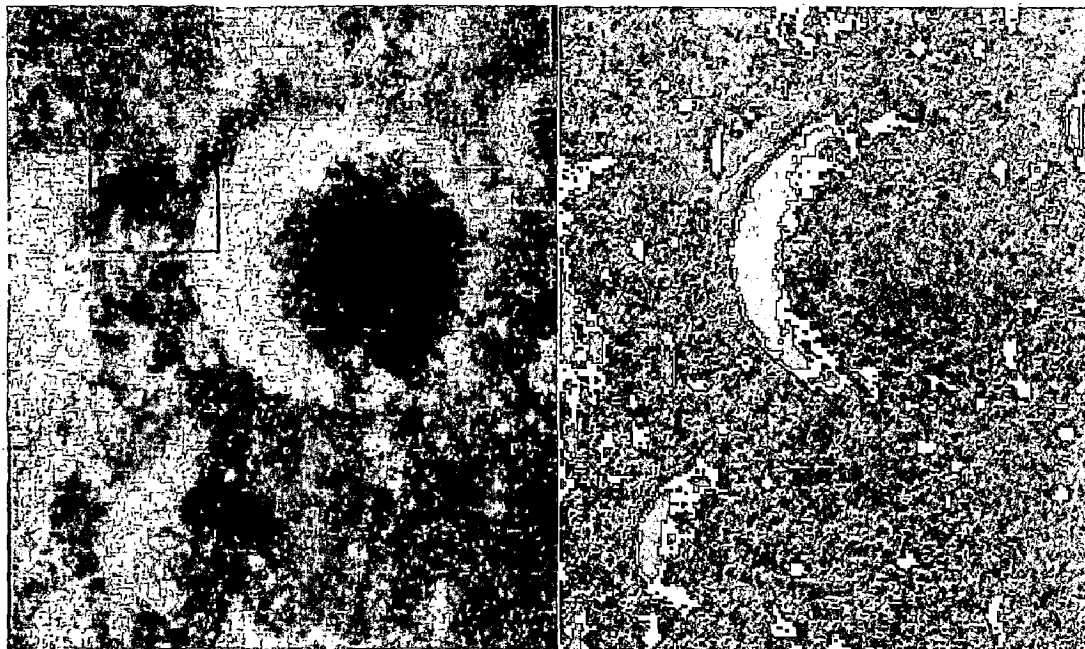
(a) m-δ decomposed image   (b) Classified image

Figure: 4.27 (a) Comparison of m-δ decomposed image and Classified result

4.6.2. Comparison of RGB images of two craters

In Fig.4.28 comparison between RGB image of 'm-δ' decomposed image for crater type-I and crater type-II is done for a crater. In Fig.4.28a RGB image of type-I and in Fig.4.28bRGB image of type-II crater is shown. In these images we can see that type-I craters has larger number of green pixels and also green pixels have more intensity when compared to type-II craters. We can also see that base of type-II craters has larger number of magenta pixels thus it has regions having double bounce and surface scatterers thus we can conclude for type-II craters double bounce scatterers were responsible for CPR>1.
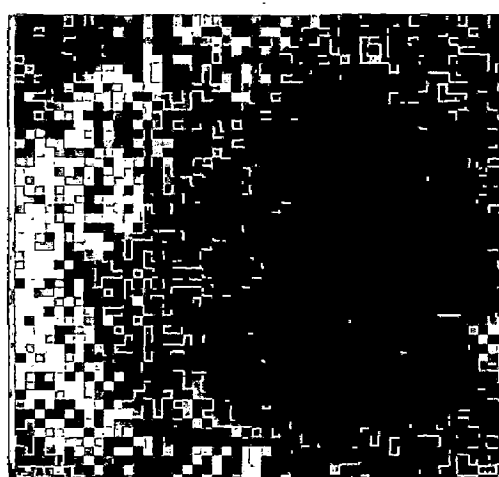
(a) Type-I crater   (b) Type-II crater

Figure: 4.28 RGB image of type-I and type-II craters to study scattering mechanism

4.6.3. Comparison of classified image of type-I and type-II craters

Figure: 4.29 Comparison of classified image of 'D+I+S' map for type-I and type-II crater

In Fig.4.29 comparison between classified image of 'D+I+S' map for crater type-I and crater type-II is shown. In Fig.4.29a classified image of type-I and in Fig.4.29b classified image of type-II crater is shown. In these images we can see that type-I craters has larger number of blue pixels which represents class-3 and type-II has large number of green pixels which represents class-2. However dominance of class-2 in type-I crater can be seen here but we cannot generalize this as this trend is observed in very few craters which is type-I craters.

Chapter 5

Conclusion

In this thesis polarimetric study and classification lunar surface using textural property of mini-SAR data is carried out. It is a unique attempt to apply satellite image classification techniques to lunar surface. Fractals and spatial autocorrelations are considered for texture analysis. Textural information based on fractal properties and spatial autocorrelation is extracted using different methods. Then K-means classification algorithm is applied to such textured images to cluster lunar surface in different classes. The limitation of classification algorithms is that they necessitate prior information about study area. The success of this classification lies in the fact that how accurately the land cover classification is being performed for lunar surface using mini-SAR and its textured images. However the accuracy of this study cannot be calculate but it still can provide a very good platform for future classification strategies.

The present work is dedicated to terrain classification of lunar surface using **mini-SAR (Miniature Synthetic Aperture Radar)** data. Craters based on its 'm-δ' and CPR property has been classified in two categories, one having dominant volume scattering phenomenon and another having dominant double bounce and surface scattering phenomenon, in present thesis these two types of craters are called type-I and type-II respectively. A density function based approach is applied to differentiate type-I and type-II craters. Classification of mini-SAR images for different regions are done to identify different classes present in it and their relation to some specific ground cover type which could be identified easily (mostly of crater regions).

Summary of chapters

Chapter 1, Presents an overview of the Chandrayan-I mission of ISRO. A brief description of problem formulation is given. About aim and objectives of this dissertation is discussed. It also gives a brief description of different scattering phenomenon.

Chapter 2, Gives a brief review of radar basics and different scattering models. It gives an overview of the properties of mini-SAR sensor. Definition and application of fractals and spatial autocorrelation (Moran's I) in satellite image analysis are discussed. Classification algorithms (K-means) used in this thesis is also presented. Description of different scattering phenomenon is given.

Chapter 3, Describes the methodology used for classifying type-I and type-II craters using m-δ technique, 'm-δ' decomposition to generate RGB image of mini-SAR data to understand scattering phenomenon associated with lunar surface. Then using this results as training data a pattern analysis technique to identify type-I and type-II craters is presented. Methodology for statistical analysis of CPR pixels to determine best fit distribution function is presented.

Chapter 4, It presents the results obtained from 'm-δ' analysis of craters. Range of estimated position and shape parameter for the two types of craters is determined. Classified images are analyzed to identify various surface type viz. rim or craters, base of craters edge of crater. Statistics of pixels from different classes are calculated. Dependence of fractal dimension and Morans'I value on window size is discussed.

Concluding remarks and Future Work

Probability density based technique is presented for identifying two types of craters based on mean and standard deviation of position and shape parameters.

In this study classification algorithms were applied only for five classes and a large region of interest (ROI) was selected for analysis. So, detail study of particular regions (e.g. different craters) to explore the properties of lunar surface is required. Selecting ROIs limited to craters and its neighbouring for large numbers of craters can be done based on textural analysis discussed in this work.

Textural analysis is performed on total power image this could be performed digital elevation map (DEM) of lunar surface to estimate roughness and to analyze different scattering mechanisms.

A detail study of classified images for more number of classes is also required. Analysis of accuracy of performed classification should be done by collecting available ground truth data on lunar surface from different agencies based on accuracy results window size could be optimized.

73

APPENDIX-I

Mode	SAR	Scatterometer
System parameters		
Altitude	100km	100km
Frequency	2.38 GHz(S-band)	2.38 GHz(S-band)
Polarization	Transmit LCP; Receive H & V	Transmit LCP; Receive H & V
Spacecraft Velocity	1631 m/s	1631 m/s
Range swath	8km	NA
Strip length	325km	300km
Antenna parameters		
Antenna length	1.37m	1.37m
Antenna width	0.925m	0.925m
Boresight gain	26.1dB	26.1dB
Antenna efficiency	53%	53%
Grazing angle	55 deg	90 deg
Image quality parameters		
Noise equivalent sigma naught	-30dB	-15dB
Slant range resolution	86m	N/A
Ground range resolution	75m	N/A
Azimuth resolution	150m	1000m
Multiplicative noise ratio	-12dB	-12dB
RF parameters		
Transmit pulse width	84μs	83μs
Chirp bandwidth	2.1 MHz	2.1 MHz

74

Peak power at transmitter port	40 W	40 W
Average transmitted power	11 W	11 W
System noise temperature	620K	620K
Digital parameters		
PRF	3100 Hz	3750 Hz
No. samples/pulse	1119	1186
A/D sampling frequency	8.2 MHz	8.2 MHz
Number of bits per sample	8	8
Number of receive channels	2	2
Peak data rate into SSDR	183.43 Mbps	187.43 Mbps
Collect time/orbit	6 min	6 min

APPENDIX-II

CRITICAL χ2 VALUES FOR UP TO 30 DEGREES OF FREEDOM

Degree of Freedom	α= 0.1	α= 0.05	α= 0.01
1	2.706	3.841	6.635
2	4.605	5.991	9.21
3	6.251	7.815	11.345
4	7.779	9.488	13.277
5	9.236	11.07	15.086
6	10.645	12.592	16.812
7	12.017	14.067	18.475
8	13.362	15.507	20.09
9	14.684	16.919	21.666
10	15.987	18.307	23.209
11	17.275	19.675	24.725
12	18.549	21.026	26.217
13	19.812	22.362	27.688
14	21.064	23.685	29.141
15	22.307	24.996	30.578
16	23.542	26.296	32
17	24.769	27.587	33.409
18	25.989	28.869	34.805
19	27.204	30.144	36.191
20	28.412	31.41	37.566
21	29.615	32.671	38.932
22	30.813	33.924	40.289
23	32.007	35.172	41.638
24	33.196	36.415	42.98
25	34.382	37.652	44.314
26	35.563	38.885	45.642
27	36.741	40.113	46.963
28	37.916	41.337	43.278
29	39.087	42.557	49.558
30	40.256	43.773	50.892

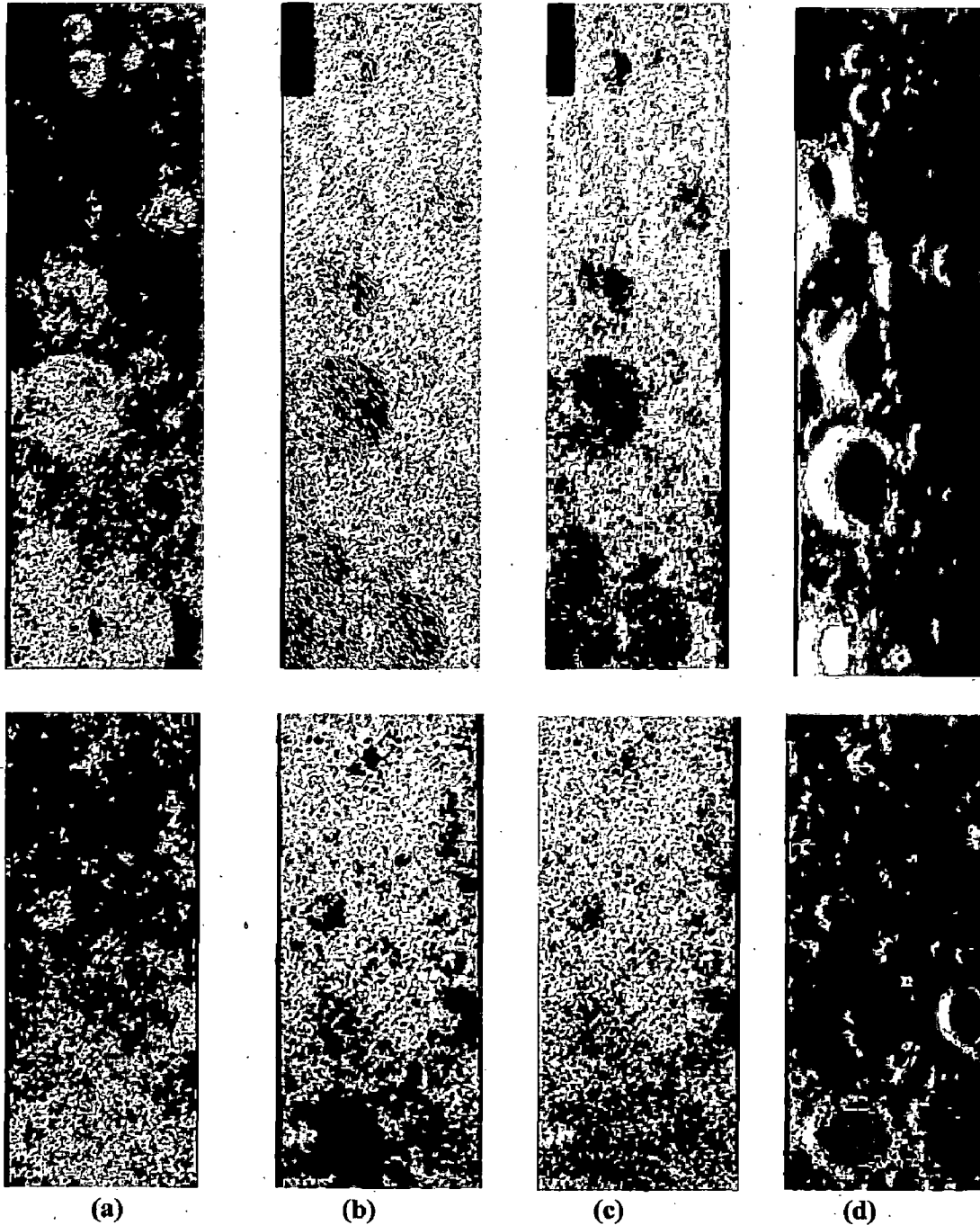# APPENDIX-III

(a) (b) (c) (d)

Figure 5.1 Pixels having a) CPR>1 are masked by red colour, b) m<0.35 pixels are blue colour, c)CPR>1
& m<0.35 are masked by green colour. d) ROIs from different crater regions are shown.

(LEFT BLANK DELIBERATELY)

REFERENCES

[1]'ISRO' "Chandrayaan-1, India's First Mission to Moon"[online]. Available at: http://www.isro.org/chandrayaan/htmls/home.htm

[2] Spudis, P., S. Nozette, B. Bussey, K. Raney, H. Winters, C. L. Lichtenberg,W. M. Marinelli, J. C. Crusan, and M. M. Gates (2009), "MiniSAR: An imaging radar experiment for the Chandrayaan1 mission to the Moon," *Current Science*, Vol. *96*, 533–539

[3]Mohan S., Das A. and Chakraborty M(2011), "Study of polarimetric properties of lunar surface using Mini-SAR data", *current Science,* Vol.101, No.2, 2011

[4]Raney, R.K.; Spudis, P.D.; Bussey, B.; Crusan, J.; Jensen, J.R.; Marinelli, W.; McKerracher, P.; Neish, C.; Palsetia, M.; Schulze, R.; Sequeira, H.B.; Winters, H.; , "The Lunar Mini-RF Radars: Hybrid Polarimetric Architecture and Initial Results," *Proceedings of the IEEE* , vol.99, no.5,pp.808-823, May 2011

[5]'NASA' "Ask an astronomer for Kids"[online] Available at: http://coolcosmos.ipac.caltech.edu/ cosmic_kids/AskKids/Moontemp.shtml

[6]'NASA' "Ice on Moon" [Online] Available at: http://nssdc.gsfc.nasa.gov/planetary/ice/ice_Moon.html

[7]'Internet' "Water Ice Found On Moon"[online]. Available at: http://www.space.com/7987-tons-water-ice-Moon-north-pole.html

[8]'NASA', Press Release, "NASA Radar Finds Ice Deposits at Moon's North Pole; Additional Evidence of Water Activity on Moon." [online] Available at: http://www.nasa.gov/home/hqnews/2010/mar/HQ_10-055_Moon_ice.html

[9]Baghdadi, N., King, C., Bourguignon, A. and Remond, A., 2002, "Potential of ERS and RADARSAT data for surface roughness monitoring over bare agricultural fields: application to catchments in northern France." *International Journal of Remote Sensing*, vol. 23, pp. 3427–3442.

[10] W. M. Boerner et al., "Determination of the characteristic polarisation states of the radar target scattering matrix [(AB)] for the coherent, monostatic and reciprocal propagation

space using the polarisation ratio," in *Direct and Inverse Methods in Radar Polarimetry, Kluwer Academic Publishers*, Netherlands, Kluwer Academic Publishers, pp. 297-349,1992 .

[11] W. M. Boerner, W-Ling Yan, An-Qing XI, and Y. Y, "On the basic principles polarimetry: the target of radar characteristic polarization state theory of Kennaugh, Huynen's polarization fork concept, and its extension to the partially polarized case," *IEEE Proceedings*, vol. 79, no. 10, pp. 1538-1550,1991

[12] W. M. Boerner, E. Pottier, S. Cloude, "Extra-wide-band Polarimetry, Interferometry & Polarimetric Interferometry in Synthetic Aperture Remote Sensing", International Symposium on Antennas and Propagation, , ACROS Fukoka, Japan, 2000.

[13] A. Freeman and S. L. Durden, "A three-component scattering model for polarimetric SAR data," *IEEE Trans. Geosci. Remote Sens.*, vol. 36, no. 3, pp. 963–973, 1998.

[14]C . Oliver and S. Quegan, Understanding Synthetic Aperture Radar Image s, 2nd ed. R aleigh, NC: SciTech Publ., 2004

[15] Doulgeris, A.; Anfinsen, S.N.; Eltoft, T.; , "Analysis of non-Gaussian POLSAR data," *Geoscience and Remote Sensing Symposium, 2007. IGARSS 2007. IEEE International* , vol., no., pp.160-163, 23-28 July 2007

[16]Anfinsen, S.N.; Doulgeris, A.P.; Eltoft, T.; , "Goodness-of-Fit Tests for Multilook Polarimetric Radar Data Based on the Mellin Transform," *Geoscience and Remote Sensing, IEEE Transactions on* , vol.49, no.7, pp.2764-2781, July 2011

[17] Lemeshko, B.Yu.; Postovalov, S.N.; Chimitova, E.V.; , "Rules of application of goodness-of-fit tests in simple and composite hypothesis testing," *Science and Technology, 2003. Proceedings KORUS 2003. The 7th Korea-Russia International Symposium on* , vol.1, no., pp.369-375 vol.1, 6-6 July 2003

[18] Mascialino, B.; Pfeiffer, A.; Pia, M.G.; Ribon, A.; Viarengo, P.; , "Evaluation of the power of Goodness-of-Fit tests for the comparison of data distributions," *Nuclear Science Symposium Conference Record, 2006. IEEE* , vol.1, no., pp.101-103, Oct. 29 2006-Nov. 1 2006

[19] Cirrone, G.A.P.; Donadio, S.; Guatelli, S.; Mantero, A.; Mascialino, B.; Parlati, S.; Pia, M.G.; Pfeiffer, A.; Ribon, A.; Viarengo, P.; , "A goodness-of-fit statistical toolkit," *Nuclear Science, IEEE Transactions on* , vol.51, no.5, pp. 2056- 2063, Oct. 2004

[20] 'National Institute of Standards and Technology, Information technology laboratory' Kolmogorov-Smirnov Goodness-of-Fit Test[online] Available at: www.itl.nist.gov/div898/handbook/eda/section3/eda35g.htm

[21] 'National Institute of Standards and Technology, Information technology laboratory' Chi-Square Goodness of Fit test [online]. Available at: www.itl.nist.gov/div898/handbook/eda/section3/eda35f.htm

[22] 'National Institute of Standards and Technology, Information technology laboratory' Anderson-Darling Goodness of Fit test [online]. Available at: www.itl.nist.gov/div898/handbook/eda/section3/eda35e.htm

[23] Lillesand, M.T., and Kiefer, R.W., *Remote Sensing and Image Interpretation*, Fourth Edition. John Wiley & Sons, New York, 2000.

[24] J.A. Richards, *Remote Sensing Digital Image Analysis*, Springer-Verlag, Berlin, 1999.

[25] Brandt Tso, Paul Mather, *Classification Methods for Remotely Sensed Data*, 2nd ed. CRC Press, Taylor & Francis Group, LLC, 2009

[26] Moth'd Belal, and Al-Daoud, "A New Algorithm for Cluster Initialization," *J. World Academy of Science, Engineering and Technology*, 2005.
Pr-24 same

[27] .M.Pena, J.A. Lozano, P. Larranaga, "An empirical comparison of four initialization methods for the K-Means algorithm," *Pattern Recognition Letters*, vol. 20, pp.1027-1040, 1999.

[28] N. . Venkateswarlu, and P. Raju, "Fast isodata clustering algorithms," *Pattern recognition*, vol. 25 (3), pp. 335-342, 1992

[29]Mandelbrot, B.B. 1982, *The Fractal Geometry of Nature*. W.H. Freeman and Co., New York.

[30] De Jong, S.M. and Burrough, P.A., 1995, A fractal approach to the classification of Mediterranean vegetation types in remotely sensed images. *Photogrammetric Engineering and Remote Sensing*, vol. 61, no. 8, pp. 1041–1053.

[31] Falconer, K., 2003, *Fractal Geometry: Mathematical Foundations and Applications*. John Wiley and Sons, Ltd., England.

[32] Keller, J.M., Crownover, R.M. and Chen, S., 1987, Characteristics of natural scenes related to the fractal dimension. *IEEE Transactions on Pattern Analysis and Machine Intelligence*, vol. PAMI-9, no. 5, pp. 621–627.

[33] Pant, T., Singh, D. and Srivastava, T., 2010, Advanced fractal approach for unsupervised classification of SAR images. *Advances in Space Research*, vol. 45, no. 11, pp. 1338–1349.

[34] Pant, T., Singh, D. and Srivastava, T., 2010, The potential application of fractal approach for surface roughness retrieval: a study for simulated surfaces. *Geomatics, Natural Hazards and Risk*, vol. 1, no. 3, pp. 243–257.

[35] Sun, W., Xu, G., Gong, P. and Liang, S., 2006, Fractal analysis of remotely sensed images: A review of methods and applications. *International Journal of Remote Sensing*, vol. 27, no. 21-22, pp. 4963–4990.

[36] Emerson, C.W., Lam, N.S.N. and Quattrochi, D.A., 2005, A comparison of local variance, fractal dimension, and Moran's I as aids to multispectral image classification. *International Journal of Remote Sensing*, vol. 26, no. 8, pp. 1575–1588.

[37] Pentland, A.P., 1984, Fractal-based description of natural scenes. *IEEE Transactions on Pattern Analysis and Machine Intelligence*, vol. PAMI-6, no. 6, pp. 661–674.

[38] Zribi, M., Ciarletti, V. and Taconet, O., 2000, Validation of a rough surface model based on fractional brownian geometry with SIRC and ERASME radar data over Orgeval. *Remote Sensing of Environment*, vol. 73, pp. 65–72.

[39] Falconer, K., 2003, *Fractal Geometry: "Mathematical Foundations and Applications."* John Wiley and Sons, Ltd., England.

·[40] De Jong, S.M. and Burrough, P.A., 1995, "A fractal approach to the classification of Mediterranean vegetation types in remotely sensed images." *Photogrammetric Engineering and Remote Sensing,* vol. 61, no. 8, pp. 1041–1053.

[41] Self similarity image. Available online at http://mumble.net/~jar/visuals/fractal.png

[42] De Cola, L., 1989, Fractal analysis of a classified Landsat scene. *Photogrammetric ·Engineering and Remote Sensing,* vol. 55, no. 5, pp. 601–610.

[43] Sarkar, N. and Chaudhuri, B.B., An efficient differential box-counting approach to compute fractal dimension of image. *IEEE Transactions on Systems, Man, and Cybernatics,* vol. 24, no. 1, pp. 115–120, 1994.

[44] Clarke, K.C., "Computation of the fractal dimension of topographic surfaces using the triangular prism surface area method." *Computers and Geosciences,* vol. 12, no. 5, pp. 713–722, 1986

[45] Sun, W., "Three new implementations of the triangular prism method for computing the fractal dimension of remote sensing images." *Photogrammetric Engineering and Remote Sensing,* vol. 72, no. 4, pp. 373–382, 2006.

[46] Jaggi, S., Quattrochi, D.A. and Lam, N.S.N., "Implementation and operation of three fractal measurement algorithms for analysis of remote sensing data". *Computer and Geosciences,* vol. 19, pp. 745–767, 1993.

[47] Berizzi, F., Bertini, G., Martorella, M. and Bertacca, M., 2006, "Two-dimensional variation algorithm for fractal analysis of sea SAR images". *IEEE Transactions on Geoscience and Remote Sensing,* vol. 44, no. 9, pp. 2361–2373.

[48] L loyd, C.D., 2007, *Local Models for Spatial Analysis.* CRC Press, London.

[49] Read, and Lam, N.S.N., 2002, Spatial methods for characterising land cover detection land-cover changes for the tropics. *International Journal of Remote Sensing,* vol. 23, no. 12, pp. 2457–2474.

[50] Liu Tao; , "Comments on "Statistics of the Degree of Polarization," *Antennas and Propagation, IEEE Transactionson,* vol.56, no.9, pp.3085-3086, Sept.2008

[51] Hirosawa, H.; , "Degree of polarization of radar backscatters from a mixed target ," *Geoscience and Remote Sensing, IEEE Transactions on* , vol.35, no.2, pp.466-470, Mar 1997

[52] Gaikwad, A.N, "Study of Through Wall Imaging for Target Detection" 'Ph.D Thesis', Department of Electronics and Communication, IIT Roorkee, 2011.

[53]Gunaratna N. et.al, "Spatial Autocorrelation", Available online at: www.stat.purdue.edu/~bacraig/SCS/Spatial%2520Correlation%2520new.doc

[54] "Image of primary colour wheel", Available online at: http://bluelobsterart.com/wordpress/wp-content/uploads/2009/03/rgb-color-wheel-lg.jpg

[55] "Description on Generalised Extreme Value Function" [online]. Available at: http://www.mathwave.com/help/easyfit/html/analyses/distributions/gen_extreme.html

[56] Myint, S.W., , "Fractal approaches in texture analysis and classification of remotely sensed data: comparisons with spatial autocorrelation techniques and simple descriptive statistics." *International Journal of Remote Sensing*, vol. 24, no. 9, pp. 1925–1947, 2003.

LIST OF PUBLICATION

The following publication was communicated at the time of submission of this dissertation:

Shailesh Kumar, Dharmendra Singh, Pooja Mishra, "Fractal and Moran's I analysis for classification of Lunar surface using Mini-SAR data of Chandrayan-I" IEEE Microwave 2012 conference, July,August, India.